ANALYSIS OF STABILITY AND TRANSITION IN FLAT PLATE COMPRESSIBLE BOUNDARY LAYERS USING LINEAR STABILITY THEORY

A THESIS SUBMITTED TO
THE GRADUATE SCHOOL OF NATURAL AND APPLIED SCIENCES
OF
MIDDLE EAST TECHNICAL UNIVERSITY

BY

H. SENEM ATALAYER

IN PARTIAL FULFILLMENT OF THE REQUIREMENTS
FOR
THE DEGREE OF MASTER OF SCIENCE
IN
AEROSPACE ENGINEERING

SEPTEMBER 2004

Approval of the Graduate School of Natural and Applied Sciences.

Prof. Dr. Canan Özgen
Director

I certify that this thesis satisfies all the requirements as a thesis for the degree of Master of Science.

Prof. Dr. Nafiz Alemdaroğlu
Head of Department

This is to certify that we have read this thesis and that in our opinion it is fully adequate, in scope and quality, as a thesis for the degree of Master of Science.

Assoc. Prof. Dr. Serkan Özgen
Supervisor

Examining Committee Members

Prof. Dr. Nafiz Alemdaroğlu	(METU, AEE)	
Assoc. Prof. Dr. Serkan Özgen	(METU, AEE)	
Prof. Dr. Zafer Dursunkaya	(METU, ME)	
Assoc. Prof. Dr. Yusuf Özyörük	(METU, AEE)	
Assoc. Prof. Dr. Sinan Eyi	(METU, AEE)	

I hereby declare that all information in this document has been obtained and presented in accordance with academic rules and ethical conduct. I also declare that, as required by these rules and conduct, I have fully cited and referenced all material and results that are not original to this work.

Name, Last name : H. Senem Atalayer

Signature :

ABSTRACT

ANALYSIS OF STABILITY AND TRANSITION IN FLAT PLATE COMPRESSIBLE BOUNDARY LAYERS USING LINEAR STABILITY THEORY

Atalayer, Hayriye Senem

M. S., Department of Aerospace Engineering

Supervisor: Assoc. Prof. Dr. Serkan Özgen

September 2004, 198 Pages

In this study, numerical investigations of stability and transition problems were performed for 2D compressible boundary layers over a flat plate in adiabatic wall condition. Emphasis was placed on linear stability theory. The mathematical formulation for 3D boundary layers with oblique waves including detailed theoretical information was followed by use of the numerical techniques for the solution of resulting differential system of the instability problem, consequently an eigenvalue problem.

First, two-dimensional sinusoidal disturbances were analyzed at various Mach numbers including the subsonic, transonic, supersonic and

even hypersonic flow speeds. In this case, the second mode (acoustic mode), namely the *Mack mode*, and its behavior with the increasing Mach number were visualized. The results were then compared with the available data in literature concluding with good agreements.

Secondly, similar analysis was carried out for oblique waves. Here, not only the effect of flow speed but also the effect of wave orientation was demonstrated. For this purpose, instability problem was solved for several wave angles at each Mach number in the range of M=0 and M=5. In this respect, the angle at which the waves were most unstable was also obtained at each investigated flow speed. The resultant stability diagrams corresponding to M=4 and higher Mach numbers for which both first and the second modes appear revealed that plane waves were more stable than oblique waves for the Tollmien-Schlichting mode, however, this was the opposite for the acoustic mode where oblique waves were observed to be more stable.

As a final step, estimation of the transition location was handled for the most unstable wave condition. Smith-Van Ingen e^n transition method was applied as the prediction device. The results representing the influence of Mach number on transition Reynolds number were then compared with the experimental data as well as the numerical ones in literature ending up with very good agreements.

Keywords: Compressible Boundary Layer, Linear Stability Theory, Oblique Wave, Laminar-Turbulent Transition.

ÖZ

DÜZ LEVHALAR ÜZERİNDEKİ SIKIŞTIRILABİLİR SINIR TABAKALARDA DOĞRUSAL KARARLILIK TEORİSİ İLE KARARLILIK VE GEÇİŞ ANALİZİ

Atalayer, Hayriye Senem
Yüksek Lisans, Havacılık ve Uzay Mühendisliği Bölümü
Tez yöneticisi: Doç. Dr. Serkan Özgen

Eylül 2004, 198 Sayfa

Bu çalışmada, adyabatik duvar koşulundaki düz levha üzerinde iki boyutlu sıkıştırılabilir sınır tabakaların kararlılık ve geçiş problemlerinin sayısal araştırması gerçekleştirilmiştir. Çalışmadaki analiz doğrusal kararlılık teorisi üzerine kurulmuştur. Düzlemsel olmayan dalgalara sahip üç boyutlu sınır tabakalar için geliştirilen ve detaylı teorik bilgi de içeren matematiksel formülleme, sonuçta bir özdeğer problemine dönüşen ve kararsızlık problemini tasvir eden diferansiyel denklem sisteminin çözümü için sayısal tekniklerin kullanımı ile devam etmiştir.

Öncelikle, sübsonik, transonik, süpersonik ve hatta hipersonik akım

hızlarını da kapsayan çeşitli Mach değerlerindeki iki boyutlu sinüzoidal bozuntular analiz edilmiştir. Bu çalışmada, *Mack mod* olarak da bilinen ikinci mod (akustik mod) ve bu modun artan Mach sayısına tepkisi görsellenmiştir. Elde edilen sonuçlar daha sonra literatürdeki mevcut bilgilerle karşılaştırılmış ve çok iyi uyuşmalar gözlenmiştir.

İkinci olarak, benzer analiz düzlemsel olmayan dalgalar için gerçekleştirilmiştir. Burada, yalnız akım hızının değil, aynı zamanda dalga yönünün etkisi de gösterilmiştir. Bunun için kararsızlık probleminin çözümü M=0 ile M=5 aralığındaki her Mach sayısında çeşitli dalga açıları için yinelenmiştir. Böylelikle, incelenen her akım hızında en kararsız dalgayı veren açı da bulunmuştur. Sonuçta elde edilenler arasında M=4 ve sonrasına ait kararlılık çizelgeleri göstermiştir ki, TS modu için düzlemsel dalgalar düzlemsel olmayan dalgalara kıyasla çok daha kararlıdır. Akustik mod için ise tersi söz konusu olmuştur, yani düzlemsel olmayan dalgaların daha kararlı olduğu gözlemlenmiştir.

Son olarak, en kararsız dalga koşulu için geçiş konumunun tahmini ele alınmıştır. Tahmin mekanizması olarak ise e^n Smith-Van Ingen metodu uygulanmıştır. Mach sayısının geçiş Reynolds değeri üzerindeki etkisini betimleyen sonuçlar daha sonra literatürdeki sayısal çalışmalarla olduğu kadar deneysel verilerler de karşılaştırılmıştır ki, elde edilen uyum oldukça iyidir.

Anahtar Kelimeler: Sıkıştırılabilir Sınır Tabaka, Doğrusal Kararlılık Teorisi, Düzlemsel Olmayan Sinüzoidal Dalga, Laminer-Türbülans Geçişi.

ACKNOWLEDGMENTS

I would like to express my deepest appreciation to Assoc. Prof. Dr. Serkan Özgen, for his great supervision comprising his advices, encouragement and support throughout this study.

I would like to thank to all academic staff; my instructors providing me a great education both in my undergraduate and graduate studies; the research assistants and my colleagues for their understandings and motivations, the administrative staff especially Nilgün Kaplan and Figen Kılıç for their sincere smiles. I also want to thank to the technical staff for their invisible assistances.

My grateful thanks are for my mother, my friend Nuray Atalayer who is always with me and cares about me more than herself; for my father Faruk Atalayer, the most dialectic and original character ever I know, for his priceless advices making me withstand in my most pessimistic times and for my brother Çağlar, my successful 'havacı' in the future, for his loving and continual support throughout my life. My special thanks go to my all friends giving me their love and support throughout this study.

I wish to express my endless thanks to my love Faruk for his invaluable love as well as his encouraging and support at every moment. Thank you for being always with me…

TABLE OF CONTENTS

LIST OF TABLES

TABLES

LIST OF FIGURES

FIGURES

NOMENCLATURE

A	disturbance amplitude
A_0	initial disturbance amplitude at $R = R_0$
A_r	fixed reference amplitude
$\vec{A}$	$= (-\alpha_i, -\beta_i)$: spatial amplification vector
$\lvert\vec{A}\rvert$	magnitude of $\vec{A}$
a^*	local speed of sound (m/sec)
c	$= c_r + ic_i$: complex wave velocity
c_i	temporal amplification factor
c_r	phase speed
c_g^*	magnitude of $\vec{c}_g^*$
$\vec{c}_g^*$	group velocity (m/sec)
c_p^*	specific heat at constant pressure (J/kgK)
c_v^*	specific heat at constant volume (J/kgK)
D	$= d/dy$
D	determinant, DET
$\vec{e}_i$	unit vector
$\bar{e}_{ij}^*$	rate of strain tensor
f	$= \omega_r / R$: dimensionless circular frequency
f_{FS}	dimensionless stream function
g	$= T^* / T_e^*$
h^*	enthalpy per unit mass (J/kg)
J	Jacobian matrix
k	magnitude of $\vec{k}$
$\vec{k}$	wave number vector
L^*	$= \left(\nu^* x^* / U_e^*\right)^{1/2}$: Blasius length scale
m	dimensionless pressure gradient
M	freestream Mach number
M_r	reference Mach number
$\breve{M}$	relative Mach number
n	maximum amplification rate
P	$= 1$: mean-state pressure normalized by P_e^*
P_r	Prandtl number

$\hat{p}$ disturbance-state pressure normalized by P_e^*

$\overline{p}$ disturbance pressure amplitude function

P^* mean-state pressure

P_e^* freestream pressure (Pa)

$\hat{p}^*$ disturbance-state pressure

$\overline{p}^*$ instantaneous pressure (Pa)

R $= R_{FS}$: Reynolds number based on Blasius length scale

R_{tr} transition Reynolds number

R_x $= U_e^* x^* / \nu_e^*$: Reynolds number based on streamwise distance

R_0 Reynolds number where the wave enters the unstable region

R_1 Reynolds number where the wave leaves the unstable region

R^* Universal gas constant (J/kgK)

S_1 Sutherland constant normalized by T_e^*

S_1^* Sutherland constant (K)

t time normalized by L^* / U_e^*

T mean-state temperature normalized by T_e^*

$\hat{T}$ disturbance-state temperature normalized by T_e^*

$\overline{T}$ disturbance temperature amplitude function

t^* time (sec)

T^* mean-state temperature

T_e^* freestream temperature (K)

T_w^* adiabatic wall temperature (K)

$\hat{T}^*$ disturbance-state temperature

$\overline{T}^*$ instantaneous temperature (K)

U streamwise mean velocity component normalized by U_e^*

$\hat{u}, \hat{v}, \hat{w}$ disturbance velocity field normalized by U_e^*

$\overline{u}, \overline{v}, \overline{w}$ disturbance velocity amplitude functions

U^* streamwise mean velocity component

U_e^* local freestream streamwise velocity component (m/sec)

$\hat{u}^*, \hat{v}^*, \hat{w}^*$ dimensional disturbance velocity field

$\overline{u}^*, \overline{v}^*, \overline{w}^*$ instantaneous velocity components (m/sec)

V normal mean velocity component normalized by U_e^*

$V_{s,i}$ uniform mean flow solution vectors

v_i elements of the $V_{s,i}$ vectors

V^* normal mean velocity component

W spanwise mean velocity component normalized by U_e^*

$W_{orth,i}$ orthogonalized uniform mean flow solution vectors

w_i elements of the $W_{orth,i}$ vectors

W^* spanwise mean velocity component

x, y, z streamwise, normal-to-the-wall and spanwise coordinates normalized by L^*

$\vec{x}_0$ starting point for the Simplex method

$\vec{x}_1$ coordinates of the vertices of a simplex

x^*, y^*, z^* space coordinates (m)

x_g^* space coordinate in the direction of $\vec{c}_g^*$

y_e Dimensionless coordinate of start-of-integration.

y_k Dimensionless coordinate of the inflection point

Z_i variables of the first order governing differential equation system

GREEK SYMBOLS

α $= (\alpha_r + i\alpha_i)$: streamwise component of wave number vector, $\vec{k}$

α_i imaginary part of complex α

α_r real part of the complex α

β $= (\beta_r + i\beta_i)$: spanwise component of wave number vector, $\vec{k}$

β_{FS} Falkner-Skan parameter

β_i imaginary part of complex β

β_r real part of complex β

δ_1 boundary layer displacement thickness normalized by L^*

δ^* boundary layer displacement thickness

ε convergence criterion in Newton-Raphson technique

γ ratio of specific heats

φ_{ij} elements of $\vec{\varphi}_i$

$\vec{\varphi}_i$ characteristic vectors of uniform mean flow solution

$\overline{\varphi}$ any disturbance amplitude function

$\hat{\varphi}$ any fluctuating quantity

κ mean-state thermal conductivity normalized by $c_p^* \mu_e^*$

κ^* mean-state thermal conductivity

$\hat{\kappa}^*$ disturbance-state thermal conductivity

$\overline{\kappa}^*$ instantaneous thermal conductivity (W/mK)

λ characteristic length scale in Simplex method

λ_i characteristic values of uniform mean flow solution

μ disturbance-state viscosity normalized by μ_e^*

μ^* mean-state dynamic viscosity

μ_e^* freestream dynamic viscosity ($Nsec/m^2$)

$\hat{\mu}^*$ disturbance-state viscosity

$\overline{\mu}^*$ instantaneous dynamic viscosity coefficient ($Nsec/m^2$)

ν^* mean-state kinematic viscosity

ρ mean-state density normalized by ρ_e^*

$\hat{\rho}$ disturbance-state density normalized by ρ_e^*

$\overline{\rho}$ disturbance density amplitude function

ρ^* mean-state density

ρ_e^* freestream density (kg/m^3)

$\hat{\rho}^*$ disturbance-state density

$\overline{\rho}^*$ instantaneous density (kg/m^3)

$\overline{\tau}_{ij}^*$ shear stress component (N/m^2)

ω $= k.c$: dimensionless complex frequency

ω_i $= k.c_i$: temporal growth rate of the disturbance amplitude

ω_r $= k.c_r$: circular frequency

ω_r^* circular frequency (Hz)

ψ angle of the wave number vector with respect to x

ψ_g angle of $\vec{c}_g^*$ with respect to x

$\overline{\psi}$ angle of the spatial amplification vector with respect to x

Ψ^* dimensional stream function

SUPERSCRIPTS

‘ ¯ ’	complex disturbance amplitude function
‘ ¯* ’	time-dependence
‘ ^ ’	fluctuating components
‘*’	dimensionality
‘ ” ’	$= d/dy$
‘j’	number of iterations

SUBSCRIPTS

cc	complex conjugate
cr	at critical conditions
e	edge, freestream
FS	based on zero pressure gradient Falkner-Skan length scale (Blasius length scale)
f_w	a wave of fixed frequency
g	along the direction of real group velocity
i	imaginary part of any complex variable
max	maximum
r	real part of any complex variable
tr	at transition condition

ABBREVIATIONS

TS	Tollmien-Schlichting mode

CHAPTER 1

INTRODUCTION

1.1 Motivation

Today, laminar-turbulent transition is still an important issue in fluid dynamics and aerodynamics with a large number of engineering applications. The reason is that an understanding of this process leads to controllability of the evolution of important aerodynamic quantities such as heat transfer rate, form drag and skin friction drag which are highly affected by the state of the boundary layer.

Laminar flow control is an active boundary-layer flow control technique employed to maintain the laminar flow state at chord Reynolds numbers beyond which is transitional or turbulent without the control. Because the laminar skin friction is much less than turbulent skin friction at the same Reynolds number, it is much desirable to have a laminar flow rather than turbulent flow for reducing the drag of aerodynamic vehicles which in turn brings the reduction in operating costs. Besides, the reductions in take-off gross weight, operating empty weight, fuel for a given mission leading to a reduced aircraft size, as well as the reduction in emissions and

noise are all the benefits of laminar flow. For all these to be activated, a good estimation of transition location is highly needed.

The same topic is of great importance for the hypersonic reentry vehicles as well. The skin friction being larger in amount for turbulent boundary layers yields much higher heat generation compared to the laminar boundary layers. Considering the reentry vehicles for which the heating rate is an essential parameter, the prediction of transition is vitally needed for their nose cone and heat shield requirements.

The necessity for a reliable transition prediction is observable on the improvements in turbine and engine performances requiring the control of airfoil surface heat transfer on blades and vanes. It is also mandatory for the low Reynolds number types to estimate the transition location because their separation-stall phenomena are highly affected by the stage of the boundary layer. Similar approach is applied for the golf balls as well. Their rough surfaces are designed to yield an early turbulence so as to avoid large wakes and provide less drag contribution compared to laminar case in spite of the increase in skin friction drag.

However, from different points of view turbulence is not so advantageous due to its higher contribution to skin friction drag. For the last three decades, the investigations have been concentrated on the reduction of skin friction drag providing a significant decrease in fuel consumption especially for new generations of supersonic transport aircraft having friction drag almost one third of all. The efforts taken through this problem meet at a

common point, a good estimation of boundary layer transition location which is one of the objectives of the current study.

Not only the aircraft or the spacecraft, but also the submarines and torpedoes suffer from the skin friction drag increased dramatically by turbulent boundary layers. To avoid their detection as well as the loss of their performances, the efforts should concentrate on the drag reduction and consequently, a well-done transition prediction.

In all these respects, one can conclude that an accurate transition prediction is extremely beneficial in many areas of fluid mechanics some of which are clarified here. In general point of view, the investigations on this topic regarding the aircraft and spacecraft performances can eventually result in improvements of air transportation safety leading to significantly high economic benefits in light of predicted increases in air traffic.

1.2 Overview of Stability Theory

Hydrodynamic stability is mainly concerned with the laminar flows and their breakdown to turbulence including the stages passed through the transition. To remind, the laminar flow is characterized by an ordered, layered and predictable motion while the turbulent state consists of a chaotic, swirly and fluctuating motion.

The theoretical investigations are all based on the assumption of small fluctuations and their interaction into laminar flows at a critical point. What

influences the stage of the flow is the behavior of the disturbances with time. If they die out in time, the main flow is known to be *stable*; whereas, if they amplify (show increase in their amplitudes), the flow is considered to be *unstable*, the stage at which the *transition* to turbulence is possible to occur. This is nothing but the preface of the stability theory based on the small disturbances. Accordingly, the prediction of the critical location, namely the *critical Reynolds number* representing the point where the disturbances first start amplifying is the main purpose of the small disturbance theory.

The laminar-turbulence transition mechanism is summarized in simpler words by Saric [1] and following by Arnal [2]. Accordingly, the transition process for a given body starts with the initiation of the disturbances to the laminar boundary layer. This stage is the first of the whole process and is called the *receptivity* [3]. It mainly describes the means by which the environmental disturbances enter the laminar boundary layer and create the initial amplitudes of unstable waves. How these disturbances are entrained into the flow and how the flow is affected by them are the questions that *receptivity* deals with.

Typical sources from which the disturbances can enter the boundary layer are free-stream vortices, acoustic waves (noise) as well as the free-stream turbulence all existing in the freestream or surface roughness and vibrations generated by the body itself. They basically define the disturbance environment. The disturbances entering the flow may be either small or large in amplitude. At that point the transition mechanism is classified as *natural transition* for small disturbances that the stability theory is concentrated on and *bypass* for larger disturbances.

Let the *natural transition* be the first to be handled. In this case, the second stage in transition process after receptivity corresponds to the *linear amplification* of the waves which is the only step that linear stability theory successfully represents. Here, one should notice that the current study is based on the linear theory hence it is just concentrated on this stage. However, after the amplitudes of the waves reach a finite value, they start to behave in a different manner from what is predicted by linear theory. The *nonlinearities* occurring in this case constitute the next step in transition process leading to wave-to-wave interactions and as a result, higher order instabilities. Further amplification of unstable waves leads to breakdown to turbulence. A fully turbulent flow eventually occurs after the coalescence of the turbulent spots that are referred to as *Emmons spots*. The related Reynolds number is then called the *transition Reynolds number*.

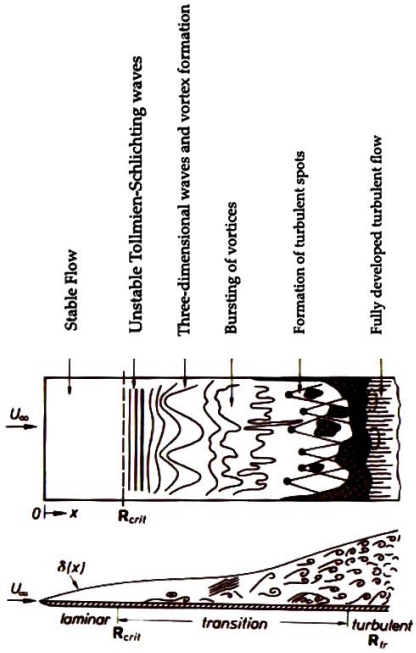

Figure 1.1 The stages of transition process in the boundary layer over a flat plate at zero angle of attack [4].

This mechanism is exactly what has been indicated by Schlichting [4] as well. Figure 1.1 gives detailed information about the stages of natural transition occurring over a flat plate demonstrated by Schlichting [4]. It also well identifies the critical Reynolds number and the transition Reynolds number.

Unlike the natural transition, if the amplitudes of the unstable waves are not so small to consider linearity, then one or more of the stages corresponding to the above mechanisms are directly *bypass*ed accompanied by immediate nonlinearities. This is hence the second possible case observed in transition.

The main reason for the instability to occur is probably due to the violation(s) in the equilibrium of the forces acting on the system. These forces can be classified as external forces including the surface tension, buoyancy in a fluid of variable density etc.; viscous forces and inertia forces. These forces have either stabilizing or destabilizing effect on the flow. However, some of them have dual influences on instability such as *viscosity*. In detail, its effect of dissipating the energy of any disturbance stabilizes the flow. This is why any bounded flow is stable when the viscosity is large enough. On the other hand, its effect of diffusing the momentum destabilizes some flow types such as parallel shear flows.

Some similar effects of viscosity are observed by the thermal conductivity as well. This parameter representing the molecular diffusion of heat tends to smooth out the temperature differences of a disturbance and

hence stabilizes the flow. In the following analysis this coefficient will be related to viscosity.

Another parameter having considerable effects on instability is the pressure gradient. A favorable one accelerates the basic flow meaning an increase in its kinetic energy. Knowing that the disturbances should absorb energy from basic flow in order to amplify, such an increase in kinetic energy prohibits the energy translation to disturbances and hence it leads the flow to stabilize. In the same manner, an adverse pressure gradient leading to a decrease in kinetic energy destabilizes the flow. The present analysis is concentrated only on zero pressure gradient case meaning that none of these effects will be observable.

The instability is affected by the velocity and temperature profiles as well. Because the viscosity is a temperature dependent parameter, any variation in temperature directly affects it, hence the instability. The velocity profile is a bit different. Its first order effect can be described by Rayleigh's inflectional theorem such that in general speaking, the existence of an inflection point at which the second derivative of the mean velocity is zero constitutes a sufficient condition for the occurrence of the instability. Accordingly, a velocity profile with that point is more unstable. The following analysis will discuss this effect for the compressible flows.

The current study covers the analysis for only the boundary layer over a flat plate, i.e., flow with a single boundary. Here, it is necessary to mention that the boundaries have also significant influences on instability. Because the amplification of the disturbances is constrained by the boundaries, the

flow is stabilized. Considering the two-wall cases such as plane Poiseuille flows, as the walls get closer, their stabilizing effect increases further. However, strong shear generated by the walls is diffused outwards by the viscosity leading to destabilization. In this respect, the flat plate boundary layers are more unstable than plane Poiseuille flows whereas, more stable than free shear flows.

For the compressible flows, one additional factor affecting the instability is the Mach number. This is however not so simple or straightforward effect just as the ones mentioned above. The current study hence concentrates on a detailed investigation of this factor in boundary layers over adiabatic flat plates.

1.3 Objectives

The analysis of stability and transition in two-dimensional compressible boundary layers over an adiabatic flat plate using the *linear stability theory* is the main purpose of the current study. In this respect, the stability analysis will be handled for initially two-dimensional disturbances at even hypersonic flow speeds. This case provides a smooth pass from the simplest incompressible case to much complex compressible three-dimensional disturbance case.

The second analysis will then go through 2D boundary layers with oblique waves. In this case, the study is limited up to high supersonic conditions. Various wave angles will be investigated in order to find the

direction at which the disturbances are most unstable, i.e., most likely to yield transition.

The last and the essential objective is then the prediction of transition location over the flat plate in the most unstable conditions. In all these analyses, comparison of the obtained results will be performed using the available data in literature to confirm the validity of the present study.

1.4 Historical Background

Since nearly a century, fluid dynamics has been concentrated on when and how laminar flows break down, their later behavior and eventual transition to turbulence all of which constitute the *hydrodynamic stability*. Helmholtz, Kelvin, Rayleigh and Reynolds were the first names having signatures in formulating these problems.

Linear stability theory as a subset of hydrodynamic stability theory, describes the linear amplification stage of the transition process for small disturbances. Its traditional analysis for the incompressible viscous plane flow comprises the solution of a linear differential equation derived by Orr (1907) and Sommerfeld (1908) independently. The linear theory is mainly concerned with individual sine waves propagating in the boundary layer parallel to the wall. These waves, referred as the instability waves, were first explained by Rayleigh (1887) and Prandtl (1921) as small, regular oscillations traveling in the laminar boundary layer. Prandtl (1921) also denoted the

destabilizing effect of the viscosity which was previously mentioned by Taylor (1915).

A complete theory of boundary layer instability was studied by Tollmien (1929) and the total amplification of the most unstable frequency waves was calculated by Schlichting (1933). That is why, the instability waves are also known as *Tollmien-Schlichting waves*. Squire (1933) stated for incompressible parallel shear flows that two-dimensional waves are first become unstable at a Reynolds number that is smaller than any value for which unstable three-dimensional waves exist. His theory is still used for incompressible analysis.

Dryden (1936) was the first who observed the velocity fluctuations in the laminar boundary layer. However, his experiments did not let the progress of the disturbances before transition be observed because the initial disturbances were quite large for a natural transition. The second attempt was performed by Nikuradse (1933) producing sinusoidal fluctuations in the boundary layer near the leading edge of a flat plate. In fact, the main purpose was the observation of transition point. So, both the artificial and the natural fluctuations were not again suitable for a natural transition.

The first successful demonstrations in this manner were done by Schubauer and Skramstad [5]. The existence of the TS waves in a Blasius boundary layer on a flat plate was then confirmed by their investigations. In those well-known experiments based on a hot-wire equipment, the oscillations were shown to be the velocity variations accompanying a wave motion in the boundary layer. This wave motion was demonstrating the

characteristics predicted by stability theory based on the exponential growth of small disturbances. Their experiments were eventually a well proof of TS waves being the first stage of the transition process.

Compressibility makes this problem not only more realistic for most flow regimes, but also more complex. The studies on this issue start with Küchemann (1938). He was the first who tried to build a compressible linear stability theory. However, his studies were based on only inviscid theory and besides, he neglected the gradient of temperature as well as the curvature of the velocity profiles. The importance of these omissions was later handled by Lees and Lin [6]. Their theoretical investigations were concerned with the stability of laminar boundary layer in a compressible fluid (perfect gas) subjected to small disturbances. They concentrated on two-dimensional disturbance case just for simplicity of the mathematical analysis even though nothing claimed about two-dimensional case as being more unstable than three-dimensional case. The definition of relative Mach number and the classification of the flow were first introduced in this extensive study comprising both viscous and inviscid instability.

Spangler and Wells [7] performed experimental analysis to observe the effects of freestream disturbances on boundary layer transition. They investigated particularly the influences of acoustic noise fields having discrete frequencies and the broad-band turbulence created by coarse-mesh grids placed in the freestream. However, their study was deprived of a complete explanation about the relation between the transition and freestream disturbance energy. They mostly concentrated on visualizing the effects of these disturbances on transition. They showed that transition

location was independent of the acoustic standing waves unlike the traveling types. Besides, their results depicted that increasing effect of these acoustic disturbances coincides with the occurrence of energy peaks at lower frequencies. The corresponding Reynolds numbers in the experiments whereas, comprise a particular frequency range amplifying in the boundary layer.

The experimental studies of Pate and Schueler [8] were based on the aerodynamic noise and its influence on the boundary layer transition. For this purpose, they used different AEDC supersonic wind-tunnels having sharp leading edge two-dimensional hollow cylinder models or pitched flat plates. From their measurements, it was recognized that the wind tunnel size has a significant effect on transition criteria as well as the other well-known factors. Accordingly, as the tunnel size increases transition Reynolds number shows a continuous increase, on the contrary the radiated aerodynamic noise generated by the tunnel wall turbulent boundary layer decreases. Because they measured data for models different than zero angle flat plates, their numerical data are not appropriate for the present study. However, it brings a different point of view for the evaluations that's, for a trustable comparison of numerical values with the experimental transition criteria, one should necessarily use the ones developed by the same tunnel as much as possible.

In [9], Reshotko who was the first in calculating the wave numbers of the TS modes together with Lees in 1962 studied the stability of laminar boundary layer in a complex manner. His study was in a guidance format representing the effects of some factors on transition phenomena such as, wave number, Mach number and surface temperature. He employed the

linear theory for compressible oblique wave condition so as to indicate that the theoretical results can serve only as a guide for the experimental investigations. As he clarified, the theoretical transition Reynolds number as well as other information determined by the linear stability theory displays a qualitative agreement with the experimental transition criteria rather than a quantitative coherence. This should be taken into account if some discrepancies are observed in the current study whenever the comparisons take place.

Further studies of Reshotko [10] on instability and transition comprehend the theory of linear stability and its basic concepts such as normal mode analysis, parallel flow assumption, Squire's transformation, receptivity and its related factors etc. He mentioned about the Mach number, the surface cooling and surface curvature effects on stability not only for air but also for water as well. He summarized some of the transition prediction methods one of which is most commonly used Smith-Van Ingen e^n transition prediction technique based on linear theory that will be also be preferred in the present study. However, lack of results led his extensive study only as a guide or a review for stability theory including both plane and oblique wave conditions.

From 1960 up to now, the most comprehensive numerical investigation in compressible laminar boundary layers was performed by Mack who is known as the father of higher instability modes at supersonic speeds. He found that the first of these higher modes, named as *second mode,* is the dominant one for the zero pressure gradient boundary layers over the flat plates. This is why it is also referred to as the *Mack mode*. In [11], he

clarified the physical explanation for its occurrence as well as its numerical interpretation. His current study [11] is the most relevant to the present analysis. Here, he handled the incompressible stability problem as the preliminary case. Then, he studied the compressible stability theory for both two-and three-dimensional flows with plane/oblique waves in a much detailed format compared to other samples in literature. Mack provided the reader not only with the theoretical information but also the mathematical formulation for the compressible case. The effect of wave orientation on instability for both the TS and the second mode was another topic that he concentrated on.

Some of the results in [11] were represented in terms of spatial theory and some in terms of temporal theory. For 2D mean flows with plane waves from M=0 to M=3.8, Mack found that the critical Reynolds number increases meaning a stabilized flow. At M=4.5, he first observed the second mode at considerable wave numbers and immediately at M=4.8 he found that the first and the second modes join. In addition to these instability analyses, he made also transition prediction studies but only for incompressible flow case. All these results as well as the mathematical investigations are pretty much valuable for the present analysis and at every possible step they will be compared with the present cases.

Mack's earlier study [12] was conducted to numerical analysis to estimate the transition location at various Mach numbers including the supersonic speeds for two-dimensional laminar boundary layer over the flat plate being different from [11] where he dealt with mostly the instability problem. He investigated not only the effect of Mach number on transition in

adiabatic wall conditions but also the effect of cooling/heating at M=3. In both cases, he analyzed the problem using linear stability theory followed by e^n transition prediction technique. While investigating the Mach number effect, he used the stability characteristics in the most unstable condition, i.e., the angle at which the waves are most unstable for the prediction of transition. However, for the estimation of the n-factor, Mack formulated a new relation so as to make the results compatible with the experimental data. This methodology is exactly the same as what the present study will use in its calculations.

From the results, Mack [12] concluded that the transition occurs at further downstream from the leading edge from M=0 to M=1.5-1.6. From M=1.5-1.6 to M=4 whereas, this point moves towards the leading edge meaning an early transition and at higher speeds, it again moves downstream. From the comparison with the experimental data, he unfortunately could not obtain a perfect numerical coincidence but in conclusion, the results were quite satisfactory in qualitative aspect.

Arnal [2] performed an extended overview discussing the possibilities of the transition prediction over adiabatic flat plates with the use of linear theory and following, Smith-Van Ingen e^n transition prediction technique. Both two-dimensional and three-dimensional flows were taken into consideration. In two-dimensional flows, Arnal discussed the incompressible and compressible cases independently. He mentioned about both temporal and spatial amplification theories to inform the reader but, he preferred using the spatial variations of the waves while illustrating the numerical results.

Arnal in fact, did not go into detail in [2] about mathematical formulation of the stability problem except giving basic concepts and theoretical definitions similar to Reshotko [10]. But, the resultant stability characteristics that are represented in the form of instability diagrams for two-dimensional flows with plane waves at various flow speeds whereas, make this study distinguishable and quite valuable for the present arguments. These configurations depict the increase in the critical Reynolds number at higher Mach numbers up to M=3. Because Arnal did not present any result between M=3 an M=4.5, it would be wrong to claim that the range of Mach number where the flow is stabilized is exactly from M=0 to M=3. At M=4.5, the second mode was visualized where it joined the TS mode at M=4.8. Moreover, even though it was constrained with only one Mach number, M=4.5, the effect of wave angle (three-dimensionality of waves) on instability at higher speeds which was demonstrated again in the same format is precious for the present oblique wave analysis as well. According to this configuration, the second mode is stabilized whereas the first mode (TS mode) is destabilized with the increase of wave angle.

The further topics handled by Arnal [2] were the non-parallel effects on instability which will help to understand the validity of parallel flow assumption in the present analysis, and nonlinearities in transition process although they were not the scope of the study. He lastly maintained some parametric analyses illustrating the effect of pressure gradient, cooling/heating, nose bluntness etc.

In [13], Arnal summarized his extended theoretical study of [2] including the incompressible and compressible flows for both two- and three-dimensional flows. The discussion occupied again the plane wave and oblique wave cases but now, he mostly concentrated on transition prediction, the use of e^n technique and various approaches currently available to compute the n-factor giving the accurate transition location. He also included the shortcomings of this technique as well as its usefulness. The question of how the unstable waves are excited by the available disturbance environment, i.e., the receptivity problem was one of the topics discussed here. Arnal finally depicted some practical approaches to analyze the behavior of disturbances when nonlinearities occur in transition process.

Masad and Abid [14] investigated the instability at high speed boundary layer flows over the flat plates. They used the linear theory for both plane and oblique wave cases, and following they used e^n technique in order to predict the transition location in the most unstable flow condition. The first of higher modes and its attitude towards the Mach number were investigated for both adiabatic and cooled/heated flows. In adiabatic case, they well depicted the most unstable wave condition both for the first mode varying with Mach number (oblique waves) and for the second mode (plane waves). They used $n = 9$ while predicting the transition locations. The only deficiency of this study was the insufficient representation of the results.

Baines et al. [15] concentrated on describing a physical mechanism for the two-dimensional instability of a Blasius boundary layer with the growing TS waves. In their investigations the stability problem was handled in a different way, to explain the idealized form of the problem, i.e., inviscid

instability and the realistic type as viscous instability separately to find out their interaction to instability. They named these two cases as the inviscid mode and the viscous mode. Here, the concept of "mode" is absolutely irrelevant with the concept of "*mode*" used by Mack [11, 12] and the current study. One benefit of this study was to consider the disturbance amplitudes as varying with time not the space, i.e., to use temporal amplification theory which will be described and formulated in the present study together with its alternative. However, one should bear in mind that they did not contribute the compressibility effect to the problem hence the only gift they would bring the present analysis is the incompressible stability characteristics.

Hu and Zhong [16] solved the stability problem but for viscous compressible Couette flows unlike the present analysis concentrated on flat plate boundary layers. Nevertheless, their study was beneficial while making a physical description for the second mode, first of the higher modes and the reason why it is called the *acoustic mode*.

Özgen [17] solved the stability problem for two-dimensional incompressible flat plate boundary layers (single layer and two-layer) as well as the plane Poiseuille and plane Couette flows. Plane waves were under consideration in all cases. For the single-layer flows, the methodology was based on the linear theory for instability analysis and followed by the e^n prediction method for the transition estimation. The results were represented in the form of stability diagrams for various pressure gradient cases including the Blasius flow case.

Atalayer and Özgen [18] investigated the Mach number effect on the compressible two-dimensional boundary layers over the adiabatic flat plates. Only two-dimensional disturbances were handled in this study. For the instability analysis, they used the linear theory with the parallel flow assumption and the steady mean flow consideration. The temporal amplification theory was preferred while formulating the problem. The numerical solution was performed using the shooting technique. The resultant stability characteristics were demonstrated as constant temporal amplification curves showing the variation of wave number with the Reynolds number. For the transition analysis, e^n prediction method was applied. The Mach number range was not so wide but was enough for the illustration of the Mach number effect both on transition and on the instability.

1.5 Road Map

The mathematical modeling of the compressible stability problem will be performed starting from three-dimensional Navier-Stokes equations in Chapter 2. The formulation of linear stability theory will be given in a detailed format.

The next chapter will cover the numerical techniques that have been used for the solution of the stability problem. Brief information about the shooting technique that has been used in the current numerical integration, will take place as well as the other methods used for different purposes such

as Gram-Schmidt orthonormalization, Newton iteration and Simplex methods.

Chapter 4 will concentrate on the transition prediction mechanism, namely Smith-Van Ingen e^n transition prediction method accompanied by the methodology, its validity and the shortcomings of its use as well as its benefits. An argument about the estimation of n-factor will also be indicated in this chapter.

The results obtained throughout this study will be represented in Chapter 5 including the comparisons and discussions. The plane wave case, oblique wave case and the prediction of transition location will be handled as individual sections.

The last chapter will present a short summary about what has been performed throughout the current effort, what can be claimed about the results and their worth all under the heading of concluding remarks.

CHAPTER 2

LINEAR STABILITY THEORY

2.1 Introduction

Linear stability theory describes the behavior of the disturbances in the flow leading to transition of the boundary layer. It is mainly concerned with individual sine waves propagating in the boundary layer parallel to the wall. These instability waves are commonly referred as the *Tollmien-Schlichting* waves. Although their amplitudes show variation through the boundary layer, they are small enough so that the linear theory could be used. Their amplifications continue up to a point where breakdown to turbulence occurs.

The stability problem basically deals with the determination of the characteristics of these unstable disturbances internalized by the boundary layers. Compressibility makes this problem not only more realistic, but also more complex for most flow regimes as well. The studies on this issue start with Küchemann (1938). Lees and Lin (1946) follow him with their investigations on this topic.

In this chapter, the mathematical modeling of the compressible stability problem will be handled starting from the 3D Navier Stokes equations for a compressible boundary layer over an adiabatic flat plate. It will cover the linearization through the method of small disturbances. The fundamental tool for the linear stability theory, method of normal modes will also take place in the following sections. Brief information about the temporal and spatial theories will then be the last topic of the chapter.

2.2 Mathematical Modeling

The compressible stability theory starts with 3D Navier-Stokes equations for a viscous, heat conducting, perfect gas in Cartesian coordinates. For a Newtonian fluid, the momentum, energy, continuity equations and the equation of state are [11]:

$$\frac{\partial \bar{u}_i^*}{\partial t^*} + \bar{u}_j^* \frac{\partial \bar{u}_i^*}{\partial x_j^*} = \frac{1}{\bar{\rho}^*} \frac{\partial \bar{\tau}_{ij}^*}{\partial x_j^*}, \tag{2.1}$$

$$\bar{\rho}^* c_v^* \left[\frac{\partial \bar{T}^*}{\partial t^*} + \bar{u}_j^* \frac{\partial \bar{T}^*}{\partial x_j^*} \right] = \frac{\partial}{\partial x_j^*} \left[\bar{\kappa}^* \frac{\partial \bar{T}^*}{\partial x_j^*} \right] + \bar{\tau}_{ij}^* \bar{e}_{ij}^*, \tag{2.2}$$

$$\frac{\partial \bar{\rho}^*}{\partial t^*} + \frac{\partial (\bar{\rho}^* \bar{u}_j^*)}{\partial x_j^*} = 0, \tag{2.3}$$

$$\bar{p}^* = \bar{\rho}^* R^* \bar{T}^*, \tag{2.4}$$

where,

$$\bar{e}_{ij}^* = \frac{1}{2} \left[\frac{\partial \bar{u}_i^*}{\partial x_j^*} + \frac{\partial \bar{u}_j^*}{\partial x_i^*} \right], \tag{2.5}$$

$$\bar{\tau}_{ij}^{*} = 2\bar{\mu}^{*}\bar{e}_{ij}^{*} + \left[-\frac{2}{3}\bar{\mu}\bar{e}_{kk}^{*} - \bar{p}^{*}\right]\delta_{ij}, \tag{2.6}$$

denoting the dimensional quantities by asterisks '*' and time dependent quantities by over bars '¯'. According to the summation convention, $i, j = (1,2,3)$, $\bar{u}_i^{*} = (\bar{u}^{*}, \bar{v}^{*}, \bar{w}^{*})$ and $x_i^{*} = (x^{*}, y^{*}, z^{*})$. x^{*} being the streamwise coordinate, y^{*} the normal coordinate and z^{*} the spanwise coordinate, $\bar{u}^{*}$, $\bar{v}^{*}$ and $\bar{w}^{*}$ are the velocity components in x^{*}, y^{*} and z^{*} directions, respectively. R^{*} is the gas constant which is a different value for different gases. For a perfect gas as in this case, it becomes a *constant* independent of temperature.

The specific heat at constant volume c_v^{*} is normally a function of temperature. However, except for high-temperature chemically reacting flows, this coefficient can reasonably be taken as constant. In this study, although high temperatures at high Mach numbers will be most of the cases to be investigated, the chemical reactions will never be taken into consideration. For this reason, both specific heat constants c_v^{*} and c_p^{*} can be taken as constants [19]. The expanded forms of these equations are then as follows:

x-momentum equation:

$$\frac{\partial \bar{u}^{*}}{\partial t^{*}} + \bar{u}^{*}\frac{\partial \bar{u}^{*}}{\partial x^{*}} + \bar{v}^{*}\frac{\partial \bar{u}^{*}}{\partial y^{*}} + \bar{w}^{*}\frac{\partial \bar{u}^{*}}{\partial z^{*}} = \frac{1}{\bar{\rho}^{*}}\frac{\partial}{\partial x^{*}}\left[2\bar{\mu}^{*}\frac{\partial \bar{u}^{*}}{\partial x^{*}} - \frac{2}{3}\bar{\mu}^{*}\left(\frac{\partial \bar{u}^{*}}{\partial x^{*}} + \frac{\partial \bar{v}^{*}}{\partial y^{*}} + \frac{\partial \bar{w}^{*}}{\partial z^{*}}\right) - \bar{p}^{*}\right]$$
$$+ \frac{1}{\bar{\rho}^{*}}\frac{\partial}{\partial y^{*}}\left[\bar{\mu}^{*}\left(\frac{\partial \bar{u}^{*}}{\partial y^{*}} + \frac{\partial \bar{v}^{*}}{\partial x^{*}}\right)\right]$$
$$+ \frac{1}{\bar{\rho}^{*}}\frac{\partial}{\partial z^{*}}\left[\bar{\mu}^{*}\left(\frac{\partial \bar{u}^{*}}{\partial z^{*}} + \frac{\partial \bar{w}^{*}}{\partial x^{*}}\right)\right], \tag{2.7}$$

y-momentum equation:

$$\frac{\partial \bar{v}^*}{\partial t^*}+\bar{u}^*\frac{\partial \bar{v}^*}{\partial x^*}+\bar{v}^*\frac{\partial \bar{v}^*}{\partial y^*}+\bar{w}^*\frac{\partial \bar{v}^*}{\partial z^*}=\frac{1}{\bar{\rho}^*}\frac{\partial}{\partial x^*}\left[\bar{\mu}^*\left(\frac{\partial \bar{v}^*}{\partial x^*}+\frac{\partial \bar{u}^*}{\partial y^*}\right)\right]$$
$$+\frac{1}{\bar{\rho}^*}\frac{\partial}{\partial y^*}\left[2\bar{\mu}^*\frac{\partial \bar{v}^*}{\partial y^*}-\frac{2}{3}\bar{\mu}^*\left(\frac{\partial \bar{u}^*}{\partial x^*}+\frac{\partial \bar{v}^*}{\partial y^*}+\frac{\partial \bar{w}^*}{\partial z^*}\right)-\bar{p}^*\right]$$
$$+\frac{1}{\bar{\rho}^*}\frac{\partial}{\partial z^*}\left[\bar{\mu}^*\left(\frac{\partial \bar{v}^*}{\partial z^*}+\frac{\partial \bar{w}^*}{\partial y^*}\right)\right], \tag{2.8}$$

z-momentum equation:

$$\frac{\partial \bar{w}^*}{\partial t^*}+\bar{u}^*\frac{\partial \bar{w}^*}{\partial x^*}+\bar{v}^*\frac{\partial \bar{w}^*}{\partial y^*}+\bar{w}^*\frac{\partial \bar{w}^*}{\partial z^*}=\frac{1}{\bar{\rho}^*}\frac{\partial}{\partial x^*}\left[\bar{\mu}^*\left(\frac{\partial \bar{w}^*}{\partial x^*}+\frac{\partial \bar{u}^*}{\partial z^*}\right)\right]$$
$$+\frac{1}{\bar{\rho}^*}\frac{\partial}{\partial y^*}\left[\bar{\mu}^*\left(\frac{\partial \bar{w}^*}{\partial y^*}+\frac{\partial \bar{v}^*}{\partial z^*}\right)\right],$$
$$+\frac{1}{\bar{\rho}^*}\frac{\partial}{\partial z^*}\left[2\bar{\mu}^*\frac{\partial \bar{w}^*}{\partial z^*}-\frac{2}{3}\bar{\mu}^*\left(\frac{\partial \bar{u}^*}{\partial x^*}+\frac{\partial \bar{v}^*}{\partial y^*}+\frac{\partial \bar{w}^*}{\partial z^*}\right)-\bar{p}^*\right], \tag{2.9}$$

energy equation:

$$\bar{\rho}^* c_v^*\left[\frac{\partial \bar{T}^*}{\partial t^*}+\bar{u}^*\frac{\partial \bar{T}^*}{\partial x^*}+\bar{v}^*\frac{\partial \bar{T}^*}{\partial y^*}+\bar{w}^*\frac{\partial \bar{T}^*}{\partial z^*}\right]=$$
$$-\bar{p}^*\left(\frac{\partial \bar{u}^*}{\partial x^*}+\frac{\partial \bar{v}^*}{\partial y^*}+\frac{\partial \bar{w}^*}{\partial z^*}\right)+\frac{\partial}{\partial x^*}\left(\bar{\kappa}^*\frac{\partial \bar{T}^*}{\partial x^*}\right)+\frac{\partial}{\partial y^*}\left(\bar{\kappa}^*\frac{\partial \bar{T}^*}{\partial y^*}\right)+\frac{\partial}{\partial z^*}\left(\bar{\kappa}^*\frac{\partial \bar{T}^*}{\partial z^*}\right)$$
$$+\bar{\mu}^*\left[2\left(\left(\frac{\partial \bar{u}^*}{\partial x^*}\right)^2+\left(\frac{\partial \bar{v}^*}{\partial y^*}\right)^2+\left(\frac{\partial \bar{w}^*}{\partial z^*}\right)^2\right)+\left(\frac{\partial \bar{u}^*}{\partial z^*}+\frac{\partial \bar{w}^*}{\partial x^*}\right)^2+\left(\frac{\partial \bar{u}^*}{\partial y^*}+\frac{\partial \bar{v}^*}{\partial x^*}\right)^2\right.$$
$$\left.+\left(\frac{\partial \bar{v}^*}{\partial z^*}+\frac{\partial \bar{w}^*}{\partial y^*}\right)^2-\frac{2}{3}\left(\frac{\partial \bar{u}^*}{\partial x^*}+\frac{\partial \bar{v}^*}{\partial y^*}+\frac{\partial \bar{w}^*}{\partial z^*}\right)^2\right], \tag{2.10}$$

continuity equation:

$$\frac{\partial \bar{\rho}^*}{\partial t^*} + \frac{\partial}{\partial x^*}\left(\bar{\rho}^* \bar{u}^*\right) + \frac{\partial}{\partial y^*}\left(\bar{\rho}^* \bar{v}^*\right) + \frac{\partial}{\partial z^*}\left(\bar{\rho}^* \bar{w}^*\right) = 0, \tag{2.11}$$

equation of state:

$$\bar{p}^* = \bar{\rho}^* R^* \bar{T}^*. \tag{2.12}$$

2.2.1 Method of Small Disturbances

The next step in derivation of the linear stability equations is the application of *method of small disturbances* to the equations of motion (Eqs. (2.7)-(2.12)). According to the small disturbance theory, each instantaneous flow property is divided into a steady mean (basic) flow term and an unsteady fluctuating term such that [11, 17, 20]:

$$\begin{aligned}
&\bar{u}_i^* = U_i^*(x^*, y^*, z^*) + \hat{u}_i^*(x^*, y^*, z^*, t^*), \qquad i=1,3,\\
&\bar{p}^* = P^*(x^*, y^*, z^*) + \hat{p}^*(x^*, y^*, z^*, t^*),\\
&\bar{T}^* = T^*(x^*, y^*, z^*) + \hat{T}^*(x^*, y^*, z^*, t^*),\\
&\bar{\rho}^* = \rho^*(x^*, y^*, z^*) + \hat{\rho}^*(x^*, y^*, z^*, t^*),\\
&\bar{\mu}^* = \mu^*(x^*, y^*, z^*) + \hat{\mu}^*(x^*, y^*, z^*, t^*),\\
&\bar{\kappa}^* = \kappa^*(x^*, y^*, z^*) + \hat{\kappa}^*(x^*, y^*, z^*, t^*),
\end{aligned} \tag{2.13}$$

where '$\hat{}$' denotes the fluctuations. The mean Cartesian velocity components U^*, V^*, W^*, the pressure P^*, the temperature T^*, the density ρ^*, the viscosity μ^* and the coefficient of thermal conductivity κ^*, which altogether define the mean (basic) flow, should be known a priori numerically, experimentally or

theoretically. The basic flow could be two- or three-dimensional, steady or unsteady, incompressible or compressible as long as it satisfies the equations of motion. In this study, attention will be focused on a *two-dimensional*, *steady* and *compressible* basic flow although the equations will be derived for a *three-dimensional* basic flow.

The fluctuating terms defined in Eqs. (2.13) are so small that the quadratic terms of the disturbances (such as $\hat{v}^*\partial\hat{u}^*/\partial y^*$) are dropped in the equations during the rearrangements. A further simplification is the *parallel flow assumption*. According to that assumption, the mean flow quantities do not vary significantly over a wavelength of the disturbances. Therefore, the streamwise and the spanwise mean velocity components, U^* and W^* as well as the temperature T^* and the density ρ^* are functions of y^* only. However, because the normal velocity component V^* is too small compared to the streamwise and spanwise velocity components, it is accepted as zero, i.e. $V^* = 0$.

In words, for a parallel flow, the streamlines are everywhere parallel to each other. Physically, it implies that the flow stability at a particular station (x,z) is determined by the local flow properties of that station independent from all others. It is important to note that, for a Couette flow or Poiseuille flow, this assumption is obviously exact whereas, for a boundary layer flow it is just a good approximation [2, 10] (see Chapter 4).

As a further assumption in this study, the transport coefficients μ^* and κ^* are accepted to be the functions of T^* only. Then, their fluctuations become [11]:

$$\hat{\mu}^* = \frac{d\mu^*}{dT^*}\hat{T}^*, \qquad \hat{\kappa}^* = \frac{d\kappa^*}{dT^*}\hat{T}^*. \tag{2.14}$$

It is important to notice that, T^* is a y^* dependent quantity, therefore these transport coefficients become also the functions of y^*. Accordingly, the derivatives of these coefficients with respect to x^*, y^* and z^* are expressed as:

$$\frac{\partial\hat{\mu}^*}{\partial x^*} = \frac{d\mu^*}{dT^*}\frac{\partial\hat{T}^*}{\partial x^*}, \qquad \frac{\partial\hat{\mu}^*}{\partial y^*} = \frac{d\mu^*}{dT^*}\frac{\partial\hat{T}^*}{\partial y^*} + \frac{d^2\mu^*}{dT^{*2}}\frac{dT^*}{dy^*}\hat{T}^*, \qquad \frac{\partial\hat{\mu}^*}{\partial z^*} = \frac{d\mu^*}{dT^*}\frac{\partial\hat{T}^*}{\partial z^*}, \tag{2.15}$$

$$\frac{\partial\hat{\kappa}^*}{\partial x^*} = \frac{d\kappa^*}{dT^*}\frac{\partial\hat{T}^*}{\partial x^*}, \qquad \frac{\partial\hat{\kappa}^*}{\partial y^*} = \frac{d\kappa^*}{dT^*}\frac{\partial\hat{T}^*}{\partial y^*} + \frac{d^2\kappa^*}{dT^{*2}}\frac{dT^*}{dy^*}\hat{T}^*, \qquad \frac{\partial\hat{\kappa}^*}{\partial z^*} = \frac{d\kappa^*}{dT^*}\frac{\partial\hat{T}^*}{\partial z^*}. \tag{2.16}$$

Substituting the instantaneous flow quantities defined by Eqs. (2.13) into Eqs. (2.7)-(2.12), applying the parallel flow assumption, neglecting the quadratic terms of fluctuations and making necessary rearrangements for a three-dimensional, steady, compressible flow, the equations of motion become:

x-momentum equation:

$$\begin{aligned}
\rho^*\left[\frac{\partial\hat{u}^*}{\partial t^*} + U^*\frac{\partial\hat{u}^*}{\partial x^*} + \hat{v}^*\frac{dU^*}{dy^*} + W^*\frac{\partial\hat{u}^*}{\partial z^*}\right] = \\
&-\frac{\partial\hat{p}^*}{\partial x^*} + \mu^*\left[2\frac{\partial^2\hat{u}^*}{\partial x^{*2}} - \frac{2}{3}\left(\frac{\partial^2\hat{u}^*}{\partial x^{*2}} + \frac{\partial^2\hat{v}^*}{\partial x^*\partial y^*} + \frac{\partial^2\hat{w}^*}{\partial x^*\partial z^*}\right)\right] \\
&+\mu^*\left[\frac{\partial^2\hat{u}^*}{\partial y^{*2}} + \frac{\partial^2\hat{v}^*}{\partial x^*\partial y^*} + \frac{\partial^2\hat{u}^*}{\partial z^{*2}} + \frac{\partial^2\hat{w}^*}{\partial x^*\partial z^*}\right] + \frac{d\mu^*}{dT^*}\frac{dT^*}{dy^*}\left[\frac{\partial\hat{u}^*}{\partial y^*} + \frac{\partial\hat{v}^*}{\partial x^*}\right] \\
&+\left[\frac{d\mu^*}{dT^*}\frac{\partial\hat{T}^*}{\partial y^*} + \frac{d^2\mu^*}{dT^{*2}}\frac{dT^*}{dy^*}\hat{T}^*\right]\frac{dU^*}{dy^*} + \frac{d^2U^*}{dy^{*2}}\frac{d\mu^*}{dT^*}\hat{T}^*,
\end{aligned} \tag{2.17}$$

y-momentum equation:

$$\rho^*\left[\frac{\partial \hat{v}^*}{\partial t^*}+U^*\frac{\partial \hat{v}^*}{\partial x^*}+W^*\frac{\partial \hat{v}^*}{\partial z^*}\right]=$$

$$-\frac{\partial \hat{p}^*}{\partial y^*}+\mu^*\left[2\frac{\partial^2 \hat{v}^*}{\partial y^{*2}}-\frac{2}{3}\left(\frac{\partial^2 \hat{u}^*}{\partial x^*\partial y^*}+\frac{\partial^2 \hat{v}^*}{\partial y^{*2}}+\frac{\partial^2 \hat{w}^*}{\partial y^*\partial z^*}\right)\right]$$

$$+\mu^*\left[\frac{\partial^2 \hat{v}^*}{\partial x^{*2}}+\frac{\partial^2 \hat{u}^*}{\partial x^*\partial y^*}+\frac{\partial^2 \hat{v}^*}{\partial z^{*2}}+\frac{\partial^2 \hat{w}^*}{\partial y^*\partial z^*}\right]+\frac{d\mu^*}{dT^*}\frac{\partial \hat{T}^*}{\partial z^*}\frac{dW^*}{dy^*}$$

$$+\frac{d\mu^*}{dT^*}\frac{dT^*}{dy^*}\left[2\frac{\partial \hat{v}^*}{\partial y^*}-\frac{2}{3}\left(\frac{\partial \hat{u}^*}{\partial x^*}+\frac{\partial \hat{v}^*}{\partial y^*}+\frac{\partial \hat{w}^*}{\partial z^*}\right)\right]+\frac{d\mu^*}{dT^*}\frac{\partial \hat{T}^*}{\partial x^*}\frac{dU^*}{dy^*}, \qquad (2.18)$$

z-momentum equation:

$$\rho^*\left[\frac{\partial \hat{w}^*}{\partial t^*}+U^*\frac{\partial \hat{w}^*}{\partial x^*}+\hat{v}^*\frac{dW^*}{dy^*}+W^*\frac{\partial \hat{w}^*}{\partial z^*}\right]=$$

$$-\frac{\partial \hat{p}^*}{\partial z^*}+\mu^*\left[2\frac{\partial^2 \hat{w}^*}{\partial z^{*2}}-\frac{2}{3}\left(\frac{\partial^2 \hat{u}^*}{\partial x^*\partial z^*}+\frac{\partial^2 \hat{v}^*}{\partial y^*\partial z^*}+\frac{\partial^2 \hat{w}^*}{\partial z^{*2}}\right)\right]$$

$$+\mu^*\left[\frac{\partial^2 \hat{w}^*}{\partial x^{*2}}+\frac{\partial^2 \hat{u}^*}{\partial x^*\partial z^*}+\frac{\partial^2 \hat{w}^*}{\partial y^{*2}}+\frac{\partial^2 \hat{v}^*}{\partial y^*\partial z^*}\right]+\frac{d\mu^*}{dT^*}\frac{dT^*}{dy^*}\left[\frac{\partial \hat{w}^*}{\partial y^*}+\frac{\partial \hat{v}^*}{\partial z^*}\right]$$

$$+\left[\frac{d\mu^*}{dT^*}\frac{\partial \hat{T}^*}{\partial y^*}+\frac{d^2\mu^*}{dT^{*2}}\frac{dT^*}{dy^*}\hat{T}^*\right]\frac{dW^*}{dy^*}+\frac{d^2W^*}{dy^{*2}}\frac{d\mu^*}{dT^*}\hat{T}^*, \qquad (2.19)$$

energy equation:

$$\rho^* c_v^* \left[\frac{\partial \hat{T}^*}{\partial t^*} + U^* \frac{\partial \hat{T}^*}{\partial x^*} + \hat{v}^* \frac{dT^*}{dy^*} + W^* \frac{\partial \hat{T}^*}{\partial z^*} \right] =$$

$$-P^* \left(\frac{\partial \hat{u}^*}{\partial x^*} + \frac{\partial \hat{v}^*}{\partial y^*} + \frac{\partial \hat{w}^*}{\partial z^*} \right) + \frac{d\kappa^*}{dT^*} \frac{dT^*}{dy^*} \frac{\partial \hat{T}^*}{\partial y^*} + \left[\frac{d^2\kappa^*}{dT^{*2}} \frac{dT^*}{dy^*} \hat{T}^* + \frac{\partial \hat{T}^*}{\partial y^*} \frac{d\kappa^*}{dT^*} \right] \frac{dT^*}{dy^*}$$

$$+\kappa^* \left[\frac{\partial^2 \hat{T}^*}{\partial x^{*2}} + \frac{\partial^2 \hat{T}^*}{\partial y^{*2}} + \frac{\partial^2 \hat{T}^*}{\partial z^{*2}} \right] + \frac{d\kappa^*}{dT^*} \frac{d^2T^*}{dy^{*2}} \hat{T}^* + \frac{d\mu^*}{dT^*} \hat{T}^* \left[\left(\frac{dU^*}{dy^*} \right)^2 + \left(\frac{dW^*}{dy^*} \right)^2 \right]$$

$$+2\mu^* \left[\frac{dU^*}{dy^*} \left(\frac{\partial \hat{u}^*}{\partial y^*} + \frac{\partial \hat{v}^*}{\partial x^*} \right) + \frac{dW^*}{dy^*} \left(\frac{\partial \hat{v}^*}{\partial z^*} + \frac{\partial \hat{w}^*}{\partial y^*} \right) \right], \qquad (2.20)$$

continuity equation:

$$\frac{\partial \hat{\rho}^*}{\partial t^*} + \rho^* \left[\frac{\partial \hat{u}^*}{\partial x^*} + \frac{\partial \hat{v}^*}{\partial y^*} + \frac{\partial \hat{w}^*}{\partial z^*} \right] + U^* \frac{\partial \hat{\rho}^*}{\partial x^*} + \hat{v}^* \frac{d\rho^*}{dy^*} + W^* \frac{\partial \hat{\rho}^*}{\partial z^*} = 0, \qquad (2.21)$$

equation of state:

$$\hat{p}^* = \rho^* R^* \hat{T}^* + \hat{\rho}^* R^* T^*. \qquad (2.22)$$

Next, the resulting equations are nondimensionalized. Accordingly, the velocity components are made dimensionless by the local freestream velocity U_e^*, the distances by a reference length scale L^* (Blasius length scale, $L^* = \sqrt{\nu_e^* x^* / U_e^*}$), the temperatures by the freestream temperature T_e^*, the density by freestream density ρ_e^*, the dynamic viscosity by the freestream viscosity μ_e^* and the pressures by the freestream pressure P_e^*. Note that, the mean pressure component, P^* is constant along the y direction in the boundary layer. This makes the nondimensional mean pressure value, P unity and the nondimensional perfect gas relation for mean flow as $\rho T = 1$.

Also, by making the time, t^* dimensionless with the use of L^*/U_e^*, one ends up with the following dimensionless equations:

x-momentum equation:

$$\rho\left[\frac{\partial\hat{u}}{\partial t}+U\frac{\partial\hat{u}}{\partial x}+\hat{v}\frac{dU}{dy}+W\frac{\partial\hat{u}}{\partial z}\right]=$$

$$-\frac{1}{\gamma M^2}\frac{\partial\hat{p}}{\partial x}+\frac{\mu}{R}\left[2\frac{\partial^2\hat{u}}{\partial x^2}-\frac{2}{3}\left(\frac{\partial^2\hat{u}}{\partial x^2}+\frac{\partial^2\hat{v}}{\partial x\partial y}+\frac{\partial^2\hat{w}}{\partial x\partial z}\right)\right]$$

$$+\frac{\mu}{R}\left[\frac{\partial^2\hat{u}}{\partial y^2}+\frac{\partial^2\hat{v}}{\partial x\partial y}+\frac{\partial^2\hat{u}}{\partial z^2}+\frac{\partial^2\hat{w}}{\partial x\partial z}\right]+\frac{1}{R}\frac{d\mu}{dT}\frac{dT}{dy}\left[\frac{\partial\hat{u}}{\partial y}+\frac{\partial\hat{v}}{\partial x}\right]$$

$$+\frac{1}{R}\left[\frac{d\mu}{dT}\left(\frac{\partial\hat{T}}{\partial y}\frac{dU}{dy}+\frac{d^2U}{dy^2}\hat{T}\right)+\frac{d^2\mu}{dT^2}\frac{dT}{dy}\frac{dU}{dy}\hat{T}\right], \qquad (2.23)$$

y-momentum equation:

$$\rho\left[\frac{\partial\hat{v}}{\partial t}+U\frac{\partial\hat{v}}{\partial x}+W\frac{\partial\hat{v}}{\partial z}\right]=$$

$$-\frac{1}{\gamma M^2}\frac{\partial\hat{p}}{\partial y}+\frac{\mu}{R}\left[2\frac{\partial^2\hat{v}}{\partial y^2}-\frac{2}{3}\left(\frac{\partial^2\hat{u}}{\partial x\partial y}+\frac{\partial^2\hat{v}}{\partial y^2}+\frac{\partial^2\hat{w}}{\partial y\partial z}\right)\right]$$

$$+\frac{\mu}{R}\left[\frac{\partial^2\hat{v}}{\partial x^2}+\frac{\partial^2\hat{u}}{\partial x\partial y}+\frac{\partial^2\hat{v}}{\partial z^2}+\frac{\partial^2\hat{w}}{\partial y\partial z}\right]-\frac{2}{3}\frac{1}{R}\frac{d\mu}{dT}\frac{dT}{dy}\left[\frac{\partial\hat{u}}{\partial x}+\frac{\partial\hat{v}}{\partial y}+\frac{\partial\hat{w}}{\partial z}\right]$$

$$+\frac{1}{R}\frac{d\mu}{dT}\left[2\frac{dT}{dy}\frac{\partial\hat{v}}{\partial y}+\frac{\partial\hat{T}}{\partial x}\frac{dU}{dy}+\frac{\partial\hat{T}}{\partial z}\frac{dW}{dy}\right], \qquad (2.24)$$

z-momentum equation:

$$\rho\left[\frac{\partial \hat{w}}{\partial t}+U\frac{\partial \hat{w}}{\partial x}+\hat{v}\frac{dW}{dy}+W\frac{\partial \hat{w}}{\partial z}\right]=$$

$$-\frac{1}{\gamma M^2}\frac{\partial \hat{p}}{\partial z}+\frac{\mu}{R}\left[2\frac{\partial^2 \hat{w}}{\partial z^2}-\frac{2}{3}\left(\frac{\partial^2 \hat{u}}{\partial x\partial z}+\frac{\partial^2 \hat{v}}{\partial y\partial z}+\frac{\partial^2 \hat{w}}{\partial z^2}\right)\right]$$

$$+\frac{\mu}{R}\left[\frac{\partial^2 \hat{w}}{\partial x^2}+\frac{\partial^2 \hat{u}}{\partial x\partial z}+\frac{\partial^2 \hat{w}}{\partial y^2}+\frac{\partial^2 \hat{v}}{\partial y\partial z}\right]+\frac{1}{R}\frac{d\mu}{dT}\frac{dT}{dy}\left[\frac{\partial \hat{w}}{\partial y}+\frac{\partial \hat{v}}{\partial z}\right]$$

$$+\frac{1}{R}\left[\frac{d\mu}{dT}\left(\frac{\partial \hat{T}}{\partial y}\frac{dW}{dy}+\frac{d^2W}{dy^2}\hat{T}\right)+\frac{d^2\mu}{dT^2}\frac{dT}{dy}\frac{dW}{dy}\hat{T}\right], \tag{2.25}$$

energy equation:

$$\rho\left[\frac{\partial \hat{T}}{\partial t}+U\frac{\partial \hat{T}}{\partial x}+\hat{v}\frac{dT}{dy}+W\frac{\partial \hat{T}}{\partial z}\right]=$$

$$-(\gamma-1)\left[\frac{\partial \hat{u}}{\partial x}+\frac{\partial \hat{v}}{\partial y}+\frac{\partial \hat{w}}{\partial z}\right]+\frac{\gamma\mu}{Pr\,R}\left[\frac{2}{\kappa}\frac{d\kappa}{dT}\frac{dT}{dy}\frac{\partial \hat{T}}{\partial y}+\frac{1}{\kappa}\frac{d^2\kappa}{dT^2}\left(\frac{dT}{dy}\right)^2\hat{T}\right]$$

$$+\frac{\gamma\mu}{Pr\,R}\left[\frac{1}{\kappa}\frac{d\kappa}{dT}\frac{d^2T}{dy^2}\hat{T}+\left(\frac{\partial^2 \hat{T}}{\partial x^2}+\frac{\partial^2 \hat{T}}{\partial y^2}+\frac{\partial^2 \hat{T}}{\partial z^2}\right)\right]$$

$$+\frac{\gamma(\gamma-1)M^2}{R}2\mu\left[\frac{dU}{dy}\left(\frac{\partial \hat{u}}{\partial y}+\frac{\partial \hat{v}}{\partial x}\right)+\frac{dW}{dy}\left(\frac{\partial \hat{v}}{\partial z}+\frac{\partial \hat{w}}{\partial y}\right)\right]$$

$$+\frac{\gamma(\gamma-1)M^2}{R}\frac{d\mu}{dT}\hat{T}\left[\left(\frac{dU}{dy}\right)^2+\left(\frac{dW}{dy}\right)^2\right], \tag{2.26}$$

continuity equation:

$$\frac{\partial \hat{\rho}}{\partial t}+\rho\left[\frac{\partial \hat{u}}{\partial x}+\frac{\partial \hat{v}}{\partial y}+\frac{\partial \hat{w}}{\partial z}\right]+U\frac{\partial \hat{\rho}}{\partial x}+\hat{v}\frac{d\rho}{dy}+W\frac{\partial \hat{\rho}}{\partial z}=0, \tag{2.27}$$

equation of state:

$$\hat{p} = \rho\hat{T} + \hat{\rho}T \text{ or, } \hat{p} = \frac{\hat{\rho}}{\rho} + \frac{\hat{T}}{T}, \tag{2.28}$$

because the local mean pressure equals to the freestream mean pressure and the nondimensional perfect gas relation reduces to $\rho T = 1$. The boundary conditions, in dimensionless form, are whereas:

$$\text{No slip BC} \rightarrow \hat{u}(0) = \hat{v}(0) = \hat{w}(0) = \hat{T}(0) = 0,$$
$$\text{Freestream BC} \rightarrow \hat{u}(y), \hat{v}(y), \hat{w}(y), \hat{T}(y) \rightarrow 0 \text{ as } y \rightarrow \infty. \tag{2.29}$$

Eqs. (2.23)-(2.28) and the boundary conditions in Eq. (2.29) define a nondimensional linear system of equations for a compressible, adiabatic boundary layer flow with the assumptions of parallel flow and small fluctuations. The expressions of the parameters that are used for nondimensionalizing the equations are:

$$c_v^* = \frac{R^*}{\gamma - 1}, \qquad R^* = c_p^* - c_v^*. \tag{2.30}$$

where, R^* is the specific gas constant, c_p^*, c_v^* are the specific heats at constant pressure and volume, respectively and γ is the ratio of specific heats. Notice that, this ratio is automatically being constant since, as mentioned previously, both specific heats are accepted to be constant throughout this study. The other parameters introduced in Eqs. (2.23)-(2.28), i.e. the dimensionless coefficient of thermal conductivity and the Prandtl number are also expressed as:

$$\kappa = \frac{\kappa^*}{c_p^* \mu_e^*}, \qquad \Pr = \mu^* \frac{c_p^*}{\kappa^*}, \tag{2.31}$$

so that, $\mu = \Pr.\kappa$. $\Pr$, in general, is a function of temperature. However, since the temperature variations of μ^* and κ^* are almost identical even at high temperatures, and additionally, since the specific heats are treated as constants, this nondimensional parameter is essentially taken as *constant* up to the temperatures on the order of 10^3 Kelvin [19, 21].

Noting that L^* is defined as the Blasius length scale [4, 11], the freestream Mach number and the Reynolds number are defined as:

$$M = \frac{U_e^*}{\sqrt{\gamma R^* T_e^*}}, \qquad R = \frac{\rho_e^* U_e^* L^*}{\mu_e^*}. \tag{2.32}$$

2.2.2 Normal Mode Analysis

One way of computing the range of unstable waves is to introduce small disturbances into the dimensionless, linearized system of equations in the form of normal modes. In the normal mode analysis, the disturbances are considered to be horizontal waves in x-z plane represented by the following:

$$\hat{\varphi}(x, y, z, t) = \bar{\varphi}(y) e^{i(\alpha x + \beta z - \omega t)}, \tag{2.33}$$

where, '$\hat{}$' shows the fluctuating quantities and '$\bar{}$' the corresponding complex disturbance amplitude functions. α and β are x and z components

of the wave number vector $\vec{k}$, respectively. ω is the complex frequency that is found by $\omega = k.c$. Here, k represents the magnitude of the wave number vector which is obtained by $\sqrt{\alpha^2 + \beta^2}$ and c represents the wave velocity.

For a two-dimensional boundary layer, these fluctuations propagating in the local freestream direction are called *two-dimensional disturbances*, whereas those propagating through some angle to that direction are called *three-dimensional disturbances* [10]. In the present thesis, two-dimensional instability analysis will be performed as a preliminary step for the oblique wave analysis (see Chapter 5).

For the velocity, pressure, density and the temperature fluctuations, Eq. (2.33) takes the following forms:

$$\hat{u}(x,y,z,t) = \bar{u}(y)e^{i(\alpha x+\beta z-\omega t)},$$
$$\hat{v}(x,y,z,t) = \bar{v}(y)e^{i(\alpha x+\beta z-\omega t)},$$
$$\hat{w}(x,y,z,t) = \bar{w}(y)e^{i(\alpha x+\beta z-\omega t)},$$
$$\hat{p}(x,y,z,t) = \bar{p}(y)e^{i(\alpha x+\beta z-\omega t)},$$
$$\hat{\rho}(x,y,z,t) = \bar{\rho}(y)e^{i(\alpha x+\beta z-\omega t)},$$
$$\hat{T}(x,y,z,t) = \bar{T}(y)e^{i(\alpha x+\beta z-\omega t)}. \qquad (2.34)$$

Each of the parameters, α, β and ω can be either complex or real. If α, β and ω are all real, the wave is neutrally stable propagating in the x-z plane with constant amplitude and wave velocity, $c = \omega/k$. Any of them being complex means that the amplitude will change through the wave

propagation. In any case, the physical solutions are the real parts of these normal modes.

Substituting Eqs. (2.34) into the dimensionless, linearized system of equations (Eqs. (2.23)-(2.28)) and performing the necessary algebra, one can reach the following system:

x-momentum equation:

$$\rho\left[-i\omega\bar{u}+i\alpha U\bar{u}+U'\bar{v}+i\beta W\bar{u}\right]=$$
$$-\frac{i\alpha}{\gamma M^2}\bar{p}+\frac{\mu}{R}\left[-2\alpha^2\bar{u}+\bar{u}''+i\alpha\bar{v}'-\beta^2\bar{u}-\alpha\beta\bar{w}-\frac{2}{3}\left(-\alpha^2\bar{u}+i\alpha\bar{v}'-\alpha\beta\bar{w}\right)\right]$$
$$+\frac{1}{R}\left[\frac{d\mu}{dT}\left(T'\left(\bar{u}'+i\alpha\bar{v}\right)+\left(U'\bar{T}'+U''\bar{T}\right)\right)+\frac{d^2\mu}{dT^2}U'T'\bar{T}\right], \qquad (2.35)$$

y-momentum equation:

$$\rho\left[-i\omega\bar{v}+i\alpha U\bar{v}+i\beta W\bar{v}\right]=$$
$$-\frac{1}{\gamma M^2}\bar{p}'+\frac{\mu}{R}\left[2\bar{v}''-\beta^2\bar{v}+i\beta\bar{w}'-\alpha^2\bar{v}+i\alpha\bar{u}'-\frac{2}{3}\left(i\alpha\bar{u}'+\bar{v}''+i\beta\bar{w}'\right)\right]$$
$$+\frac{1}{R}\frac{d\mu}{dT}\left[\left(2T'\bar{v}'+i\alpha U'\bar{T}+i\beta W'\bar{T}\right)-\frac{2}{3}T'\left(i\alpha\bar{u}+\bar{v}'+i\beta\bar{w}\right)\right], \qquad (2.36)$$

z-momentum equation:

$$\rho\left[-i\omega\bar{w}+i\alpha U\bar{w}+W'\bar{v}+i\beta W\bar{w}\right]=$$
$$-\frac{i\beta}{\gamma M^2}\bar{p}+\frac{\mu}{R}\left[-2\beta^2\bar{w}+\bar{w}''+i\beta\bar{v}'-\alpha^2\bar{w}-\alpha\beta\bar{u}-\frac{2}{3}\left(-\beta^2\bar{w}+i\beta\bar{v}'-\alpha\beta\bar{u}\right)\right]$$
$$+\frac{1}{R}\left[\frac{d\mu}{dT}\left(T'\left(\bar{w}'+i\beta\bar{v}\right)+\left(W'\bar{T}'+W''\bar{T}\right)\right)+\frac{d^2\mu}{dT^2}W'T'\bar{T}\right], \qquad (2.37)$$

energy equation:

$$\rho\left[-i\omega\bar{T}+i\alpha U\bar{T}+T'\bar{v}+i\beta W\bar{T}\right]=$$

$$-(\gamma-1)\left[i\alpha\bar{u}+\bar{v}'+i\beta\bar{w}\right]+\frac{\gamma\mu}{\mathrm{Pr}\,R}\left[\frac{2}{\kappa}\frac{d\kappa}{dT}T'\bar{T}'+\frac{1}{\kappa}\frac{d^2\kappa}{dT^2}(T')^2\,\bar{T}\right]$$

$$+\frac{\gamma\mu}{\mathrm{Pr}\,R}\left[\frac{1}{\kappa}\frac{d\kappa}{dT}T''\bar{T}+\left(-\alpha^2\bar{T}+\bar{T}''-\beta^2\bar{T}\right)\right]$$

$$+\frac{\gamma(\gamma-1)M^2}{R}2\mu\left[U'\left(\bar{u}'+i\alpha\bar{v}\right)+W'\left(\bar{w}'+i\beta\bar{v}\right)\right]$$

$$+\frac{\gamma(\gamma-1)M^2}{R}\frac{d\mu}{dT}\bar{T}\left[U'^2+W'^2\right], \qquad (2.38)$$

continuity equation:

$$i\left[\alpha U+\beta W-\omega\right]\bar{\rho}+\rho\left[\bar{v}'+i\alpha\bar{u}+i\beta\bar{w}\right]+\rho'\bar{v}=0, \qquad (2.39)$$

equation of state:

$$\bar{p}=\frac{\bar{\rho}}{\rho}+\frac{\bar{T}}{T}, \qquad (2.40)$$

and the following boundary conditions:

$$\text{No slip BC}\rightarrow\bar{u}(0)=\bar{v}(0)=\bar{w}(0)=\bar{T}(0)=0,$$

$$\text{Freestream BC}\rightarrow\bar{u}(y),\bar{v}(y),\bar{w}(y),\bar{T}(y)\rightarrow 0\ \text{ as }\ y\rightarrow\infty, \qquad (2.41)$$

where, prime (') defines the derivative with respect to dimensionless y distance (i.e., d/dy).

2.2.3 Eighth Order System

Eqs. (2.35)-(2.41) form an eighth order system having the variables of $\bar{u}$, $\bar{v}$, $\bar{w}$, $\bar{p}$, $\bar{T}$, $\bar{\rho}$, $\bar{u}'$ and $\bar{w}'$. It is necessary to mention that the system is referred to as *eighth order* not because of its order of highest derivative but, because it has eight variables. However, the equations are not yet the most convenient form of equations of compressible stability theory. A further rearrangement is on the momentum equations considering the direction of wave number vector, $\vec{k}$. Meanwhile, the variables of the new system also change.

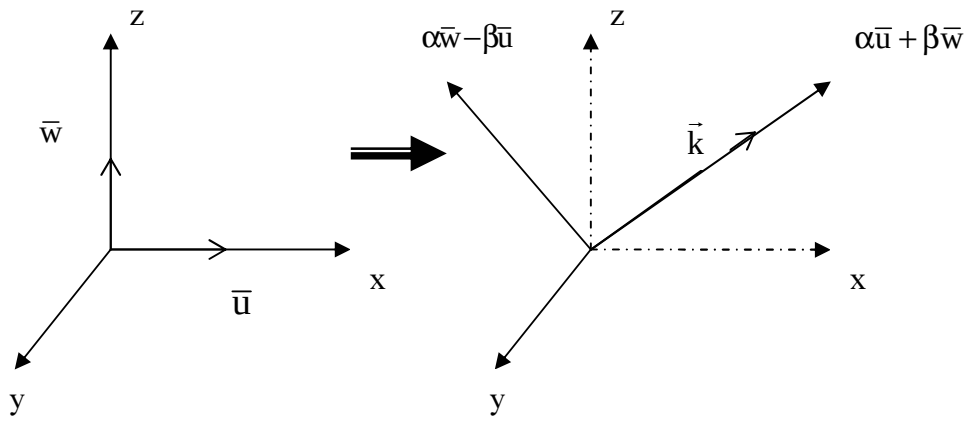

Figure 2.1 Change in the directions of momentum equations and in the variables.

First step is the multiplication both sides of Eq. (2.35) with α and Eq. (2.37) with β. Adding them up and making necessary rearrangements, one can reach a new momentum equation in the direction parallel to $\vec{k}$ (Figure 2.1). Second attempt is vice versa, multiplication of both sides of Eq. (2.35) with β and Eq. (2.37) with α. Subtraction of the first from the second ends up with a new momentum equation in the direction normal to $\vec{k}$. The new set of equations is, then:

momentum equation parallel to the wave number vector, $\vec{k}$:

$$\rho\left[i(\alpha U+\beta W-\omega)(\alpha\bar{u}+\beta\bar{w})+(\alpha U'+\beta W')\bar{v}\right]=$$
$$-\frac{i\bar{p}}{\gamma M^2}(\alpha^2+\beta^2)+\frac{\mu}{R}\left[(\alpha\bar{u}+\beta\bar{w})''+(\alpha^2+\beta^2)(i\bar{v}'-2(\alpha\bar{u}+\beta\bar{w}))\right]$$
$$-\frac{2}{3}\frac{\mu}{R}\left[(\alpha^2+\beta^2)(i\bar{v}'-(\alpha\bar{u}+\beta\bar{w}))\right]$$
$$+\frac{1}{R}\left[(\alpha U'+\beta W')\left(\frac{d\mu}{dT}\bar{T}'+\frac{d^2\mu}{dT^2}T'\bar{T}\right)+\frac{d\mu}{dT}\bar{T}(\alpha U''+\beta W'')\right]$$
$$+\frac{1}{R}\frac{d\mu}{dT}T'\left[i\bar{v}(\alpha^2+\beta^2)+(\alpha\bar{u}+\beta\bar{w})'\right], \qquad (2.42)$$

y-momentum equation:

$$i\rho\left[\alpha U+\beta W-\omega\right]\bar{v}=$$
$$-\frac{\bar{p}'}{\gamma M^2}+\frac{\mu}{R}\left[2\bar{v}''+i(\alpha\bar{u}+\beta\bar{w})'-(\alpha^2+\beta^2)\bar{v}-\frac{2}{3}\left(\bar{v}''+i(\alpha\bar{u}+\beta\bar{w})'\right)\right]$$
$$+\frac{1}{R}\frac{d\mu}{dT}\left[2T'\bar{v}'+i(\alpha U'+\beta W')\bar{T}-\frac{2}{3}T'\left(\bar{v}'+i(\alpha\bar{u}+\beta\bar{w})\right)\right], \qquad (2.43)$$

momentum equation normal to the wave number vector, $\vec{k}$:

$$\rho\left[i(\alpha U+\beta W-\omega)(\alpha\bar{w}-\beta\bar{u})+(\alpha W'-\beta U')\bar{v}\right]=$$

$$\frac{\mu}{R}\left[\left(\alpha^2+\beta^2\right)(\beta\bar{u}-\alpha\bar{w})+(\alpha\bar{w}-\beta\bar{u})''\right]+\frac{1}{R}\frac{d\mu}{dT}(\alpha\bar{w}-\beta\bar{u})'T'$$

$$+\frac{1}{R}\left[(\alpha W'-\beta U')\left(\frac{d\mu}{dT}\bar{T}'+\frac{d^2\mu}{dT^2}T'\bar{T}\right)+\frac{d\mu}{dT}\bar{T}(\alpha W''-\beta U'')\right], \qquad (2.44)$$

energy equation:

$$\rho\left[i(\alpha U+\beta W-\omega)\bar{T}+T'\bar{v}\right]=$$

$$-(\gamma-1)\left[i(\alpha\bar{u}+\beta\bar{w})+\bar{v}'\right]+\frac{\gamma\mu}{Pr\,R}\left[\bar{T}''+\frac{2}{\kappa}\frac{d\kappa}{dT}T'\bar{T}'-\left(\alpha^2+\beta^2\right)\bar{T}\right]$$

$$+\frac{\gamma\mu}{Pr\,R}\frac{1}{\kappa}\left[\frac{d\kappa}{dT}T''+\frac{d^2\kappa}{dT^2}(T')^2\right]\bar{T}+\frac{\gamma(\gamma-1)M^2}{R}2\mu i(\alpha U'+\beta W')\bar{v}$$

$$+\frac{\gamma(\gamma-1)M^2}{R}\left[\frac{d\mu}{dT}\bar{T}\left(U'^2+W'^2\right)+\frac{2\mu}{\left(\alpha^2+\beta^2\right)}(\alpha U'+\beta W')(\alpha\bar{u}+\beta\bar{w})'\right]$$

$$+\frac{\gamma(\gamma-1)M^2}{R}\frac{2\mu}{\left(\alpha^2+\beta^2\right)}(\alpha W'-\beta U')(\alpha\bar{w}-\beta\bar{u})', \qquad (2.45)$$

continuity equation:

$$i\left[\alpha U+\beta W-\omega\right]\bar{\rho}+\rho\left[\bar{v}'+i(\alpha\bar{u}+\beta\bar{w})\right]+\rho'\bar{v}=0, \qquad (2.46)$$

equation of state:

$$\bar{p}=\frac{\bar{\rho}}{\rho}+\frac{\bar{T}}{T}. \qquad (2.47)$$

This procedure leads us to a new eighth order system having the variables of $(\alpha\bar{u}+\beta\bar{w})$, $(\alpha\bar{w}-\beta\bar{u})$, $\bar{v}$, $\bar{p}$, $\bar{\rho}$, $\bar{T}$, $\bar{u}'$ and $\bar{w}'$. They are the *basic equations of compressible stability theory* valid for three-dimensional disturbances in a three-dimensional basic flow. However, as mentioned in previous sections, only *2D basic flow case* will be analyzed throughout this thesis. In this respect, the spanwise component of the mean velocity, W together with its first and second derivatives with respect to y distance, W' and W'' are introduced as *zero* while performing the numerical solutions.

Comparing Eqs. (2.42)-(2.47) with Mack's system of linearized equations obtained by following the same procedure, i.e. Eqs. (8.9) in [11], a few small differences are observed. One of them is recognized in y-momentum equation such that the parameter $-2\mu i/3R\left(\alpha\bar{u}'+\beta\bar{w}'\right)$ in Eq. (2.43) appears as $-2\mu i/3R\left(\alpha\bar{u}+\beta\bar{w}\right)$ in Eq. (8.9b) of [11]. One difference observed in continuity equation is that the parameter $\rho'\bar{v}$ in Eq. (2.46) appears as $p'\bar{v}$ in Eq. (8.9d) of the same reference. The last discrepancy is in energy equation, one of the parameters is probably forgotten to be multiplied by 2.

In fact, the mathematical modeling of the compressible stability problem explained in this chapter was derived independently by two people, Atalayer and Özgen at different times and locations and both studies met the same results even up to the last digits. For this reason, there is a high level of confidence in Eqs. (2.42)-(2.47). The minor disagreements with Mack's resultant system of equations are most probably due to printing errors in [11].

2.2.4 First Order Equations

Eqs. (2.42)-(2.47) need to be reorganized in the form of first order differential equations in order to proceed with a convenient numerical solution. In this respect, the variables are redefined in the following manner:

$$\begin{aligned} Z_1 &= \alpha\bar{u} + \beta\bar{w}, & Z_2 &= DZ_1, \\ Z_3 &= \bar{v}, & Z_4 &= \bar{p}/\gamma M^2, \\ Z_5 &= \bar{T}, & Z_6 &= DZ_5, \\ Z_7 &= \alpha\bar{w} - \beta\bar{u}, & Z_8 &= DZ_7. \end{aligned} \tag{2.48}$$

After this point, the differentiation with respect to y is denoted by 'D' instead of prime ('), i.e. $D = d/dy$. With the use of these variables the new system is rewritten as:

$$DZ_i = \sum_{j=1}^{8} a_{ij} Z_j, \qquad i = 1,8, \tag{2.49}$$

where, a_{ij} are the elements of the coefficient matrix (see Appendix A). The corresponding boundary conditions are:

$$\begin{aligned} &\text{No slip BC} \rightarrow Z_1(0) = Z_3(0) = Z_5(0) = Z_7(0) = 0, \\ &\text{Freesream BC} \rightarrow Z_1(y), Z_3(y), Z_5(y), Z_7(y) \rightarrow 0 \text{ as } y \rightarrow \infty. \end{aligned} \tag{2.50}$$

Resulting system of homogeneous equations, together with the homogeneous boundary conditions constitute an eigenvalue problem with the eigenvalues, $(\alpha, \beta, \omega, R)$ and the eigenfunctions, $(\bar{u}, \bar{v}, \bar{w}, \bar{p}, \bar{T})$.

2.2.5 Spatial and Temporal Theories

2.2.5.1 Spatial Amplification Formulation

The spatial amplification theory was first developed by Gaster [22, 23]. Due to this theory, the wave amplitudes change with the distance. Accordingly, the wave number components α and β are *complex* such that:

$$\alpha = \alpha_r + i\alpha_i, \qquad \beta = \beta_r + i\beta_i, \tag{2.51}$$

whereas, the frequency ω is *real,* defining now the circular frequency. In this respect, Eq. (2.33) becomes:

$$\hat{\varphi}(x, y, z, t) = \bar{\varphi}(y) e^{-(\alpha_i x + \beta_i z)} e^{i(\alpha_r x + \beta_r z - \omega t)}. \tag{2.52}$$

The above equation clearly implies that the amplification factor of the corresponding wave is a vector composed of $-\alpha_i$ and $-\beta_i$ where $-\alpha_i$ defines the amplification factor in x direction and $-\beta_i$ in z direction. Its magnitude and angle with respect to x direction are expressed as:

$$\left|\vec{A}\right| = \sqrt{\alpha_i^{\,2} + \beta_i^{\,2}}, \qquad \bar{\psi} = \tan^{-1}\left(\frac{\beta_i}{\alpha_i}\right). \tag{2.53}$$

For the special boundary layers such as *z-independent* 2D planar boundary layers, the amplification factor in z direction is neglected [11]. That is, the change in the amplitude of the spatial wave in x direction becomes the

only criteria in analyzing the amplification factor. Then, for $-\alpha_i$ being the growth rate, if:

$$\begin{aligned} -\alpha_i &< 0 \rightarrow \text{the wave is stable,} \\ -\alpha_i &= 0 \rightarrow \text{the wave is neutrally stable,} \\ -\alpha_i &> 0 \rightarrow \text{the wave is unstable.} \end{aligned} \tag{2.54}$$

The real parts of these wave number components, (α_r, β_r) define the wave number vector, $\vec{k}$ with a magnitude, k and angle, ψ as:

$$k = \sqrt{\alpha_r^{\,2} + \beta_r^{\,2}}, \qquad \psi = \tan^{-1}\left(\frac{\beta_r}{\alpha_r}\right). \tag{2.55}$$

Thus, the wave speed, c with which the constant phase lines move in a distance normal to themselves, becomes a real parameter defined by:

$$c = \omega / k. \tag{2.56}$$

The dispersion relation, i.e. the relation for eigenvalues is written as:

$$\omega = (\alpha, \beta). \tag{2.57}$$

The determination of this relation for a given Reynolds number and boundary layer profile is then the goal of the stability analysis.

2.2.5.2 Temporal Amplification Formulation

In this case, the wave amplitudes change with time. Accordingly, the frequency ω is *complex* so that:

$$\omega = \omega_r + i\omega_i, \tag{2.58}$$

and the wave number components, α, β are *real*. The wave speed, c is now a complex parameter in the form of:

$$c = \omega / k = c_r + ic_i, \tag{2.59}$$

where, c_r is the *phase speed* and c_i is the *temporal amplification factor*. The magnitude of the wave number vector, k and its angle with respect to the streamwise direction is defined as:

$$k = \sqrt{\alpha^2 + \beta^2}, \qquad \psi = \tan^{-1}\left(\frac{\beta}{\alpha}\right). \tag{2.60}$$

In temporal case, the definition of local normal modes becomes:

$$\hat{\varphi}(x, y, z, t) = \overline{\varphi}(y) e^{\omega_i t} e^{i(\alpha x + \beta z - \omega_r t)}, \tag{2.61}$$

where, $\omega_r = kc_r$ represents the circular frequency. The *growth rate* of the corresponding wave is whereas:

$$\omega_i = kc_i. \tag{2.62}$$

The sign of k is always positive meaning that, it does not change the configuration range of the amplification. In this respect, the limits of stability are reformed according to the temporal amplification factor, i.e. if:

$$\begin{aligned} &c_i < 0 \rightarrow \text{the wave is stable,} \\ &c_i = 0 \rightarrow \text{the wave is neutrally stable,} \\ &c_i > 0 \rightarrow \text{the wave is unstable.} \end{aligned} \tag{2.63}$$

In this case, the dispersion relation is written as:

$$c = (\alpha, \beta). \tag{2.64}$$

According to Gaster's studies [22, 23], the spatial formulation seems to give the changes in the amplitude of a normal mode more directly than the temporal theory does. However, this has not been proved mathematically in a complete manner [24]. Also, compared to the temporal theory, the spatial formulation is much more difficult to solve mathematically since it leads to nonlinearity. That's why, in this *thesis*, the stability analysis is restricted to the *temporal amplification theory*.

However, considering a steady mean flow as in this case, the amplitude of a normal mode changes only with distance. So, while dealing with the disturbance amplitudes it would be necessary to express the results of the temporal formulation in terms of the spatial formulation. This transformation is performed through the *Gaster's formulation* that will be explained in the next chapters.

With the use of temporal theory, the set of eigenvalues is rearranged as (α,β,c_r,c_i,R) . The resultant system of Eqs. (2.49) is then solved for the certain combinations of these eigenvalues satisfying the boundary conditions in Eq. (2.50).

CHAPTER 3

SOLUTION METHOD

3.1 Introduction

The mathematical modeling of the stability problem for a compressible boundary concludes with the governing equations defined in Eqs. (2.49) and the boundary conditions in Eq. (2.50). The homogeneous equation system together with the homogeneous boundary conditions constitutes an eigenvalue problem. For the numerical integration of this first order differential system, one of the most commonly used techniques, *shooting technique* is applied in this study. Unlike other equally used solution techniques such as finite difference or spectral methods, it does not need any rearrangement when applied to different flow case problems. Besides, reaching the solution with this method takes much shorter time compared to others. This is why many computer codes for boundary layer problems in literature are based on this technique such as the ones developed by Mack [11] or by Brown [25].

This chapter concentrates on the numerical solution of the stability problem, i.e. the solution of Eqs. (2.49). The shooting method that it is based on, and determination of the initial values needed for the numerical

integration will be covered in the first section. One problem about this technique could be the loss of linear independence between the obtained solutions. The next section will be concerned with the *Gram-Schmidt Orthonormalization Technique* which is a way of preventing this problem. The use of *Newton-Raphson Iteration* in plotting the proper configurations of the stability characteristics and the *Simplex Method* applied as the first step of this process will be the topics of the last section.

3.2 Integration Procedure

The linear viscous stability theory results in an eigenvalue problem of which an integration procedure is highly needed for the solution. In this study, a backward integration method also mentioned by Drazin and Reid [24], namely *the shooting method*, is chosen. However, the obtained governing Eqs. (2.49) together with Eq. (2.50) are not yet ready to be solved. First, one has to specify the velocity profile, the temperature profile and their derivatives in the system. As the present stability analysis will be performed for 2D mean flows, the current study accounts for 2D boundary layers.

The complexity of compressibility is felt here, one more time. Different from the simplest incompressible boundary layer over adiabatic flat plates, the energy equation has to be included within the derivations of boundary layer equations. In addition, the variable property effects enter the problem through the density, the coefficients of viscosity and thermal conductivity together with their derivatives as these are functions of mean flow temperature.

In order to obtain the streamwise velocity profiles, the modified Falkner-Skan equation is to be used (see App. B for the derivation):

$$2\left[\mu\left(\frac{f'_{FS}}{\rho}\right)'\right]' + f_{FS}\left[\frac{f'_{FS}}{\rho}\right]' = 0, \tag{3.1}$$

where, (′) denotes the differentiation with respect to dimensionless y distance (y^*/L^*, L^* being the Blasius length scale) and μ represents the dynamic viscosity coefficient nondimensionalized by μ_e^*. Here, ρ is the dimensionless density (ρ^*/ρ_e^*) and f_{FS} is the dimensionless stream function defined as:

$$f_{FS} = \Psi^*/\sqrt{\nu_e^* U_e^* x^*}, \tag{3.2}$$

Ψ^* being the dimensional stream function and ν_e^* being the freestream kinematic viscosity. The relation between this dimensionless stream function f_{FS} and the dimensionless streamwise velocity component U, (U^*/U_e^*), is obtained as follows (see App. B for the derivation):

$$f'_{FS} = U.\rho\,. \tag{3.3}$$

In this respect, Eq. (3.1) can be rewritten as:

$$2\left[\mu U'\right]' + f_{FS}U' = 0\,. \tag{3.4}$$

This equation is mainly derived from the x-momentum equation of the compressible boundary layer equations for 2D flow over a flat plate with zero pressure gradient.

For the temperature field whereas, the energy equation is handled within the same flow conditions (see App. B for the derivation). The resulting equation that gives the temperature profile is, then:

$$2\left[\frac{\mu}{\mathrm{Pr}}g'\right]' + f_{FS}g' = -2(\gamma-1)M^2\mu(U')^2, \tag{3.5}$$

where, g is dimensionless temperature (T^*/T_e^*) and M is the local Mach number at the edge of the boundary layer. For flat plate cases, it refers to the freestream Mach number. As mentioned earlier, the Prandtl number and the specific heat ratio are held constant throughout this analysis. For air at standard conditions, $\mathrm{Pr} = 0.72$ and $\gamma = 1.4$.

The reference length used to make the related parameters dimensionless is the Falkner-Skan length scale for zero pressure gradient case, i.e., the Blasius length scale $(L^* = \sqrt{\nu_e^* x^* / U_e^*})$. For convenience, it has been used also in nondimensionalizing Eqs. (2.17)-(2.22).

Making necessary rearrangements, one can reach the following system of mean flow equations for a compressible boundary layer over an adiabatic flat plate:

$$U'' = -\left(\frac{f_{FS}}{2\mu} + \frac{\mu'}{\mu}\right)U', \tag{3.6}$$

$$g'' = -\left(\frac{Pr}{2\mu} f_{FS} + \frac{\mu'}{\mu}\right)g' - Pr(\gamma - 1)M^2 (U')^2, \tag{3.7}$$

with the following boundary conditions:

No slip BC $\rightarrow f_{FS}(0) = f'_{FS}(0) = 0$ and $g'(0) = 0$ (for adiabatic wall case),

or, $g(0) = g_w$ (for constant temp. case),

Freestream BC $\rightarrow f'_{FS} \rightarrow 1$, $g \rightarrow 1$ as $y \rightarrow \infty$. (3.8)

Here, g_w refers to nondimensional wall temperature, T_w^* / T_e^*. Recall that, because the local mean pressure equals to the freestream mean pressure, the nondimensional perfect gas relation reduces to $\rho T = 1$ or, $\rho = 1/g$. The remaining terms, viscosity and its derivative with respect to dimensionless y distance are described by using *Sutherland's formula* [4]:

$$\frac{\mu^*}{\mu_e^*} = \left(\frac{T^*}{T_e^*}\right)^{3/2} \frac{T_e^* + S_1^*}{T^* + S_1^*}, \tag{3.9}$$

or, in nondimensional form:

$$\mu = g^{3/2} \frac{1 + S_1}{g + S_1}, \tag{3.10}$$

where, $S_1 = S_1^* / T_e^*$ and $S_1^* = 110K$ for air [4]. Accordingly, its derivative with respect to dimensionless y distance is obtained as:

$$\mu' = \frac{g'}{g + S_1}\left[\frac{3}{2} g^{1/2}\left(1 + S_1\right) - \mu\right]. \qquad (3.11)$$

For the solution of the coupled ordinary differential system expressed by Eqs. (3.6)-(3.7), the same integration technique, *shooting technique*, is employed. Accordingly, integration proceeds from the freestream to the wall. Actually, a point in the boundary layer sufficiently far from the wall, say y_e, where the dimensionless mean velocity and temperature are sufficiently close to one, would provide the location to start the integration. In this respect, the true values of f_{FS}, U, U', g and g' at that point would be the ones that the integrator uses as initial values. The well-known variable step-size fourth-order Runge-Kutta method has been chosen as the integrator [26].

The determination of the starting values, i.e. values at $y = y_e$ for the integration procedure is performed by an independent computer code. This is actually based on a solver consisting of a modified shooting method for the incompressible boundary layer flow cases which was developed by Nachtsheim and Swigert [27]. Here, it has been also modified according to the compressible flow case using Eqs. (3.6)-(3.7) so that it would give proper initial values of f_{FS}, U, U', g and g' for the integration of mean flow at a specified freestream Mach number value.

The reliability of the modified code can be checked in two ways. First, the adiabatic wall temperature values found by this solver for a number of specified Mach numbers are compared with the theoretical values calculated with the following relation [4]:

$$T_w^* = T_e^* \left(1 + \sqrt{Pr}\,\frac{\gamma - 1}{2} M^2 \right). \tag{3.12}$$

Here, T_e^* represents the freestream temperature in Kelvin and M represents the freestream Mach number. In this case, both correspond to the values at the edge of the boundary layer. Table 3.1 gives the results obtained for some freestream Mach number values using this relation. It can easily be deduced that these values match with the results found by the code with a high accuracy.

Table 3.1 Comparison of the obtained wall temperatures with the theoretical values at specified Mach numbers.

Mach no.	$(g_w)_{code}$	$(g_w)_{theoretical}$	% dif.
0.0	0.999999999997	1.000000000000	0.0
0.2	1.006781343790	1.006788225099	0.0
0.4	1.027123067820	1.027152900398	0.0
0.6	1.061017278000	1.061094025895	0.0
0.8	1.108451373770	1.108611601590	0.0
0.9	1.137240628870	1.137461558263	0.0
1.0	1.169408009800	1.169705627485	0.0
1.5	1.380813398430	1.381837661841	0.0
2.0	1.676185800170	1.678822509939	0.0
2.5	2.055082262840	2.060660171780	0.0
3.0	2.517093397070	2.527350647363	0.0
3.5	3.061884499320	3.078893936688	0.1
4.0	3.689198709390	3.715290039756	0.2
4.5	4.398848207560	4.436538956567	0.3
5.0	5.190698956920	5.242640687119	0.4
6.0	7.020658293000	7.109402589452	0.8
7.0	9.178629388370	9.315575746754	1.7

The second attempt for this purpose would be the direct comparison of obtained the velocity and the temperature profiles with the corresponding ones found by van Driest [4, 28] for a laminar, compressible boundary layer over an insulated flat plate. Looking at Figure 3.1 and Figure 3.2, one can clearly see the remarkable agreement of the solutions obtained in this study with the van Driest's.

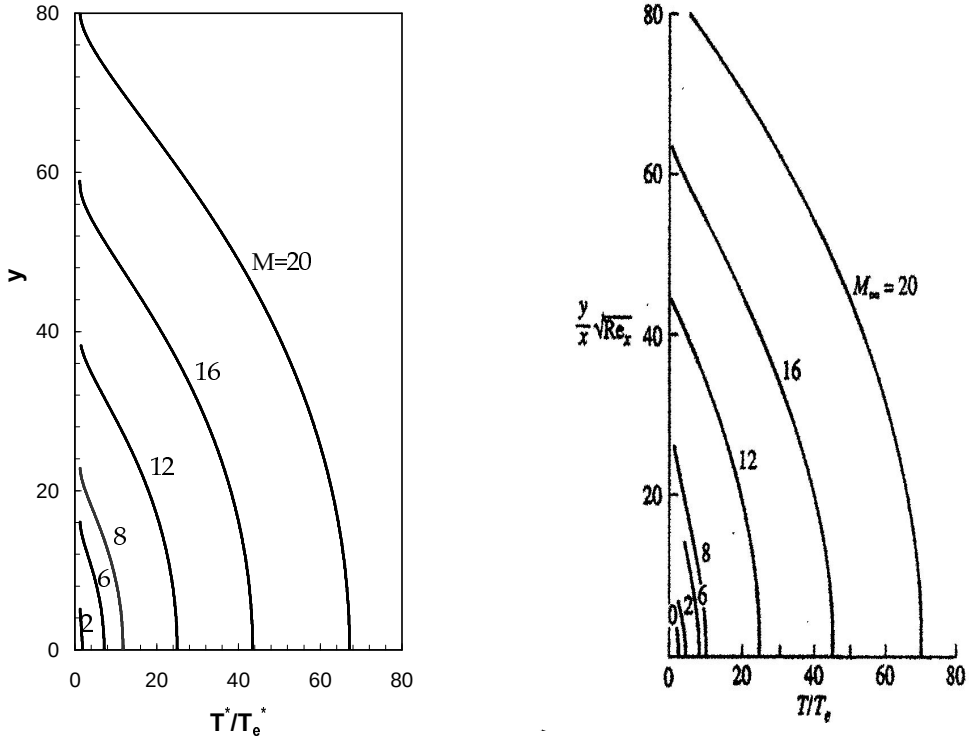

Figure 3.1 Comparison of **(a)** the temperature profiles obtained in current study, with **(b)** the results of van Driest [4, 28].

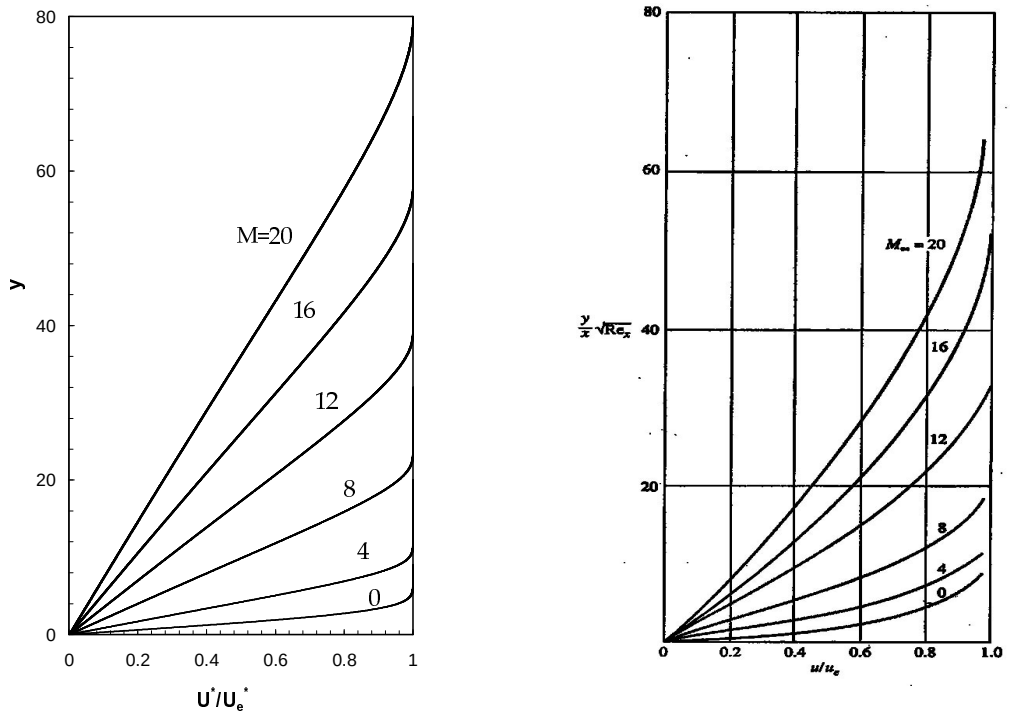

Figure 3.2 Comparison of **(a)** the velocity profiles obtained in current study, with **(b)** the results of van Driest [4, 28].

All these comparisons conclude that the efforts taken through this topic are well accomplished. Table 3.2 and Table 3.3 give then the lists of results determined as the starting values for the mean flow solutions, i.e., the lists of f_{FS}, U, U′, g and g′ values at chosen Mach numbers. These are also the inputs for integration of the perturbation system (Eqs. (2.49)). The number of digits after the decimal may seem too many, but for the solution of the eigenvalue problem this turned out to be a necessity since the mean flow solutions are very susceptible to the starting values used for the integration.

Table 3.2 Starting values of velocity field for mean flow integration.

Mach no.	y_e	f_{FS}	U	U'
0.0	9.00	7.27921323	9.99999996E-1	4.12787201E-7
0.2	9.00	7.26272374	9.99999996E-1	4.37676219E-7
0.4	9.98	8.19338362	1.00000000E+0	1.19554860E-8
0.6	9.98	8.11158620	1.00000000E+0	1.65711019E-8
0.8	9.99	8.00795865	1.00000000E+0	2.49181700E-8
0.9	9.99	7.93946344	1.00000000E+0	3.25522628E-8
1.0	10.00	7.87333961	1.00000000E+0	4.20041322E-8
1.5	10.73	8.11312421	1.00000000E+0	1.54533634E-8
2.0	10.63	7.35426198	9.99999999E-1	2.75063253E-7
2.5	11.47	7.38619734	9.99999999E-1	2.28890516E-7
3.0	12.48	7.45678936	9.99999999E-1	1.63567417E-7
3.5	13.76	7.68113290	9.99999999E-1	6.46284245E-8
4.0	15.26	8.02150352	9.99999999E-1	1.56347415E-8
4.5	16.60	8.10772464	9.99999990E-1	1.01449499E-8
5.0	17.92	8.08766366	9.99999982E-1	1.01010288E-8
6.0	20.79	8.04296698	9.99999972E-1	1.02031646E-8
7.0	23.95	8.00597458	9.99999969E-1	1.00264894E-8

Table 3.3 Starting values of temperature field for mean flow integration.

Mach no.	y_e	g	g'
0.0	9.00	1.00000000	0.00000000E+0
0.2	9.00	1.00000000	-2.04879145E-7
0.4	9.98	1.00000000	-6.13200824E-8
0.6	9.98	1.00000000	-1.74414265E-7
0.8	9.99	1.00000001	-4.15544403E-7
0.9	9.99	1.00000001	-6.37158529E-7
1.0	10.00	1.00000001	-9.44507537E-7
1.5	10.73	1.00000019	-1.03035488E-6
2.0	10.63	1.00000450	-1.44834604E-5
2.5	11.47	1.00000657	-1.97023556E-5
3.0	12.48	1.00000725	-2.21208296E-5
3.5	13.76	1.00000481	-1.53162071E-5
4.0	15.26	1.00000185	-7.14661330E-6
4.5	16.60	1.00000162	-6.57448657E-6
5.0	17.92	1.00000209	-8.03053769E-6
6.0	20.79	1.00000328	-1.14783497E-5
7.0	23.95	1.00000462	-1.52147783E-5

3.2.1 Uniform Mean Flow

One last step before to start solving the differential system for the perturbations is the determination of the starting values for the integration of the stability equations. The choice of a backward integration method as a solution method was mentioned earlier. It was also clarified that the starting point for the integration would be the freestream or, a distance sufficiently far from the wall satisfying the recommended conditions. Therefore, one has to find the starting values of the integral which are actually the analytical solutions of the perturbation system at that location. How they are obtained is outlined below.

In the freestream (or, at $y = y_e$) the flow is uniform, i.e., $U = U_e$, $W = W_e$ and $T = 1$, $\mu = 1$, $\kappa = 1$. Besides, all y derivatives of mean flow quantities are zero. Applying these conditions to Eqs. (2.49), one obtains a system of first order differential equations with constant coefficients (see App. C). The first six of these equations are coupled so that they can be solved as an independent system. This facilitates the solution procedure more than expected. Appendix C gives detailed information about the analytical solutions of the whole system concluding with the following form:

$$Z_i(y) = \vec{\varphi}_i e^{\lambda_i y}, \qquad i = 1,8, \tag{3.13}$$

where, Z_i is the eight component solution vector, $\vec{\varphi}_i$ are the eight component *characteristic vectors*, and λ_i are the eight component *characteristic values*. These characteristic values are found as follows:

$$\lambda_{1,2} = \pm\sqrt{b_{11}},$$

$$\lambda_{3,4} = \pm\sqrt{\frac{(b_{22}+b_{33})}{2} + \frac{1}{2}\sqrt{(b_{33}-b_{22})^2 + 4b_{23}b_{32}}},$$

$$\lambda_{5,6} = \pm\sqrt{\frac{(b_{22}+b_{33})}{2} - \frac{1}{2}\sqrt{(b_{33}-b_{22})^2 + 4b_{23}b_{32}}},$$

$$\lambda_{7,8} = \lambda_{1,2}, \tag{3.14}$$

with,

$$b_{11} = \left(\alpha^2+\beta^2\right) + iR\left(\alpha U_e + \beta W_e - \omega\right),$$

$$b_{12} = \left(\alpha^2+\beta^2\right)\left[iR - \frac{1}{3}\gamma M^2\left(\alpha U_e + \beta W_e - \omega\right)\right],$$

$$b_{13} = \frac{1}{3}\left(\alpha^2+\beta^2\right)\left(\alpha U_e + \beta W_e - \omega\right),$$

$$b_{22} = \left(\alpha^2+\beta^2\right) - \frac{R}{E_e}\left[\gamma - \frac{4}{3}\Pr(\gamma-1)\right]M^2\left(\alpha U_e + \beta W_e - \omega\right)^2,$$

$$b_{23} = \frac{R}{E_e}\left[1 - \frac{4}{3}\Pr\right]\left(\alpha U_e + \beta W_e - \omega\right)^2,$$

$$b_{32} = -iR\Pr(\gamma-1)M^2\left(\alpha U_e + \beta W_e - \omega\right),$$

$$b_{33} = \left(\alpha^2+\beta^2\right) + iR\Pr\left(\alpha U_e + \beta W_e - \omega\right), \tag{3.15}$$

where, $E_e = \left[R + i4/3\gamma M^2\left(\alpha U_e + \beta W_e - \omega\right)\right]$. The first six of the characteristic values, $\lambda_{1,2}$, $\lambda_{3,4}$ and $\lambda_{5,6}$ are obtained by solving the first six coupled differential equations as an independent system in the form of three second order equations with constant coefficients 'b_{ij}' given in Eqs. (3.15). The last two characteristic values, $\lambda_{7,8}$ are whereas found by using the remaining two differential equations that form a second-order system decoupled from the

first six equations. Bear in mind that these characteristic values should not be confused with the eigenvalues (α,β,c_r,c_i,R) of the system expressed in Eqs. (2.49).

The freestream boundary condition defined in Eq. (2.50) requires decaying solutions as going far away from the wall. In order this to be valid, only the characteristic values with a *negative sign* are taken into account. For each negative characteristic value, there exists a distinct eight component characteristic vector, $\vec{\varphi}_i$. These vectors together with the characteristic values constitute the eight component solution vector, Z_i.

Referring to Appendix C for the characteristic vectors corresponding to the first three negative characteristic values λ_1, λ_3, λ_5 of the first six coupled differential equations:

$$\vec{\xi} = \begin{bmatrix} \xi_{11} & \xi_{31} & \xi_{51} \\ \xi_{12} & \xi_{32} & \xi_{52} \\ \xi_{13} & \xi_{33} & \xi_{53} \end{bmatrix},$$

$$= \begin{bmatrix} 1 & \dfrac{b_{12}(b_{33}-\lambda_3^2)-b_{13}b_{32}}{(\lambda_3^2-b_{11})} & \dfrac{b_{12}(b_{33}-\lambda_5^2)-b_{13}b_{32}}{(\lambda_5^2-b_{11})} \\ 0 & (b_{33}-\lambda_3^2) & (b_{33}-\lambda_5^2) \\ 0 & -b_{32} & -b_{32} \end{bmatrix}, \tag{3.16}$$

and calling $B_e = (\alpha U_e + \beta W_e - \omega)$, the expanded form of Z_i would be expressed as follows:

$$\begin{bmatrix} Z_1 \\ Z_2 \\ Z_3 \\ Z_4 \\ Z_5 \\ Z_6 \\ Z_7 \\ Z_8 \end{bmatrix} = c_1 \begin{bmatrix} \xi_{11} \\ \xi_{11}\lambda_1 \\ -i\left(\dfrac{\xi_{11} + B_e\left(\gamma M^2 \xi_{12} - \xi_{13}\right)}{\lambda_1}\right) \\ \xi_{12} \\ \xi_{13} \\ \xi_{13}\lambda_1 \\ 0 \\ 0 \end{bmatrix} e^{\lambda_1 y} + c_3 \begin{bmatrix} \xi_{31} \\ \xi_{31}\lambda_3 \\ -i\left(\dfrac{\xi_{31} + B_e\left(\gamma M^2 \xi_{32} - \xi_{33}\right)}{\lambda_3}\right) \\ \xi_{32} \\ \xi_{33} \\ \xi_{33}\lambda_3 \\ 0 \\ 0 \end{bmatrix} e^{\lambda_3 y} + c_5 \begin{bmatrix} \xi_{51} \\ \xi_{51}\lambda_5 \\ -i\left(\dfrac{\xi_{51} + B_e\left(\gamma M^2 \xi_{52} - \xi_{53}\right)}{\lambda_5}\right) \\ \xi_{52} \\ \xi_{53} \\ \xi_{53}\lambda_5 \\ 0 \\ 0 \end{bmatrix} e^{\lambda_5 y} + c_7 \begin{bmatrix} 0 \\ 0 \\ 0 \\ 0 \\ 0 \\ 0 \\ 1 \\ \lambda_7 \end{bmatrix} e^{\lambda_7 y} \qquad (3.17)$$

3.2.2 Shooting Technique

The solution vector in Eq. (3.17) provides the starting values for the numerical integration of Eqs. (2.49). The shooting technique that has been chosen as the solution method in this study, basically comprises the simultaneous integration of Eqs. (2.49) with Eqs. (3.6)-(3.7) by using a common integrator. With the use of a fourth-order variable step-size Runge-Kutta method [26], integration proceeds from $y = y_e$ towards the wall. The starting values for basic (mean) flow system that are listed in Table 3.2 and Table 3.3, are treated as the inputs of this simultaneous process. The uniform mean flow solutions of the perturbation equations whereas, define the initial values of the integral. Considering the zero elements of these solutions, Eq. (3.17) can be rewritten in the following generalized form:

$$
\begin{aligned}
Z_1 &= c_1\varphi_{11}e^{\lambda_1 y} + c_3\varphi_{31}e^{\lambda_3 y} + c_5\varphi_{51}e^{\lambda_5 y},\\
Z_2 &= c_1\varphi_{12}e^{\lambda_1 y} + c_3\varphi_{32}e^{\lambda_3 y} + c_5\varphi_{52}e^{\lambda_5 y},\\
Z_3 &= c_1\varphi_{13}e^{\lambda_1 y} + c_3\varphi_{33}e^{\lambda_3 y} + c_5\varphi_{53}e^{\lambda_5 y},\\
Z_4 &= c_1\varphi_{14}e^{\lambda_1 y} + c_3\varphi_{34}e^{\lambda_3 y} + c_5\varphi_{54}e^{\lambda_5 y},\\
Z_5 &= c_1\varphi_{15}e^{\lambda_1 y} + c_3\varphi_{35}e^{\lambda_3 y} + c_5\varphi_{55}e^{\lambda_5 y},\\
Z_6 &= c_1\varphi_{16}e^{\lambda_1 y} + c_3\varphi_{36}e^{\lambda_3 y} + c_5\varphi_{56}e^{\lambda_5 y},\\
Z_7 &= c_7\varphi_{77}e^{\lambda_7 y},\\
Z_8 &= c_7\varphi_{78}e^{\lambda_7 y}.
\end{aligned}
\tag{3.18}
$$

When the wall is reached, it is checked whether the corresponding boundary conditions given in Eq. (2.50) are satisfied. Applying no slip condition, the system reduces to the following matrix form:

$$\begin{bmatrix} \varphi_{11}e^{\lambda_1 y} & \varphi_{31}e^{\lambda_3 y} & \varphi_{51}e^{\lambda_5 y} & 0 \\ \varphi_{13}e^{\lambda_1 y} & \varphi_{33}e^{\lambda_3 y} & \varphi_{53}e^{\lambda_5 y} & 0 \\ \varphi_{15}e^{\lambda_1 y} & \varphi_{35}e^{\lambda_3 y} & \varphi_{55}e^{\lambda_5 y} & 0 \\ 0 & 0 & 0 & \varphi_{77}e^{\lambda_7 y} \end{bmatrix} \begin{bmatrix} c_1 \\ c_3 \\ c_5 \\ c_7 \end{bmatrix} = \begin{bmatrix} 0 \\ 0 \\ 0 \\ 0 \end{bmatrix}. \tag{3.19}$$

It is obvious that the determinant of the first matrix (a complex determinant in this study) must be equal to zero for the existence of nontrivial solutions. In this respect:

$$\begin{aligned} &\mathrm{DET} = 0 \\ &= \varphi_{11}\varphi_{33}\varphi_{55}\varphi_{77} - \varphi_{11}\varphi_{35}\varphi_{53}\varphi_{77} - \varphi_{13}\varphi_{31}\varphi_{53}\varphi_{77} \\ &\quad + \varphi_{13}\varphi_{35}\varphi_{51}\varphi_{77} + \varphi_{15}\varphi_{31}\varphi_{53}\varphi_{77} - \varphi_{15}\varphi_{33}\varphi_{51}\varphi_{77}. \end{aligned} \tag{3.20}$$

Regarding that only the certain combinations of the eigenvalues $(\alpha, \beta, c_r, c_i, R)$ satisfy this condition, the evaluation of these combinations forms an essence of the current solution method.

3.3 Gram Schmidt Orthonormalization

One problem during the numerical integration is that, the growth speeds of the four solutions (each corresponding to a λ_i) in magnitudes, are different from each other. The rapid growing of some solutions (can be one or more) is actually because of their coefficients consisting of Reynolds

number. As the integration proceeds however, this difference starts occurring in orders of magnitude. It can reach such an extent that the round-off error or the parasite error of one solution approaches almost the same order of magnitude of another solution itself. As a result, this causes the linear independence between these solutions to be lost. In order to prevent this, an orthonormalization technique must be used [17, 29].

The *Gram-Schmidt Orthonormalization* is one of these techniques that is commonly used to avoid such problems. Godunov (1961), Bellman and Kalaba (1965) are the scientists who developed this method for linear differential systems. An alternative would be the Kaplan's filtering technique (1964) as also stated by Mack [11]. This method is based on purifying the slower growing solution by using a filtering system on the parasitic error whenever the loss of linear independence occurs. The reason why the Gram-Schmidt has been chosen here is that it is much easier to incorporate to higher order systems compared to Kaplan's method.

Physically, Gram-Schmidt technique prevents the loss of independence by making the solution vectors orthonormal at regular steps during the integration. Remember that in this study, there are four solutions corresponding to λ_1, λ_3, λ_5 and λ_7. The first three of them are obtained by using the first six differential equations of the main system. The last solution vector corresponding to λ_7 is whereas independent from these coupled ones. That's why; the orthogonalization procedure is applied to all except for this uncoupled vector. Introducing the solution vectors as $V_{s,i}$, each of which corresponds to the first three λ_i, and representing their orthogonalized

forms by $W_{orth,i}$ that compose an orthogonal basis, the Gram-Schmidt algorithm is derived in the following steps:

$$\underline{\text{Step 1}} \rightarrow W_{orth,1} = V_{s,1},$$

$$\underline{\text{Step 2}} \rightarrow W_{orth,2} = V_{s,2} - \frac{\langle V_{s,2}, W_{orth,1} \rangle}{\|W_{orth,1}\|^2} W_{orth,1},$$

$$\underline{\text{Step 3}} \rightarrow W_{orth,3} = V_{s,3} - \frac{\langle V_{s,3}, W_{orth,1} \rangle}{\|W_{orth,1}\|^2} W_{orth,1} - \frac{\langle V_{s,3}, W_{orth,2} \rangle}{\|W_{orth,2}\|^2} W_{orth,2}. \quad (3.21)$$

The first step is nothing but taking directly the solution vector $V_{s,1}$ as the first orthogonal vector. The second step is in words, the orthogonal projection of the second solution vector $V_{s,2}$ on the first vector. The last step whereas defines the orthogonal projection of the third solution vector $V_{s,3}$ on the space formed by the first and the second orthogonalized solution vectors. Needless to say, these solution vectors are composed of complex elements. Thereby, the complex inner product is represented by:

$$\langle V_s, W_{orth} \rangle = \sum_{i=1}^{8} v_i w_{i,cc}, \quad (3.22)$$

where, v_i, w_i are elements of the V_s, W_{orth} vectors, respectively, and cc defines the complex conjugate of the corresponding element. On the other hand, the norm is defined as:

$$\|W_{orth}\| = \langle W_{orth}, W_{orth,cc} \rangle^{1/2}. \quad (3.23)$$

The procedure results in a set of orthogonal vectors composed of complex elements. These new vectors together with the remaining independent one for λ_7 are then normalized by their own magnitudes. This is the last step of Gram-Schmidt that ends up with four linearly independent normalized solution vectors forming an orthonormal basis. This procedure is repeated in every step size, Δy. While choosing this step size for the orthonormalization, two criteria have been considered; first, it should be smaller than or equal to 1, and $y_e / \Delta y$ must always be an integer. In this study, it is taken as 0.1 and no problem has been encountered.

The algorithm is known to be complex considering the determination of the eigenfunctions of the stability problem. However, because this thesis concentrates on finding only the eigenvalues rather than the eigenvectors, there is no need to worry about its complexity.

3.4 Newton Iteration

As clarified previously, the aim of this study is to search for the certain combinations of $(\alpha, \beta, c_r, c_i, R)$ satisfying the condition in Eq. (3.20). In the current study, two of these parameters (c_i, R) are fixed and the other two (c_r, α) are searched. The last parameter β whereas, is not an additional parameter as it's a function of α and a specified wave angle, ψ. The resultant combinations can be represented in various ways. The common one is the constant temporal amplification curve. In such cases, c_i is set to a constant value and the variation of wave number α with R is visualized.

Figure 3.3 shows an example to the ones plotted in a manner explained above. These curves, called *stability curves* are one of the main goals of this study. In order to plot these constant temporal amplification curves, one needs two starting points on the curve so that the Newton iteration can proceed in the specified R-direction. Sample points are shown as *point A* and *point B* in Figure 3.3. They are essentially the required values for the iteration to proceed and to find the rest of the curve in the corresponding direction. These points are found by using a function minimization routine based on the *Simplex method* [26].

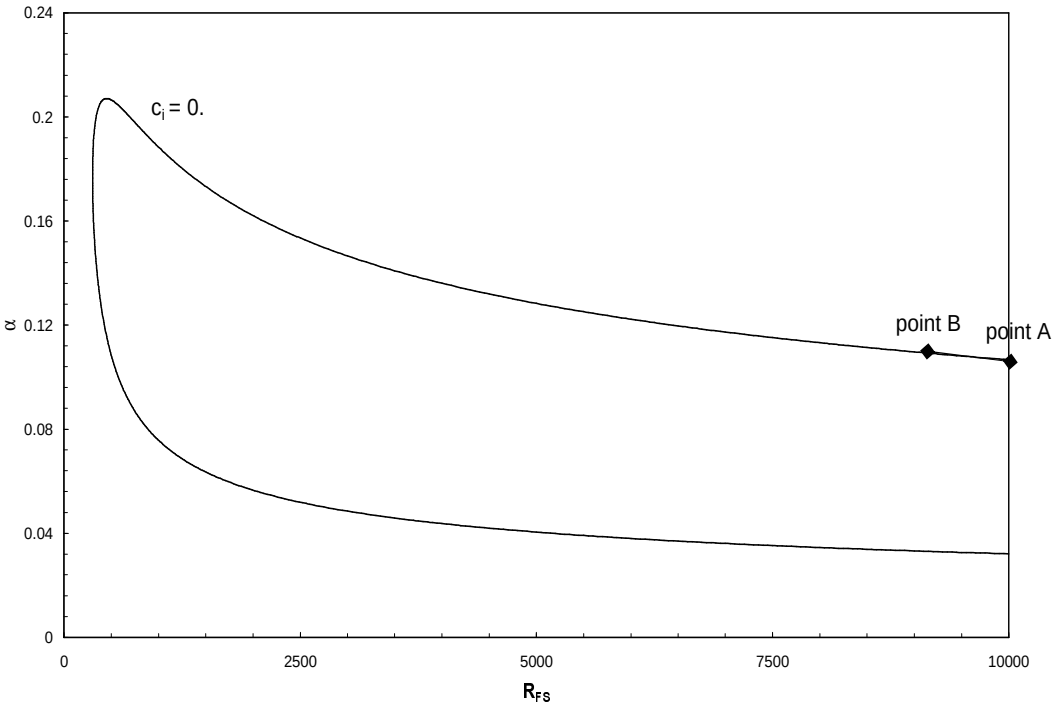

Figure 3.3 Neutral stability curve for 2D flow with two-dimensional disturbances over an adiabatic flat plate at M=0.

The Simplex method, which was invented by George Dantzig in 1947, is known as the basic technique in solutions of the linear optimization programs. Its use for function minimization whereas, was developed by Nelder and Mead [30]. This method is an efficient iterative algorithm to solve unconstrained minimization problems numerically with several variables. Quick convergence and intelligent choice of linearization of the function to be minimized are non-trivial key elements in general minimization algorithms.

Then, what is a *simplex*? A simplex is the geometrical shape consisting of N+1 vertices in N-dimensions, or simply in N number-of-unknowns. In three dimensions, it becomes a tetrahedron, whereas it reduces to a triangle in two dimensions. In this case, setting the number of searched parameters to 2 as c_r and α makes the simplex a triangle as shown in Figure 3.4.

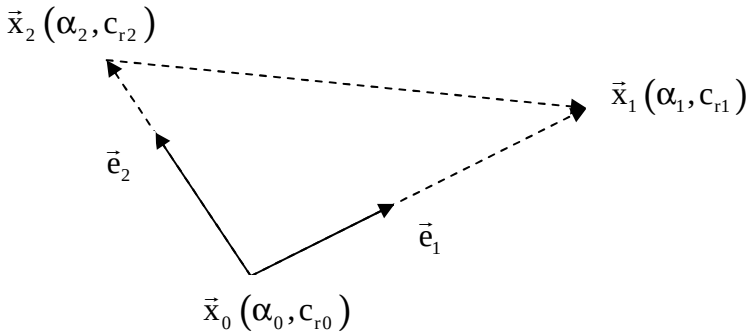

Figure 3.4 A sample simplex with its initial coordinates, $\vec{x}_0$ being the initial guess.

This method similar to the iteration procedure needs also a starting point. However, its accuracy does not so much depend on that point. By defining that point, say $\vec{x}_0$, the other two points, i.e., other vertices of the triangle are found by the following:

$$\vec{x}_i = \vec{x}_0 + \lambda \vec{e}_i \qquad i = 1, 2 . \tag{3.24}$$

Here, each of $\vec{e}_i$ defines a unit vector and λ refers to a constant which is the characteristic length scale of each vector direction. In this study, it is taken as 0.1.

The simplex method is made up of numerous steps most of which are called *reflections*. In such steps, the highest point, i.e. the point having the largest function, is reflected through the opposite face of the simplex to a point having a lower function. The highest point or highest function refers here to the point having the largest determinant, Eq. (3.20). These reflections are however, limited to conserve the volume of the simplex, hence avoid degeneracy.

Other types of steps taken through the application could be namely *expansion*, where the simplex expands in one or another direction to take larger steps; *contraction* along one direction from the highest point, and *multi-contraction*, i.e. contraction in all directions. The last one occurs when simplex tries to pass through a narrow region by pulling itself around its lowest (best) point. In this case, the best point is where the determinant is minimum.

In this study, the Simplex method searches for the values where the determinant 'DET', or 'D' is very close to zero. It starts searching with an initial point and correspondingly an initial triangle similar to Figure 3.4.

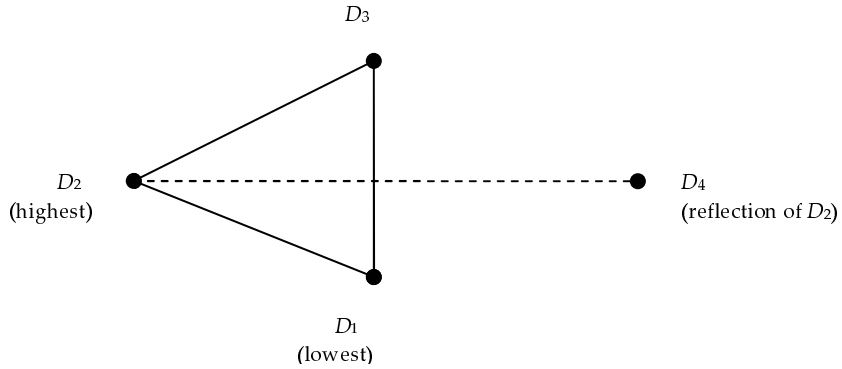

Figure 3.5 Reflection of the highest point across the edge of the simplex.

The points forming the initial simplex are checked for the highest and the lowest determinant. As the point with the highest function is obtained, its mirror image is taken across the edge of the simplex (Figure 3.5).

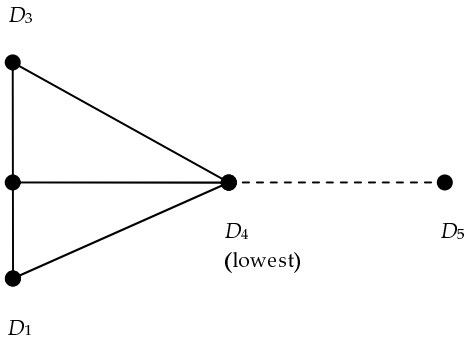

Figure 3.6 First step towards expansion, investigation of a much lower point in the same direction with the current lowest one.

As a result of reflection, the simplex takes the shape of Figure 3.6. The new point, D_4 is then compared with the other two points. If it is the lowest one, this time the mirror image is taken on the same direction with the first, i.e., going further away from the edge, and within a distance twice the first in order to see if the determinant drops further in direction of D_4. The new point D_5 is then checked whether it has a lower or higher determinant than D_4.

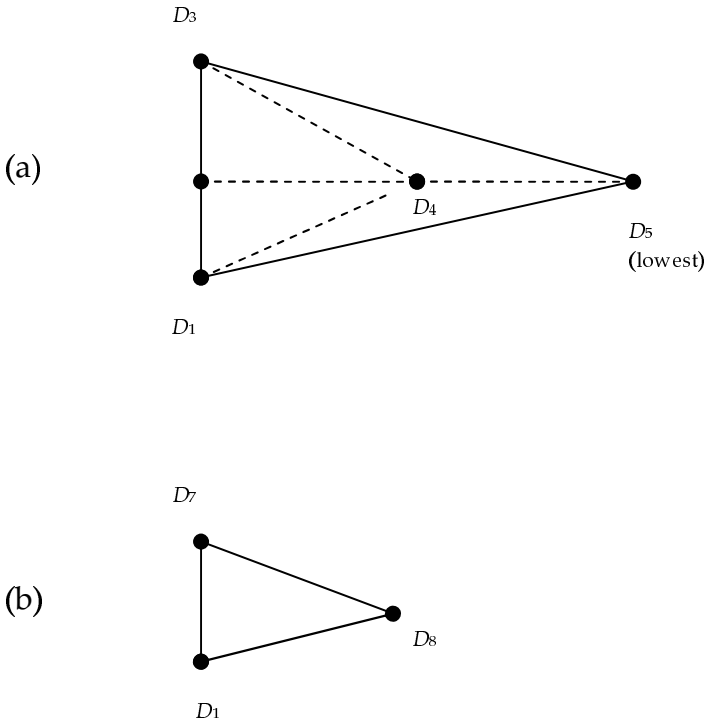

Figure 3.7 (a) Expansion of simplex through the lowest point D_4. **(b)** New form of the simplex after a multiple contraction.

If D_5 is lower than D_4, then the simplex expands in that direction. (Figure 3.7(a)) But, if D_5 is not the lowest, this time contraction towards the lower points occurs. The second shape in Figure 3.7 shows a simplex at a level of the procedure which has undergone a contraction in all directions, i.e., end of a multiple-contraction.

Several steps similar to those explained above constitute the best point which will be one of the starting points for the iteration procedure. The other one, *point B* here, is found in same manner. In order to find the rest of the points or, to obtain the stability curves (Figure 3.3), *Newton Raphson iteration* method has been used. Opposite to simplex method, this technique provides a much faster iteration and hence faster determination of the required points. Expressing the determinant, DET (or *D*) in Eq. (3.20) as:

$$D = D_r + iD_i . \tag{3.25}$$

In this case, it represents two equations (D_r, D_i) with two unknowns (α, c_r). Calling $(\alpha^j, c_r^{\,j})$ as the j^{th} iteration by definition of Newton-Raphson method, the $(j+1)^{th}$ iteration is determined as follows:

$$\begin{aligned} \alpha^{j+1} &= \alpha^j + \Delta\alpha^j , \\ c_r^{\,j+1} &= c_r^{\,j} + \Delta c_r^{\,j} . \end{aligned} \tag{3.26}$$

Expanding the determinant as in Eq. (3.25) about α^j, $c_r^{\,j}$ and by definition, applying $D^{j+1}=0$, a linear system is formed as follows:

$$D_r^{\,j} + \left(\frac{\partial D_r}{\partial \alpha}\right)^j \Delta\alpha^j + \left(\frac{\partial D_r}{\partial c_r}\right)^j \Delta c_r^{\,j} = 0,$$

$$D_i^{\,j} + \left(\frac{\partial D_i}{\partial \alpha}\right)^j \Delta\alpha^j + \left(\frac{\partial D_i}{\partial c_r}\right)^j \Delta c_r^{\,j} = 0. \tag{3.27}$$

Multiplying the first equation by $(\partial D_i / \partial c_r)^j$, the second by $(\partial D_r / \partial c_r)^j$ and subtracting the second from the first; then multiplying the first original equation this time by $(\partial D_i / \partial \alpha)^j$, the second original by $(\partial D_r / \partial \alpha)^j$ following the subtraction, Eqs. (3.27) ends up with the following:

$$\Delta\alpha^j = \frac{1}{J}\left[D_i^{\,j} \left(\frac{\partial D_r}{\partial c_r}\right)^j - D_r^{\,j} \left(\frac{\partial D_i}{\partial c_r}\right)^j \right],$$

$$\Delta c_r^{\,j} = \frac{1}{J}\left[D_r^{\,j} \left(\frac{\partial D_i}{\partial \alpha}\right)^j - D_i^{\,j} \left(\frac{\partial D_r}{\partial \alpha}\right)^j \right], \tag{3.28}$$

where, J is the Jacobian matrix expressed by:

$$J = \begin{vmatrix} \left(\frac{\partial D_i}{\partial c_r}\right)^j & \left(\frac{\partial D_i}{\partial \alpha}\right)^j \\ \left(\frac{\partial D_r}{\partial c_r}\right)^j & \left(\frac{\partial D_r}{\partial \alpha}\right)^j \end{vmatrix}. \tag{3.29}$$

The convergence of the iteration happens when $\left|\Delta\alpha, \Delta c_r\right| \le \varepsilon$. In this study, the convergence criteria has been taken as 10^{-8}. Note that, the Newton-Raphson method can proceed in only one direction. In this case, it is

taken as the negative Reynolds number direction. That means, it fails at the nose region of the curves like Figure 3.3.

Looking at this figure, it is obvious that the stability curve is composed of two branches each having two initial points. Once these points are found by minimization routine, say *point A* and *point B*, the Newton-Raphson finds the rest of the corresponding branch. As it reaches to the nose region, it fails. Then, using another two points obtained by the Simplex method for the other branch, Newton-Raphson restarts iteration and continues up to the nose point in the same manner. Eventually, these two branches are combined to form the complete $R-\alpha$ curve.

CHAPTER 4

PREDICTION OF TRANSITION

4.1 Introduction

Today, one can claim that it is still not possible to make a good prediction about the transition location. However, the industrial needs enforce the studies on trying to reach the best possible results. The last topic of the thesis is based on this subject.

The process of transition to turbulence is a result of three basic and successively divided steps. Receptivity as the first stage, following the linear amplification and the nonlinear amplification as the last step were all accounted for in the first chapter. It was also mentioned that the only stage that the linear theory can be applied is the second one. The other two are still unclear topics keeping many question marks within themselves so, they are mostly not taken into account while solving for the transition prediction by using the linear theory. An important point is that the linear theory alone can not predict the transition location even if it would be assumed that non linear phenomena occurring before the break down to turbulence are negligible in order to let the linear theory to be used up to transition onset.

In this study, transition location will be predicted by using an empirical method in addition to linear stability theory. This method, called *e^n transition prediction method*, is based on an additional assumption about which the following section will give brief information. One of the most useful quantities that the stability theory provides to such problems, namely the *disturbance amplitude ratio (*or, *rate*) will be maintained by this method. The resultant combinations of eigenvalues obtained by the linear stability analysis will then be used in determination of these ratios.

4.2 e^n Transition Prediction Method

e^n method is a commonly used technique for predicting the transition location, and can be treated as the only practical method available for industrial applications. It was in fact, born in 1952 by Smith while studying on a different topic, the Görtler vortices problem. But, as his study was not published at that time, it is known in literature as it was first developed in 1956 again by Smith, but now with Gamberoni [31]. An independent study about this topic was made by Van Ingen at the same time. Hence, it is usually referred to as the *Smith-Van Ingen e^n method*. Both attempts were based on the linear stability theory.

According to the e^n prediction method, transition starts when a small disturbance is introduced at a critical Reynolds number and amplified by a factor of e^n as it moves downstream. That means, breakdown to turbulence occurs when the amplitude of the most amplified TS wave becomes e^n times as large as its initial amplitude. The additional assumption that comes within

this method is then the value of *n-factor*. The latter studies in literature have been performed in order to improve this assumption.

4.2.1 Methodology

The calculation of transition with the e^n method following the linear theory is quite straightforward for the simplest boundary layer flow types, i.e., 2D incompressible flows with two-dimensional disturbances. However, as the compressibility effects are considered, the complexity starts occurring in the calculations. In any case, as a preliminary step, one has to define a new parameter, the *circular frequency* that will be used in the following procedure. The circular frequency, ω_r^* in Hertz can be made dimensionless in the following manner:

$$\omega_r = \frac{\omega_r^* L^*}{U_e^*}. \tag{4.1}$$

As in previous calculations, L^* and U_e^* are the Blasius length scale and the local streamwise edge velocity of the boundary layer, respectively. This parameter was also defined as $\omega_r = kc_r$ in previous chapters (Eq. (2.59)). A wave is introduced into a steady boundary flow with such a particular dimensional circular frequency, and it preserves this dimensional frequency while propagating downstream. In other words, for a normal mode, the dimensional frequency, ω_r^* is constant through the wave propagation, while the other parameters such as the wave number or phase velocity change. However, by making it dimensionless as in Eq. (4.1), it becomes a function of

streamwise distance, x^* because L^* is an x^* dependent scale. It is much preferred to make the frequency dimensionless with the use of kinematic viscosity coefficient, ν^* instead of L^* so that, it could be represented as:

$$f = \frac{\omega_r}{R}, \tag{4.2}$$

where, R denotes the Reynolds number defined as $U_e^* L^* / \nu_e^* = \sqrt{R_x}$. This is the definition of Reynolds number that will be used throughout this study. Even in this form, except for flat-plate boundary layer flows, the dimensionless frequency is still x^* dependent.

For flow cases where the velocity profiles are described by the Falkner-Skan equation, the variable dimensionless frequency takes the form of:

$$f(R) = f(R_0)\left(\frac{R_0}{R}\right)^{\frac{4m}{m+1}}. \tag{4.3}$$

Here, m is the dimensionless pressure gradient parameter, i.e.:

$$m = \frac{x^*}{U_e^*}\frac{dU_e^*}{dx^*}. \tag{4.4}$$

The other parameters seen in Eq. (4.3) are described in the following manner:

$R_0 \rightarrow$ Reynolds number at initial position, x_0^*, where the wave first meets the instability on flat plate, or where it enters the unstable region (see Figure 4.1).
$R \rightarrow$ Reynolds number at any station, x^*.

It is also possible to define the dimensionless frequency, f in terms of the Falkner-Skan parameter:

$$\beta_{FS} = \frac{2m}{m+1}, \tag{4.5}$$

so that Eq. (4.3) becomes:

$$f(R) = f(R_0)\left(\frac{R_0}{R}\right)^{2\beta_{FS}}. \tag{4.6}$$

However, as this study is concentrated on zero pressure gradient boundary layer flows ($\beta_{FS} = 0$), this relation reduces to $f(R) = f(R_0)$. This also proves the statement mentioned in the previous paragraph, i.e., the dimensionless frequency being constant with respect to x^* for flat-plate boundary layer flow cases.

Figure 4.1 illustrates a sample stability curve for the simplest case of this study, i.e., for the flow with two-dimensional disturbances, at M=0. This is the neutral stability curve where the constant temporal amplification factor, c_i is set to zero. Each frequency in this figure corresponds to an independent wave.

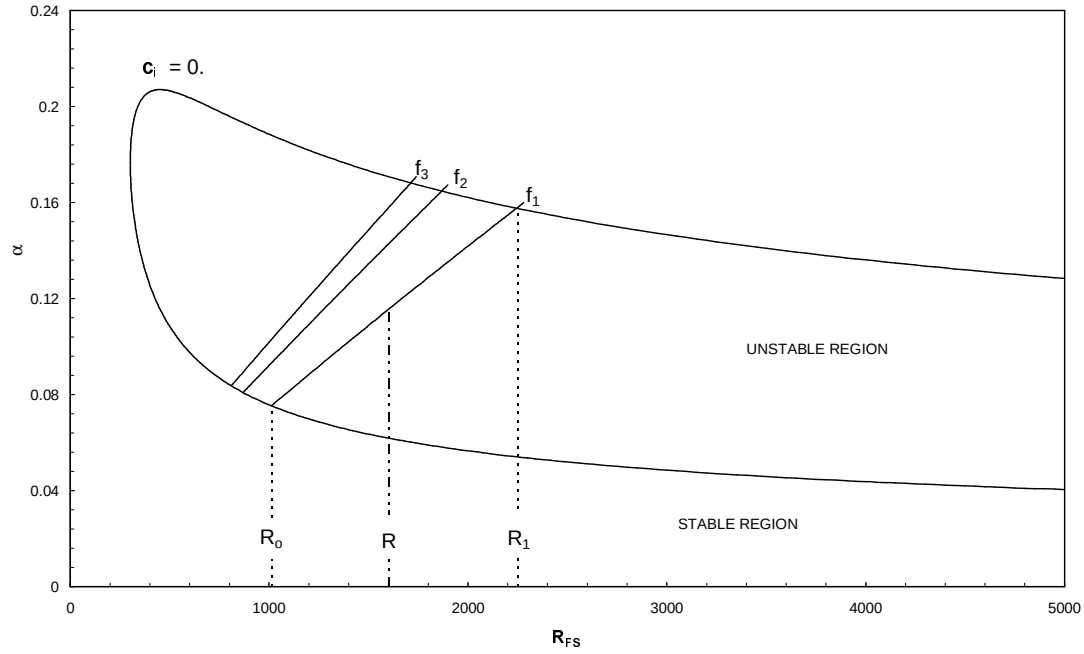

Figure 4.1 Neutral stability curve and sample trajectories of unstable plane waves with constant frequencies at M=0.

In the same figure, Figure 4.1, inner part of the neutral stability curve represents the *unstable region* and outside represents the *stable region* so that a wave with a frequency of f_1 starting in stable region, is damped up to R_0 which is the boundary for the instability. As entering inside the curve, it starts amplifying. Further amplifying lets the wave reach again the stable region as long as transition to turbulence does not happen within that region up to R_1. If it reaches that upper boundary, it starts damping again. One should note that, transition occurs within the unstable region by the most amplified disturbance, and if it occurs, such a curve loses its validity of representing the stability conditions of the flow. One goal of this study is to find the frequency that yields to transition earliest.

Consider a wave moving downstream with a frequency f_w through the boundary layer. As clarified previously, it starts amplifying after passing the neutral point, $R = R_0$. Its amplification at any location within the unstable region can be investigated by using either spatial theory or the temporal theory. In both cases one should note that, the numerical derivations are according to the dimensional quantities denoted by '*'.

Let the first case be the investigation by *spatial amplification theory*. In this case, the growth rate of the disturbance, in general would depend on both components of amplification rate vector, $-\alpha_i^*$ and $-\beta_i^*$. However, as explained in Chapter 2, the change in the amplitude of the spatial wave in x-direction becomes *the only criteria* while analyzing the amplification rates in the case of *z independent* 2D planar boundary layers. Hence, the growth rate reduces to $-\alpha_i^*$ and it would be:

$$\frac{1}{A}\frac{dA}{dx^*} = -\alpha_i^*, \tag{4.7}$$

where, A defines the amplitude of the wave at any streamwise location x^*. This parameter represents the magnitude of the root mean square of the physical disturbances which are the real parts of the normal modes [2]. Integrating this relation with respect to the streamwise direction between x_0^* and any station $x^* \rangle x_0^*$, one can conclude with the amplification ratio of the wave within these locations:

$$\frac{A}{A_0} = e^{\int_{x_0^*}^{x^*} \left(-\alpha_i^*\right)_{max} dx^*} \qquad \text{or,} \qquad \ell n\left(\frac{A}{A_0}\right) = \int_{x_0^*}^{x^*} \left(-\alpha_i^*\right)_{max} dx^* \,, \tag{4.8}$$

A_0 representing the initial amplitude of that wave at $x^* = x_0^*$, (or in dimensionless form $R = R_0$) and A being the amplitude at station, x^*. When the upper bound moves to $x^* = x_1^*$ (in dimensionless form $R = R_1$), Eq. (4.8) gives the total amplification rate of the corresponding wave through the unstable region. An important point is that both amplitudes remain as unknowns throughout this study however; their ratios are to be the vital parameter that will be used in prediction of transition location.

For *three-dimensional disturbance* cases (oblique waves), the local growth rate changes with respect to the wave angle, ψ $(-\alpha_i^*(\psi))$, such that there is a wave number direction at which the local growth rate is maximum at the corresponding streamwise location $(-\alpha_i^*(\psi) = -\alpha_{i\,max}^*)$. This is nothing but the growth rate used in calculation of the amplification ratios. This method is named as the *envelope method* in literature [13]. However, the current analysis will follow a different path which will be clarified in the next pages.

In the case of *two-dimensional disturbances* where $\beta^* = 0$ and $\psi = 0$, this relation reduces to a much simpler form:

$$\ell n\left(\frac{A}{A_0}\right) = \int_{x_0^*}^{x^*} -\alpha_i^* dx^* \,. \tag{4.9}$$

The only difference is that the local growth rate is constant now at the corresponding streamwise location. This makes the calculations much easier than expected.

The integration in Eq. (4.8) (or, Eq. (4.9) in 2D form) constitutes a curve, namely a *constant frequency curve* (Figure 4.2). The *n-factor* that gives its name to this prediction method refers to the maximum amplification rates of these curves. That means:

$$n = \max_{f_w}\left[\ell n\left(\frac{A}{A_0}\right)\right]. \tag{4.10}$$

These n-factors thereby constitute a curve, called *envelope curve*, which is tangent to the curves each representing the variation of amplification rate for a fixed frequency.

A sample plotting is sketched in Figure 4.2 to visualize the relation between the amplification ratios and the stability curves. In Figure 4.2(a), the points where a specified frequency wave starts damping and where it starts amplifying are identified. The amplification ratio curves, i.e., constant frequency curves are illustrated in Figure 4.2(b). Here, the line drawn tangent to the variations of $\ell n(A/A_0)$ represents a curve that gives the maximum amplification rate at any required streamwise location together with the frequency corresponding to this maximum rate. This curve of n-factor is called the *envelope curve*. It is the final step of the stability problem.

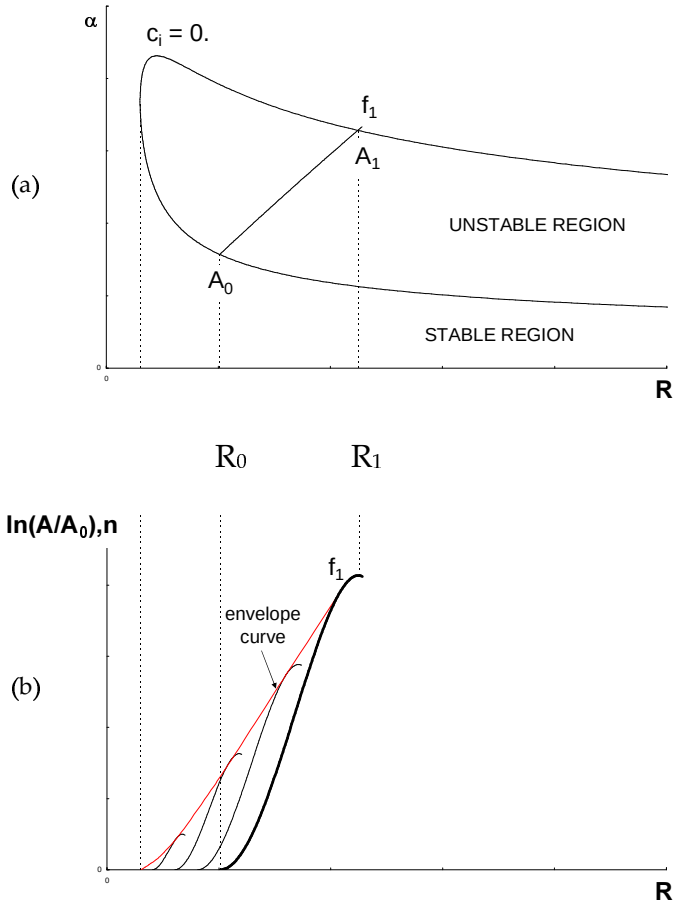

Figure 4.2 A sample representation of a single frequency wave to illustrate the relation between **(a)** the stability curves and **(b)** the amplification ratios together with the envelope curve.

In the case of *temporal amplification theory*, the growth rate of the disturbance is expressed in the form of:

$$\frac{1}{A}\frac{dA}{dt^*} = \omega_i^* = k^* c_i^* . \qquad (4.11)$$

Different from the spatial theory, here the amplitude of a fixed frequency wave changes not with the streamwise distance, but with time.

Then, its amplification rate is calculated by integrating Eq. (4.11) with respect to time, i.e.:

$$\frac{A}{A_0} = e^{\int_{t_0^*}^{t^*} \left(\omega_i^*\right)_{max} dt^*} \qquad \text{or,} \qquad \ell n\left(\frac{A^*}{A_0^*}\right) = \int_{t_0^*}^{t^*} \left(k^* c_i^*\right)_{max} dt^* . \tag{4.12}$$

Here, t_0^* corresponds to a time at which the wave enters the unstable region and t^* corresponds to any time at which the wave amplitude, A is investigated.

For the *oblique waves* in *temporal* case, similar to spatial theory, the local growth rates vary with the wave angle, ψ so that at each corresponding time it reaches a maximum value, $\left(k^* c_i^*\right)_{max}$ which is used in calculation of the amplification ratios as seen in Eq. (4.12).

In fact, to repeat the procedure of determining such an angle, ψ and its corresponding local growth rate at each integration step would make the calculations unnecessarily complicated. For this reason, in the *current oblique wave analysis*, not the wave angle giving the maximum local growth rate, but the one at which the flow is most unstable, i.e., the angle giving the smallest critical Reynolds number will be taken into consideration. The integration will therefore go through that angle.

It is necessary to remember that all results up to now, i.e., the stability characteristics and hence the growth rates are to be found with the use of temporal amplification theory. So, it would be more convenient to continue

with this theory. On the other hand, for a steady basic flow, the amplitude at a fixed point is independent of time, and the variation of the wave amplitude can only be measured by distance. This enforces us to use the spatial theory at that point. But first, one has to convert the obtained temporal growth rates into the corresponding the spatial growth rates. It will be then performed by a method called *Gaster's transformation*.

This transformation was first used by Schlichting in 1933 for two-dimensional disturbances. Later, Lees [32] applied the same relation for the same disturbance type and he justified the method not mathematically, but just intuitively. Its mathematical derivation however, was performed by Gaster in 1962 [22] again for the same flow type. That's why; it is called *Gaster's transformation*. Although it has been derived for two-dimensional disturbances, it can easily be transformed to oblique waves. In this study, both cases will be analyzed. First, the Gaster's relation will be derived starting from oblique waves and then it will be simplified for the plane waves.

Considering an unbounded domain as in this case for a steady basic flow, it is now clear that the normal modes vary continuously with respect to one or more wave numbers. Taking their growth rates relative to each other, one can see that they are considerably close to each other. This explains the reason why the most unstable mode is just the first of these modes. So, for linear instability an unstable disturbance carries the character of not a single wave but a group of waves (wavepackets) which are similar to the most unstable mode. The velocity at which these wavepackets propagate is called

the group velocity. It is absolutely different from the phase velocity of a single (monochromatic) wave.

This new parameter, the *group velocity* is the one that is used by *Gaster's transformation* to make a relation between the temporal and the spatial theories. For the oblique waves, it is defined as:

$$\vec{c}_g{}^* = \left(\frac{\partial \omega^*}{\partial \alpha^*}, \frac{\partial \omega^*}{\partial \beta^*} \right). \tag{4.13}$$

In reality, this parameter is complex however; its imaginary part is very small compared to its real part, so only its *real* part is taken as the group velocity. In *temporal* case, this approximation leads us to use only the real part of complex ω^* while defining the group velocity. Accordingly, its magnitude and angle with respect to x-direction are as follows:

$$c_g{}^* = \sqrt{\left(\frac{\partial \omega_r^*}{\partial \alpha^*} \right)^2 + \left(\frac{\partial \omega_r^*}{\partial \beta^*} \right)^2}, \qquad \psi_g = \tan^{-1}\left[\frac{\partial \omega_r^* / \partial \beta^*}{\partial \omega_r^* / \partial \alpha^*} \right]. \tag{4.14}$$

In Gaster's transformation, this magnitude is used to make a relation between the time derivation and the derivation with respect to $x_g{}^*$, the coordinate in the direction of the real group velocity:

$$\frac{d}{dt^*} = c_g{}^* \frac{d}{dx_g{}^*}. \tag{4.15}$$

Applying it to Eq. (4.7) and Eq. (4.11), one ends up with the following relation:

$$-\left(\alpha_i^*\right)_g = \frac{\omega_i^*}{c_g^*} = \frac{k^* c_i^*}{c_g^*}, \tag{4.16}$$

which is used for the oblique waves to convert the temporal growth rate to the spatial growth rate along the direction of real group velocity. One should note that this relation is just an approximation valid for the small amplification rates which correspond to the ones near to the neutral stability curve.

Now, applying this transformation to the spatially defined amplification ratio in Eq. (4.8) as:

$$\ell n\left(\frac{A}{A_0}\right) = \int_{x_0^*}^{x^*} \frac{\left(k^* c_i^*\right)_{max}}{c_g^* \cos\psi_g} dx^*, \tag{4.17}$$

so that it would be possible to find the desired spatial amplification rates of the fixed frequency waves by using their appropriate temporal growth rates obtained in previous chapters. The envelope of the wave can be calculated in the same manner:

$$n = max_{f_w}\left(\int_{x_0^*}^{x^*} \frac{\left(k^* c_i^*\right)_{max}}{c_g^* \cos\psi_g} dx^*\right). \tag{4.18}$$

However, this relation is composed of dimensional parameters. Because all calculations and results of the stability analysis up to now are based on dimensionless parameters, it is more convenient to make this relation also nondimensional. Hence, in terms of dimensionless parameters:

$$n = \max_{f_w}\left[\ell n\left(\frac{A}{A_0}\right)\right] = \max_{f_w}\left(\int_{R_0}^{R}\frac{2\left(kc_i\right)_{max}}{c_g\cos\psi_g}dR\right), \tag{4.19}$$

where, R_0 represents the Reynolds number at the neutral stability point and R corresponds to any Reynolds number along the constant frequency trajectory. At that point, it would be beneficial to state that the spanwise component of the group velocity is much smaller than its streamwise component so that the calculations would be much easier if one neglects this small component. This can easily be proved by numerical computations. In this respect, the group velocity is redefined as $\partial\omega_r/\partial\alpha$ and the envelope as:

$$n = \max_{f_w}\left[\ell n\left(\frac{A}{A_0}\right)\right] = \max_{f_w}\left(\int_{R_0}^{R}\frac{2\left(kc_i\right)_{max}}{c_g}dR\right). \tag{4.20}$$

This is the basic equation that will be used in the following chapters to reach the transition location in the case of *oblique waves*. One has to know that, a similar rearrangement had also been used by Arnal [2], but with a different approach in obtaining $\left(kc_i\right)_{max}$ leading to locally varying wave angle. In the current analysis however, the integration will proceed for a fixed angle giving the smallest critical Reynolds number.

For the *plane waves*, the determination of the maximum amplification rate (n) is much easier. In this case, $\beta^* = 0$ that means the group velocity is in the same direction with the streamwise wave number. In this respect, it is redefined as:

$$c_g{}^* = \frac{d\omega^*}{d\alpha^*}. \tag{4.21}$$

For temporal amplification theory, it reduces to:

$$c_g{}^* = \frac{d\omega_r^*}{d\alpha^*} = \frac{d\left(\alpha^* c_r^*\right)}{d\alpha^*}. \tag{4.22}$$

In parallel, the Gaster's transformation is also simplified. Making a relation between the time derivation and the derivation with respect to streamwise direction x^* as:

$$\frac{d}{dt^*} = c_g{}^* \frac{d}{dx^*}, \tag{4.23}$$

the temporal and spatial theories are transformed to each other in the following form:

$$-\alpha_i^* = \frac{\omega_i^*}{c_g{}^*} = \frac{\alpha^* c_i^*}{c_g{}^*}. \tag{4.24}$$

Due to these simplifications, the amplification rate of a two-dimensional wave is rearranged such that:

$$\ell n\left(\frac{A}{A_0}\right)=\int_{R_0}^{R}\frac{2(\alpha c_i)}{c_g}dR\,, \tag{4.25}$$

and Eq. (4.19) turns into a form which is the basic equation that will be used in the following chapters to reach the transition location in the case of *two-dimensional waves*:

$$n=\max_{f_w}\left[\ell n\left(\frac{A}{A_0}\right)\right]. \tag{4.26}$$

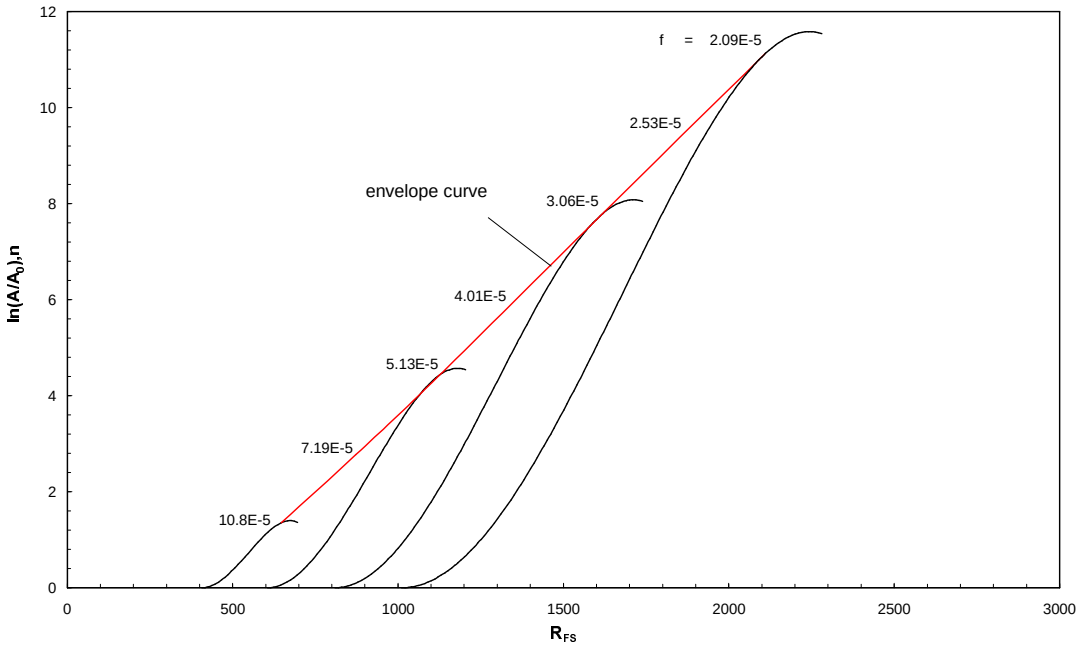

Figure 4.3 Progress of amplification rates for some constant frequency waves at M=0 and the envelope curve.

Figure 4.3 shows an example to the dimensionless results calculated for two-dimensional disturbance cases at M=0 by using Eq. (4.25). S-shapes are the constant frequency curves each of which corresponds to an independent wave. The tangent line to these shapes defines the envelope curve. Each n-factor on this line represents the maximum amplification rate at the corresponding Reynolds number.

However, the transition location is still unknown. The next and the last step is to find or estimate the value of n-factor at which the transition occurs. Once it is found, the Reynolds number corresponding to that value across the envelope curve will be the one that breakdown to turbulence occurs and it is called *transition Reynolds number* (R_{tr}). This n-value will also help to find the frequency that yields the highest amplification rate, i.e., the one which yields transition faster.

4.2.2 The Value of *n-factor*

In the framework of the current compressible stability analysis, the following procedure is applied:

- Determination of the 2D compressible laminar mean flow velocity and temperature profiles together with their derivatives.
- Calculation of the stability characteristics of the temporally amplified two- and three-dimensional disturbances by using these mean flow properties.

- Determination of the amplification rates by the spatial theory for the fixed frequency waves whose temporal growth rates are converted to appropriate local spatial rates by Gaster's transformation.
- Definition of the envelope curve with the use of these constant frequency amplification ratio curves.
- Prediction of the transition location, or (R_{tr}), with the use of envelope curve and an appropriate n-factor.

The estimation of the n-factor is based on an assumption, an additional one to those up to now. However, the prediction of transition location highly depends on this assumption and one should be very careful on deciding this value. It depends on the nature of flow, i.e., whether two- or three-dimensional, on the Mach number range of the flow and so on. Unfortunately, no general theory exists which could give the correct n-value for any kind of stability problem. However, there are a number of studies in literature each using the experimental definitions of the transition location to reach a crude n-value satisfying the required conditions. This makes the n-factor depend on not only the flow type or Mach numbers, but also the experimental conditions (freestream turbulence, noise, etc.).

The first assumption about this factor was made by Smith and Gamberoni [31]. According to their studies, transition was occurring as the disturbance amplitude enlarges with an exponential factor of 9. This was maintained by a series of comparisons of their numerical results with the experimental data. The solutions were within at most 20% error. At the same time, van Ingen found a similar result but with a factor e^7 or e^8. The different solutions explain why the method is known as e^n *method*, not e^9.

This difference most probably comes from different experimental conditions or different wind tunnels used in experiments.

Afterwards, the same topic was studied by Jaffe, Okamura and Smith on various shapes. They calculated the spatial growth rates of the waves by using exact solutions of the Orr-Sommerfeld equation for the locally calculated mean velocity profiles. In conclusion, they found good correlations by using an amplification ratio of e^{10}. Actually, their experimental results about these ratios where the transition occurs in low turbulence wind tunnels were obtained in a range of $e^{6.8}$ and $e^{12.1}$. This in fact shows that, there would be cases at which the linear instability is the dominant in transition, rather than nonlinear instability where the disturbances are let amplify further.

This was also mentioned by Arnal [2] in simpler words, but just considering the flat plate conditions with zero pressure gradient. According to him, in such cases the distance between the end of the linear region and the breakdown to turbulence is sufficiently short, i.e. the range of the linear amplification occupies nearly 75% of the streamwise distance between the leading edge and the transition location. This is also a good explanation to the question of why most of the practical transition prediction processes are based on linear stability only.

In literature, the typical value for n is usually 9 for low turbulence and free flight conditions yielding very good results in incompressible analyses. However, this value is also known to be affected by the Mach number [12]. In this respect, for the estimation of maximum amplification

factor, Mack's proposal [12] will be taken as reference in the current study rather than using a constant value. What he implies is that the disturbance environment changes with Mach number, so the initial amplitude A_0 which depends on the disturbance environment must change as well. Accordingly, the transition criterion is redefined as:

$$\frac{A}{A_r} = \frac{A_0}{A_r}\frac{A}{A_0}, \tag{4.27}$$

denoting a constant ratio with a fixed reference amplitude A_r. Although it is a constant its components, A_0/A_r and A/A_0 are both functions of Mach number. A/A_0 is defined by Mack [12] as the contribution to the final disturbance amplitude from instability. It is actually the transition criterion that the current study searches for. The other ratio A_0/A_r which is found by the amplitude of the external disturbances and their interaction with the boundary layer is formulated as:

$$\frac{A_0}{A_r} = \left(\frac{M}{M_r}\right)^2, \tag{4.28}$$

through the measurements of Laufer [33] indicating that the pressure fluctuation in the freestream is proportional to freestream Mach number, M^2 within the range of $M = 1.6$ and $M = 5$. Here, M_r represents the reference Mach number where the initial amplitude is to be the reference amplitude, A_r. With Eq. (4.28), the initial amplitude, A_0 shows variation with M^2. This relation makes the transition criterion, A/A_0 be proportional to $1/M^2$.

For the determination of the transition criterion, the first step is to be the choice of A/A_r value. Mack's studies are concentrated on $A/A_r = 100$ and $A/A_r = 400$. Actually, his aim was to obtain results approximate to the transition data found by some wind tunnel experiments. Therefore, he maintained the most suitable A/A_r value(s) by trial and error. In this study, with a similar approach, a range of A/A_r between 100 and 400 will be tried so that the best transition criterion would be found for the results to converge the ones in literature found by the wind tunnel experiments.

The other parameter, A_0/A_r in Eq. (4.27) is calculated for the corresponding freestream Mach number using Eq. (4.28). Finally, the maximum amplification rate that gives the transition Reynolds number is obtained by inserting those into Eq. (4.27). To be consistent with the Mack's solutions, M_r is taken as 1.3 in this study and A_0 is assumed to be *constant* with a magnitude of A_r for Mach numbers less than that reference value ($M_r < 1.3$), i.e.:

$$\frac{A_0}{A_r} = 1 \qquad \text{for} \qquad M_r < 1.3,$$

$$\frac{A_0}{A_r} = \left(\frac{M}{M_r}\right)^2 \quad \text{for} \qquad M_r > 1.3. \tag{4.29}$$

4.2.3 Shortcomings of the e^n Method

Since the e^n method is based on linear stability, receptivity and non-linear mechanisms that the linear theory does not account for are also the

ones neglected by the e^n method. The neglect of the non-parallel effects is another shortcoming in the current procedure.

Receptivity, as defined in Chapter 1, describes the mechanisms that cause freestream disturbances to enter the boundary layer and create initial amplitudes for unstable waves. It is the first stage of the transition process that is, the initial amplitudes of the disturbances A_0 are the topics of receptivity. In the e^n method whereas, the value of the initial or any current amplitude is not important individually. The main goal is to find their ratio. However, the stability characteristics obtained by the linear theory are the ones that ignore the receptivity mechanisms. This neglect naturally affects the e^n method which uses these characteristics as inputs.

As mentioned clearly, the nonlinear mechanisms corresponding to the region of high amplifications are to be neglected in linear theory. However, it was clarified by Arnal [2] that the distance between the end of the linear region (region where linear theory is applied) and the breakdown to turbulence is very short. The reason could be the evolution of the peak-valley structures at a very fast rate. It was also mentioned previously that, for the typical flat plate conditions, the linear amplification range is $75\% - 85\%$ of the streamwise distance between the leading edge and the transition location. This is a high range that lets the linear theory give satisfactory results [2]. The same conclusion is also valid for the current e^n method.

However, for compressible flows there is no an extensive result about this problem. The only conclusion is that at high Mach numbers, the temperature and the density fluctuations show a sharp peak near the edge of

the boundary layer where the nonlinearity starts to develop. But, no satisfactory result exists about this topic and how much it affects the e^n method is still questionable.

The shortcoming caused by the non parallel effects comes from the parallel flow assumption applied during the linear stability analysis (see Chapter 2). For two-dimensional disturbance cases, the growth rates are weakly affected by this assumption. It was shown numerically by Gaster [34], Bertolotti [35] and Chang et al. [36] using PSE (parabolized stability equations). However, as the Mach number increases, the effect of this assumption starts showing itself. Figure 4.4 demonstrates some of the results reported by Arnal [2].

On the other hand, for oblique cases the situation is quite the opposite. Figure 4.5 is a sample plotted by Arnal [2] to illustrate the effect of the parallel mean flow assumption on the growth rates. It is clear that the resultant amplification rates become less due to parallelism. However, many studies about this topic in literature use this crude but simplifying assumption.

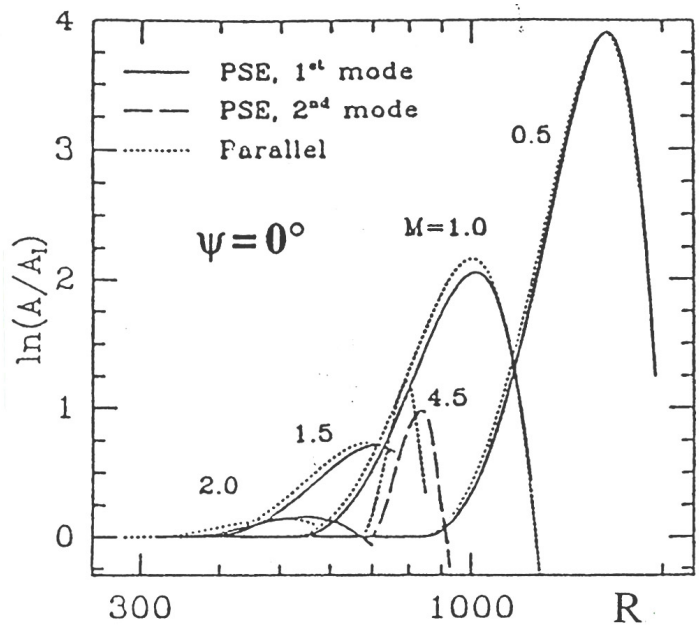

Figure 4.4 A study by Arnal [2] showing the parallel flow effect on the amplification rates of the plane waves.

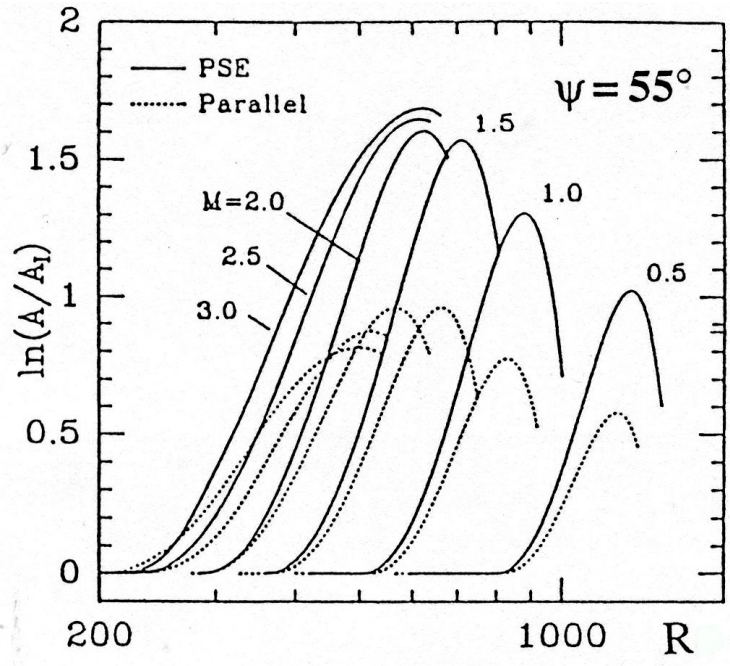

Figure 4.5 A study by Arnal [2] showing the parallel flow effect on the amplification rates of the oblique waves.

CHAPTER 5

RESULTS AND DISCUSSION

5.1 Introduction

The current chapter is concerned with the results of the stability and transition analyses performed throughout this study using the methods outlined in previous chapters for two-dimensional mean flow in compressible boundary layer over a flat plate with adiabatic wall condition. Following the derivations of the governing system of equations in Chapter 2, a FORTRAN code has been written in order to solve the linear stability problem and hence, to obtain the certain combinations of wave parameters (α,β ,ω,R) by implementing the methods mentioned in Chapter 3. The program is capable of solving this eigenvalue problem for either *two-* or *three-dimensional sinusoidal disturbances* by using temporal amplification theory.

The first type to be investigated is the 2D Blasius boundary layer with two-dimensional disturbances. Different configurations of the resultant eigenvalues and their comparison with the corresponding ones in literature will cover the first section. It is actually the preliminary step for the stability analysis of three-dimensional disturbances in 2D Blasius flow over an adiabatic flat plate which will be the topic of the next section. In this case, the

results will again be compared with the available data in literature. Finally, the transition analysis composed of finding the amplification ratios of the most unstable waves each having the constant frequencies and determination of their envelope will be examined as an independent section which also includes comparison with literature.

As clarified in previous chapters, some of the parameters remain constant throughout this study. Once more, these are the specific gas constant R^* as $287\ J/kg.K$, the Prandtl number Pr as 0.72, the dimensional Sutherland constant S_1^* as $110\ K$ and the specific heat ratio γ as 1.4. Also, one should note that the currently obtained governing equations are for 3D boundary layer flows. So, for the current 2D mean flow case, the spanwise mean velocity component W and its derivatives are to be taken as zero.

5.2 Two-dimensional Disturbance Case

This case can be regarded as the preliminary step for the analysis of two-dimensional mean flow having oblique waves. This is in fact, a necessity to concentrate first on this case in order to check the validity of the current effort before attempting to solve the oblique case. Besides, this leads us to realize the effect of three-dimensionality on disturbances, and hence on instability in a better aspect.

Starting from the governing equations, the wave number component β is set to zero. The computer code that has been written in the framework of the theory and the numerical methods explained in the previous chapters,

gives solutions proper for the current case only by introducing the wave angle ψ as zero.

The typical representation of eigenvalues is the (α, R) diagram such as Figure 5.1. This figure illustrates the constant temporal amplification curves of 2D Blasius flow at M=0. The outermost curve corresponding to $c_i = 0$ represents the curve of neutral stability. As mentioned in Chapter 4, it is the curve by which the unstable (disturbances are amplified) and the stable (disturbances are damped) regions are separated. Once again, the stable region corresponds to outside this curve and the unstable region to its inner part. An important point is that both temporal and spatial amplification theories give exactly the same neutral stability curve in shape when applied for the same flow conditions.

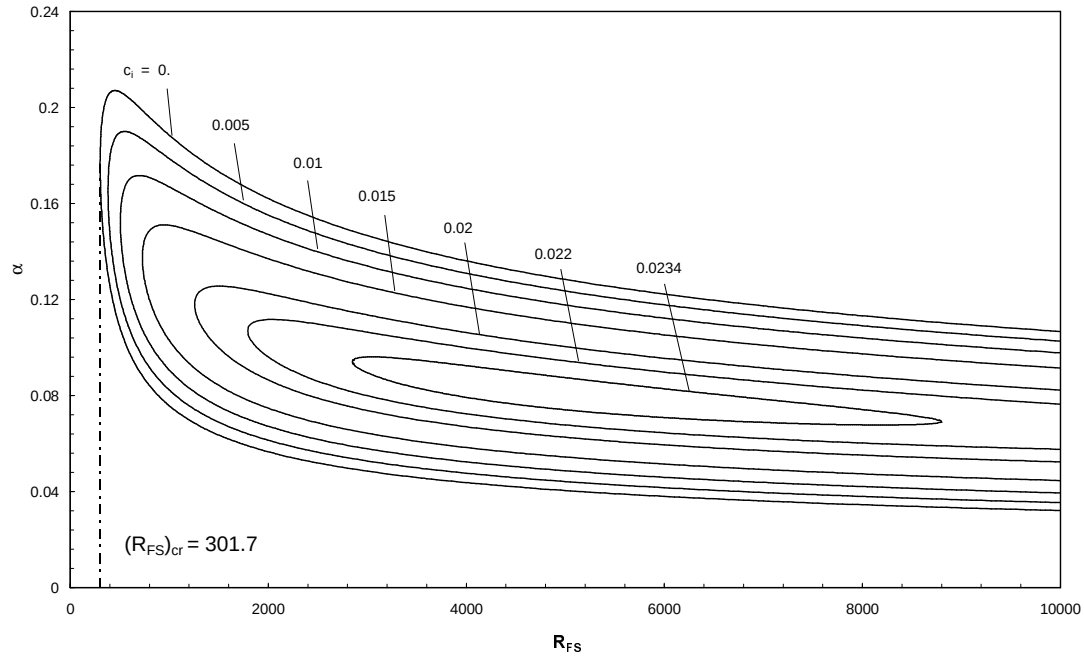

Figure 5.1 Constant temporal amplification curves for plane waves at M=0.

A vital key for the linear stability analysis clarified by the neutral stability curve is the *critical Reynolds number*. This value, at which the instability is first introduced to the flow, corresponds to the point on this curve where the Reynolds number has its smallest value. At Reynolds numbers below R_{cr}, all the disturbances are stable no matter what their wave numbers are. Figure 5.1 exhibits it with a dotted line.

The privilege of this graph compared to the other stability curves to be plotted in the following pages is that its isolines are also the ones corresponding to the *incompressible* boundary layer flow cases. It can easily be confirmed by setting the freestream Mach number to zero in the governing equations for the compressible 2D boundary layer flows with plane waves. Through this information, these curves as well as the critical Reynolds number are then compared with the proper incompressible results in literature. The results of Özgen [17] and Baines et al. [15] both represented in terms of displacement thickness show a perfect agreement with the curves of the current study. Moreover, the critical Reynolds number which is $(R_{FS})_{cr}$ =301.7 , or $(R_{\delta^*})_{cr} \approx 520$ (see Table 5.1) in the present analysis matches in excellent manner with what has been demonstrated by Schlichting [4]. This is the first step in confirmation of the solution method and the code written in this study.

Similar (α, R) configurations are then plotted for different Mach numbers. Figure 5.2 is a visualization of the constant amplification curves for plane waves on (α, R) plane at sonic speed. As moving inside the unstable region where the amplification factors enlarge, the isolines embrace a smaller

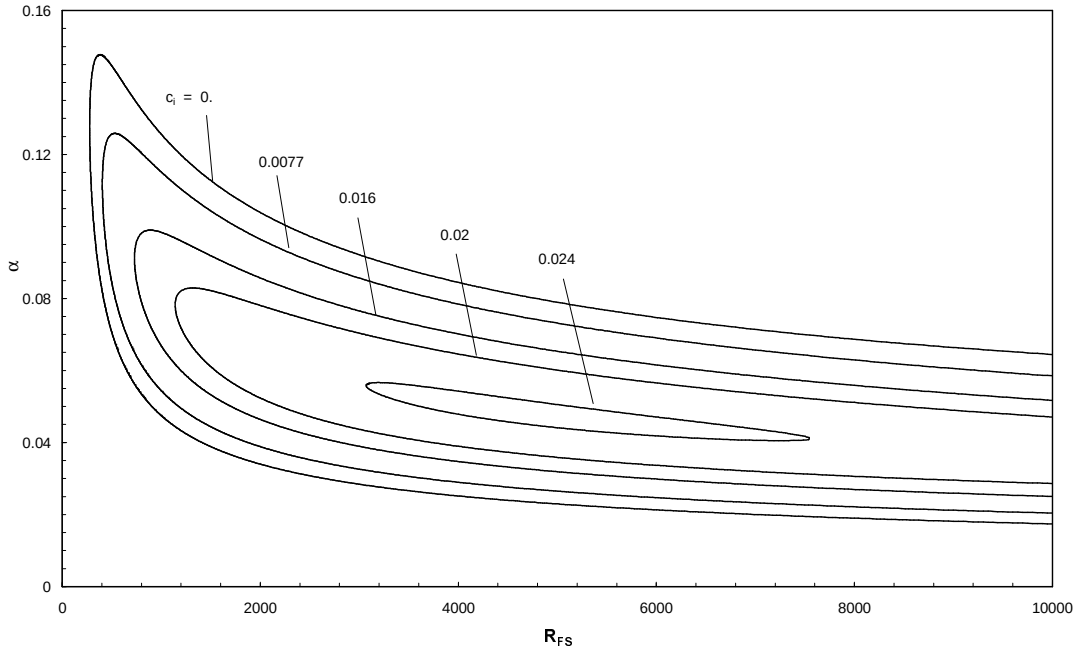

Figure 5.2 Constant temporal amplification curves for plane waves at M=1.

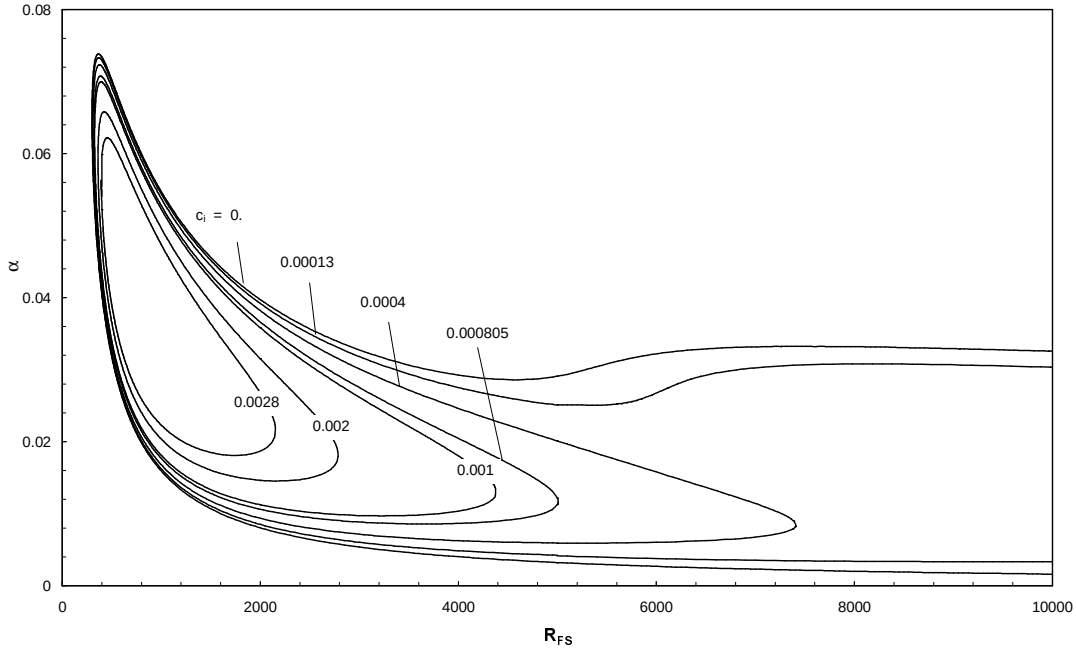

Figure 5.3 Constant temporal amplification curves for plane waves at M=2.

and smaller region. Comparing with Figure 5.1, one inevitably observes the slight motion of the curves towards the peak point appearing at finite Reynolds numbers. For the critical Reynolds number whereas, a slight increase is recognizable at current speed compared to M=0.

These effects are shown better in Figure 5.3, a similar one for a larger Mach number, M=2. Here, the shift of the curves towards the peak point is much more apparent. This was also illustrated by Arnal [2] at similar Mach number range. However, since he used the spatial amplification theory in his calculations, the shapes of the constant amplification curves except for the neutral stability curve show difference as expected. The critical Reynolds numbers are however within great agreement. For the numerical comparison, one can refer to the following pages.

Isolating the curves of neutral stability as in Figure 5.4, one can realize the effect of Mach number on instability much clearly. Looking at this figure illustrating some of these curves corresponding to low Mach numbers within M=0 and M=1, the first observation would be the slight motion of the neutral stability curve towards lower wave numbers (i.e., longer waves) without a considerable change on its shape with the increase of Mach number. That is, the wave numbers where the instability occurs get smaller. In spite of this fact, the unstable region remains within almost the same width. Meanwhile, the critical Reynolds number, below which all the waves are damped, decreases gradually. The numerical values calculated within this Mach range are listed below in Table 5.1.

Unfortunately, neither numerical nor experimental data are available

at such low Mach number values in literature. The only evidence which is maintained by the studies of Arnal [2] is that the minimum Reynolds numbers at M=0 and M=1.3 depict a slight increase remaining within the same order of magnitudes. One should note that, his analysis and numerical results are based on the displacement thickness. The present analysis is whereas, in terms of Blasius length scale. Therefore, before the comparison, one has to convert the current results into the proper ones using a multiplicative constant which is indeed, the displacement thickness nondimensionalized by the Blasius length scale ($\delta_1 = \delta^* / L^*$). Table 5.1 gives the necessary data used for the conversion as well as the resultant Reynolds numbers. At this point, one can see the expected gradual increase in R_{cr}.

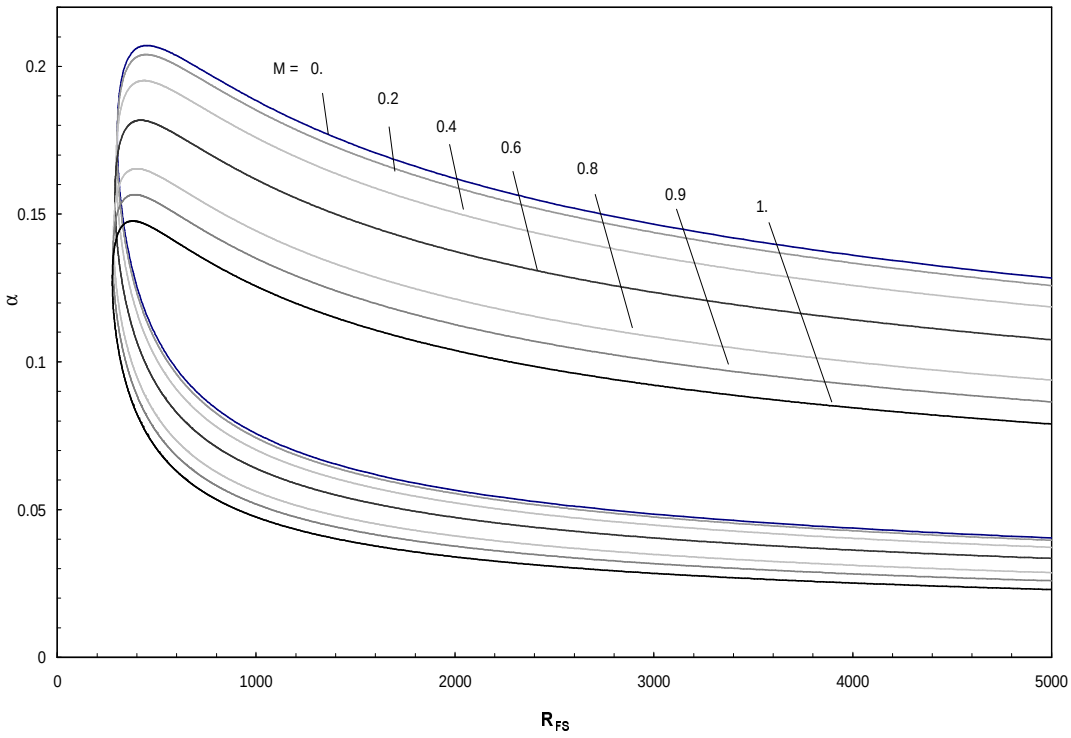

Figure 5.4 Neutral stability curves for plane waves at Mach numbers from M=0 to M=1.

Table 5.1 Effect of Mach number on critical Reynolds number for plane waves within the range of M=0 and M=1.

Mach no.	$(R_{FS})_{cr}$	δ_1	$(R_{\delta^*})_{cr}$
0.0	301.70	1.72	518.82
0.2	300.27	1.74	522.33
0.4	332.66	1.78	527.01
0.6	323.01	1.86	539.31
0.8	315.69	1.98	560.17
0.9	309.56	2.05	572.87
1.0	276.37	2.12	585.90

Before proceeding further, it would be necessary to define a new parameter essential for the compressible flows and for the interpretation of the following results. This parameter, so-called the *generalized inflection point,* is known to be a sufficient condition for the appearance of unstable disturbances for compressible flows [6]. As known from Rayleigh's theorem for the inviscid incompressible flows [4], the existence of an inflection point, y_k, at which the second derivative of the streamwise mean velocity component is zero ($(U'')_{y_K} = 0$, (') denoting the differentiation with respect to dimensionless y distance), constitutes a sufficient condition for the occurrence of the instability. In inviscid theory where the viscosity is assumed to act only on the mean flow profiles and to be neglected in stability equations (neglect of the terms with $1/R$), this happens to be an important mathematical result and a necessary condition for the instability to occur. However, in the viscous theory corresponding to finite Reynolds numbers, it is not a must. For instance, the Blasius profile has an inflection point at the wall and yet it is known that it may become unstable even though Rayleigh's theorem predicts it to be unconditionally stable.

In compressible flows, the situation is a bit different. The inviscid instability analysis performed by Lees and Lin [4] shows that different from the incompressible theory, the sufficient condition for the occurrence of unstable waves is now the existence of a point where $(\rho U')'_{y_k} = 0$.

This point, namely the *generalized inflection point,* has great importance for compressible flat plate boundary layers and its importance is felt more as the flow speed increases. It was previously mentioned while discussing Figure 5.4 that although the curves of neutral stability move downwards with the increase of Mach number, their shapes do not deform too much. This observation is also achieved in Figure 5.5 representing the similar curves for the Mach numbers from M=1 to M=2. As the Reynolds number decreases, these curves converge themselves to make a peak at some finite value. This is almost the same for all neutral stability curves plotted in these figures. Arnal [2] has similar stability analysis not for a range but for individual values of M=0 and M=1.3. He explains the similarity in shape on the corresponding neutral stability curves by the dominant effect of viscous instability on the boundary layer within this Mach number range. In other words, the generalized inflection point remains very close to the wall in this interval and this causes the boundary layer to be unstable under the effect of viscosity [2]. Figure 5.5 supports this aspect and moreover clarifies that it is possible for this viscous instability to be dominant up to M=2.

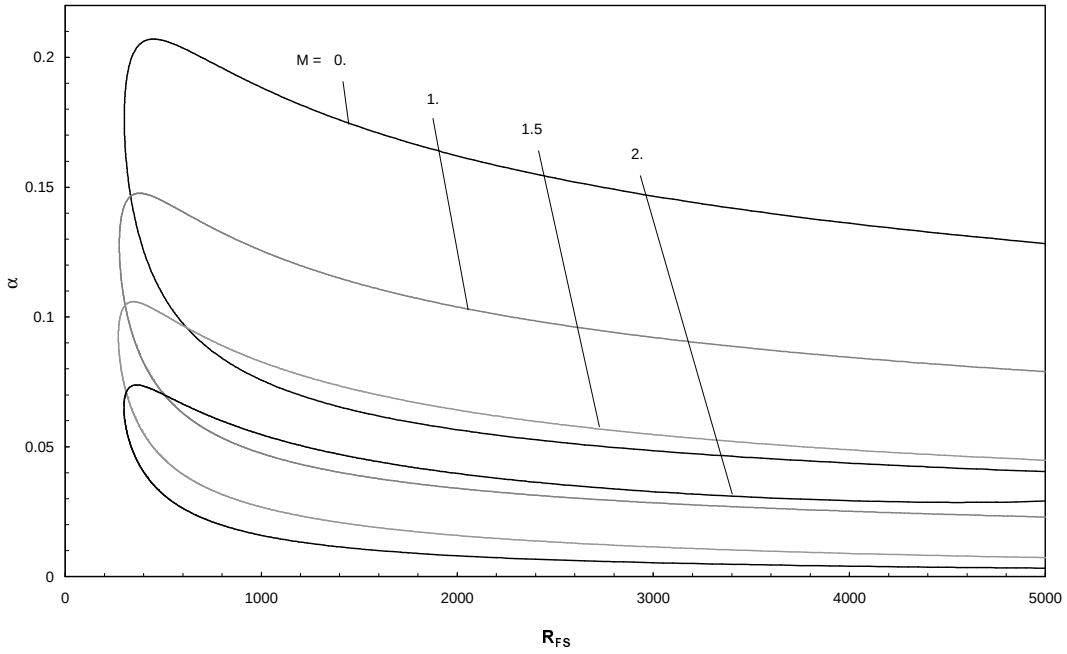

Figure 5.5 Neutral stability curves for plane waves at Mach numbers between M=1 and M=2.

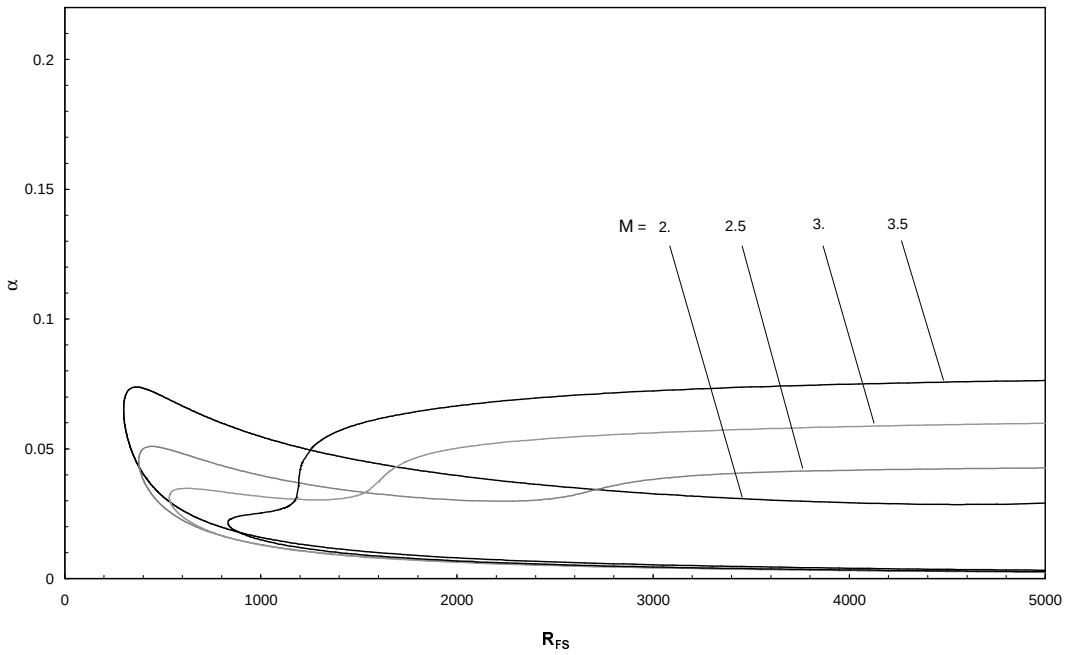

Figure 5.6 Neutral stability curves for plane waves at Mach numbers between M=2 and M=3.5.

However, at higher Mach numbers, the inflection point moves further away from the wall towards the edge of the boundary layer and this causes the generalized Rayleigh's inviscid instability mechanism to be the dominant [12]. In this case, these curves tend to be parallel to the R-axis and the range of unstable wave numbers increases at large Reynolds numbers. Through this point of view, one can easily observe the ranges of viscous and inviscid instabilities on the stability curves at Mach numbers between M=2.5 and M=3.5 in Figure 5.6. Here, the viscous instability range gets smaller with the increase of Mach number, i.e., the inviscid instability starts to dominate much earlier so that it happens at $R_{FS} \cong 2000$ for M=3.5. Comparing them with Arnal's [2] solutions at M=2.2 and M=3.8, one sees a very good match with the present ones. This argument is also what perfectly supported by Mack's observations on this Mach range [12] as well.

Figure 5.5 and Figure 5.6 demonstrate also the variation of critical Reynolds number with the freestream Mach number. From M=0 to M=1.5, this value at which the instability of two-dimensional disturbances is first introduced to the boundary layer flow, shows a slight decrease without changing its order of magnitude. This slight change turns into a considerable increase after M=1.5 to the end of the Mach range, M=3.5.

In literature, many investigations about similar topics include results in terms of different length scales. Arnal [2] has some numerical data based on displacement thickness, δ^*. Some of them were previously used in confirmation of low Mach number results. Here, the current values are similarly converted into the proper ones based on this scaling factor by using

the same multiplicative ($\delta_1 = \delta^* / L^*$). Table 5.2 represents these constants and the resultant critical Reynolds number values.

Table 5.2 Critical Reynolds number values at the Mach numbers between M=0 and M=3.5.

Mach no.	$(R_{FS})_{cr}$	δ_1	$(R_{\delta^*})_{cr}$
0.0	301.70	1.72	518.92
1.0	276.30	2.12	585.76
1.5	271.69	2.61	709.11
2.0	299.86	3.27	980.54
2.5	377.15	4.08	1538.77
3.0	532.40	5.02	2672.65
3.5	832.02	6.07	5050.36

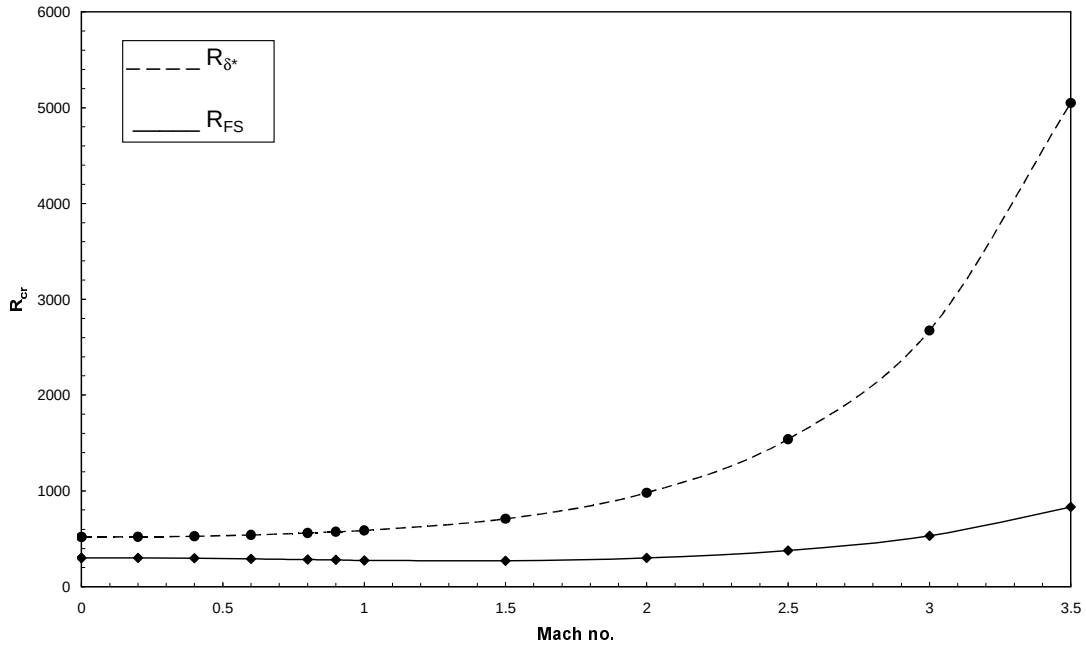

Figure 5.7 Effect of Mach number on critical Reynolds number for plane waves, from M=0 to M=3.5.

Figure 5.7 depicts the critical Reynolds values in terms of both Blasius length scale and displacement thickness together with the previous results given in Table 5.1 so as to let the gradual changes be observed better. It is clear that the previous gradual decrease between M=0 and M=1.5 disappears in the representation of critical Reynolds number with respect to displacement thickness and it turns into a continuous increase from M=0 to M=3.5.

The investigations of Arnal [2] are limited to specific Mach number cases that are not exactly the ones currently studied here. Besides, all his results are of spatial amplification theory, so his constant amplification isolines except for the neutral stability curves, do not have to match or even resemble the ones presently obtained. Nevertheless, comparison of the neutral stability curves as well as the critical Reynolds number values with those corresponding to near Mach numbers can give an idea about the current results.

At M=0, what Arnal obtains perfectly coincides with the present case after being converted into the same length scale (displacement thickness). Looking at the spatial stability diagrams he had found at M=1.3, one can see that the critical Reynolds number is at around $R_{\delta^*} \cong 600-630$ which is quite acceptable taking into account the present values of $\left(R_{\delta^*}\right)_{cr}$ at M=1 and M=1.5. Similarly, his value of $\left(R_{\delta^*}\right)_{cr}$ at M=2.2 occurring nearly between $R_{\delta^*} \cong 1100-1300$ is also in accord with the current results obtained at M=2 and M=2.5. However, it could be hard to claim about a similar compatibility for M=3. As Table 5.2 declares, the unstable disturbances are introduced into

the boundary layer flow at $R_{\delta^*} \cong 2673$. On the other hand, this occurs at around $R_{\delta^*} \cong 2000 - 2100$ according to Arnal's results [2]. This discrepancy is followed by the small difference of the neutral stability curve at that Mach number with the current one in Figure 5.6.

Even though the critical Reynolds numbers and the neutral stability curves corresponding to M=1.3 and M=2.2 are pretty much acceptable, in fact, it would be too much to expect a perfect coincidence between the current results and Arnal's since there are many unclear points about the compressible equation system he had solved for the perturbations. For instance, it is unknown which of the important parameters had been used as constant and which of them as temperature variable such as the Prandtl number. Besides, he mentions nothing about the mean flow energy equation and how he had included this essential part of the compressible theory to the stability problem. Actually, there is nothing much about the governing equations he had used to get the currently mentioned results. He only gives general information and some important theoretical aspects about the compressible linear stability theory.

The stability diagrams obtained up to now are represented differently in Figure 5.8 so that they could be compared with the ones presented by Mack [11] at similar Mach numbers (see Figure 5.9). The neutral stability curves are plotted for M=1.5, M=2 and for M=2.5 in the Figure 5.8. These diagrams similar to the previous ones, divide the stable region which is the outer part, and the unstable region corresponding to the inner part. The peak points whereas, give the critical Reynolds number values at a scale of $1/R_{FS} x10^3$.

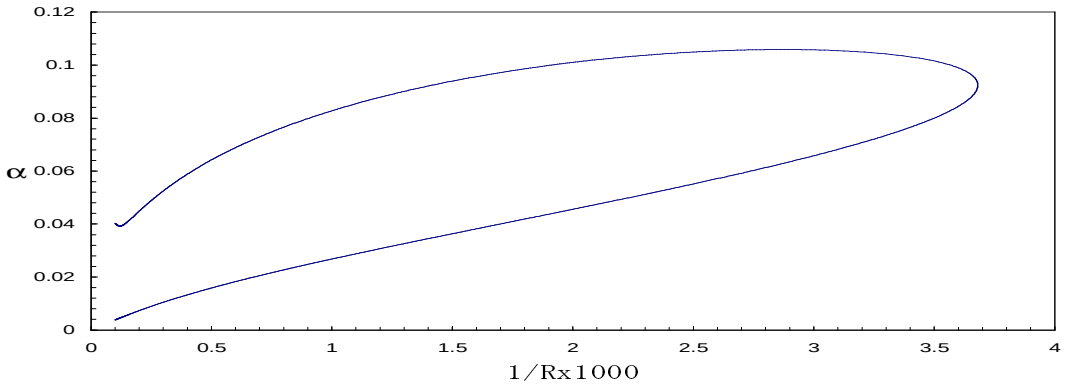

(a)

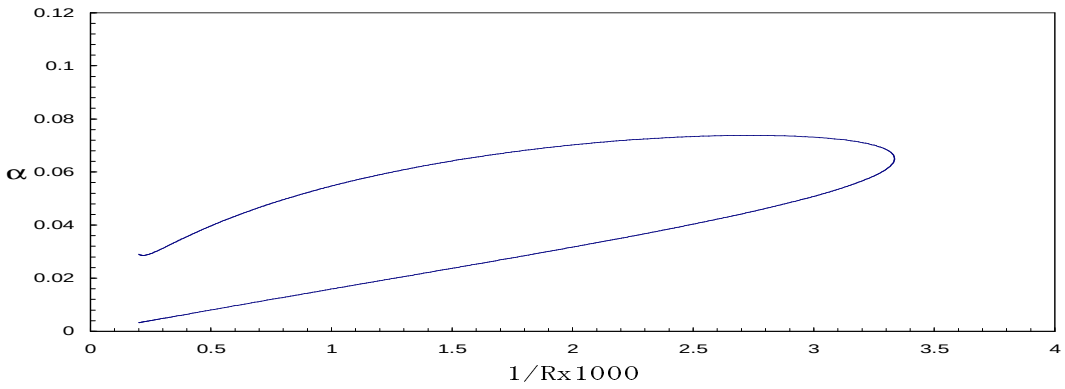

(b)

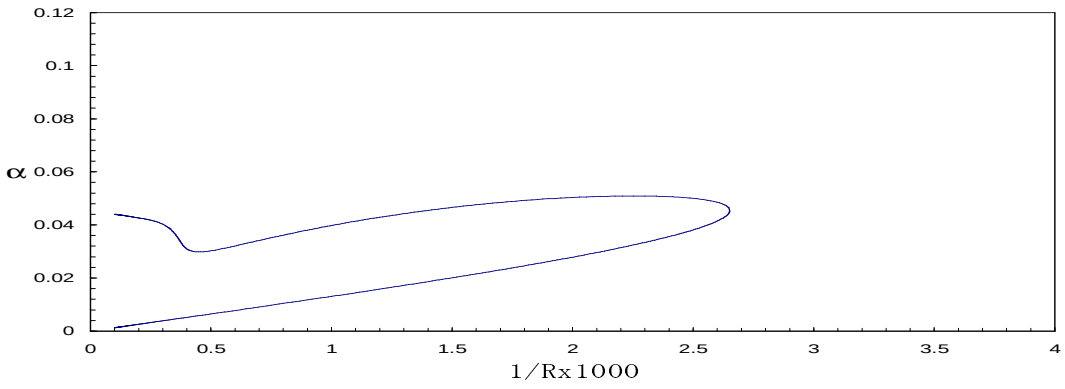

(c)

Figure 5.8 Neutral Stability curves for plane waves at **(a)** M=1.5, **(b)** M=2, and **(c)** M=2.5, illustrating the Mach number effect.

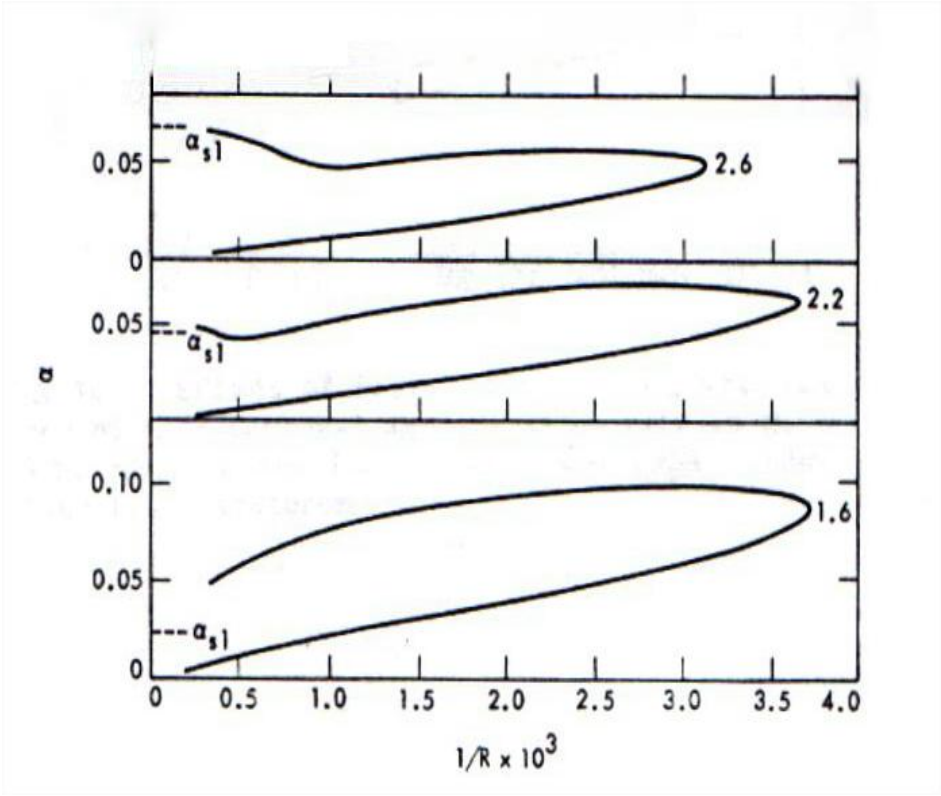

Figure 5.9 A study by Mack [11] displaying the effect of Mach number on 2D stability curves at wind-tunnel temperatures.

The first configuration in Figure 5.8 visualizing the stability curve for M=1.5 perfectly matches with the one plotted by Mack for M=1.6. Regarding same case, the compatibility of the minimum Reynolds number with the Mack's result is also well established. Comparing the next curve in the current figure plotted at M=2 with the configuration at M=2.2 in Figure 5.9, one can conclude with the same accordance in the shapes considering the differences in Mach values. Mack finds the peak point at nearly $R_{FS} \approx 280$ for that Mach number which is also acceptable when the currently obtained values at similar Mach numbers are to be considered.

However, in the last diagram of Figure 5.8 a small discrepancy occurs compared to the stability curve of Mack at M=2.6. He finds the peak point nearly at $R_{FS} \approx 320$ which is a little smaller than expected (see Table 5.2). This difference could be most probably due to the fact that Mack takes the Prandtl number in his calculations as a temperature dependent variable which is in fact, a constant in the current study (Chapter 2). Also, the reference temperature that he used as the wind-tunnel temperature, $50\ K$ is different from the currently used $T_e^* = 288K$ as well. Moreover, similar to Arnal's study [2], there are a couple of points that are not very clear, such as the mean flow energy equation and its contribution to the stability problem.

Proceeding further by increasing the Mach number on the plane wave analysis, one observes that the stability phenomenon for the boundary layer flow becomes much more exciting. From Figure 5.10 to Figure 5.13, constant temporal amplification curves each giving the variation of the wave number with the Reynolds number and their behavior upon the Mach number are illustrated including the hypersonic cases. Different from the previous diagrams yielding only one mode of instability, there exists now an additional mode, the *second mode*, which appears at higher wave numbers.

Before mentioning about this mode, one has to introduce a new parameter, *the relative Mach number*. It can be described as the flow Mach number in a reference frame moving at the velocity of an instability wave [16]. Its name was first used by Mack [11, 12] who is also the father of these additional modes. But, the classification of disturbances with the use of such a relative speed was earlier made by Lees and Lin [6]. According to their definition, a *two-dimensional* disturbance is *subsonic*, *sonic* or *supersonic* when

the x-component of its phase speed relative to the freestream velocity is less than, equal to, or greater than the local speed of sound. Accordingly, denoting the local Mach number by M, the relative Mach number is described by the following [2, 6]:

$$\breve{M} = M - \frac{c_r^*}{a^*} = \frac{U^* - c_r^*}{a^*}, \tag{5.1}$$

where, c_r^* is the dimensional form of phase speed defined as ω_r^*/α^* by the temporal amplification theory for the plane waves. The local speed of sound varying with the mean temperature distribution, is represented here by 'a^*'. This new parameter, $\breve{M}$ was formulated for oblique waves by Mack [11]. While rearranging the governing equations (Eqs. (2.49)) according to the inviscid instability theory corresponding to infinite Reynolds numbers, he referred to the following relation:

$$\breve{M} = \frac{(\alpha U + \beta W - \omega)M}{k\sqrt{T}}, \tag{5.2}$$

as the *relative Mach number* in the direction of the unstable waves, i.e., the direction of $\vec{k}$. By this definition, he succeeded in obtaining the oblique compressible form of the system arranged by Lees and Lin [6] for the plane flow. Note that, taking the wave number component β as zero, Eq. (5.2) turns into the nondimensional form of Eq. (5.1). In this manner, the disturbances are to be subsonic if this parameter is less than 1; sonic if it equals to 1 and supersonic if it is greater than 1 [2, 6, 11, 16].

Coming back to higher modes, their existence was first declared by Mack [11, 12]. From the numerical inviscid stability analysis about the compressible flat plate boundary layers, he obtained that as the relative flow (the flow with the relative Mach number) becomes supersonic over some portion of the boundary layer profile or, as the relative flow Mach number at the wall becomes supersonic while in the freestream it is subsonic, there occurs an infinite number of wave numbers corresponding to a single phase speed, c_r. This means an infinite number of neutral waves with zero amplification factor having the same phase speeds in spite of their different wave numbers. These additional wave numbers are therefore, called the *higher modes*. For the mathematical proof of this phenomenon, one can refer to [11].

The additional mode occurring first at M=4 in this study as shown in Figure 5.10, is known to be the first and the most unstable of these additional modes for a zero-pressure gradient boundary layer over a flat plate at high Mach numbers [12]. It was named as the *second mode* by Mack [11] calling the originally known mode, the viscous one, as the *first mode* or, the *TS mode*.

Physically, this second mode, also known as the *Mack mode* in literature, is the creation of a continuing reflection of acoustic waves in a relative supersonic region between the wall and the relative sonic line where $\breve{M}^2 = 1$ [11]. In adiabatic wall conditions, it is expected to be visualized after $M = 2.2$ [11], but since its first occurrence is at very large wave numbers compared to the first mode, it was not possible to display it in previous diagrams. However, as the Mach number increases this mode appears at

lower and lower wave numbers, i.e., two modes come closer so that at M=4, the second mode occurs in a range of α =0.-0.4 .

In Figure 5.10, the stability diagram at M=4 is represented with a few constant temporal amplification curves for both modes. The first observation would be the rapid variation of the amplification factors with the increasing Reynolds number in the acoustic mode compared to the viscous mode which yields higher maximum amplification rates for the second mode. However, the minimum Reynolds number for the instability is still achieved by the first mode at that Mach number although this will be accomplished by the second mode at higher flow speeds.

Figure 5.11 and Figure 5.12 are similar diagrams corresponding to M=5 and M=6, respectively. They illustrate the variations of amplification factors with the Mach number. The first mode shows a gradual increase in its highest value of amplification factors with the increase of Mach numbers. At Mach 4, the value of its highest amplification isoline is $c_i = 0.0035$ which is quite a big value as understood from its narrow shape starting at a large value of Reynolds number.

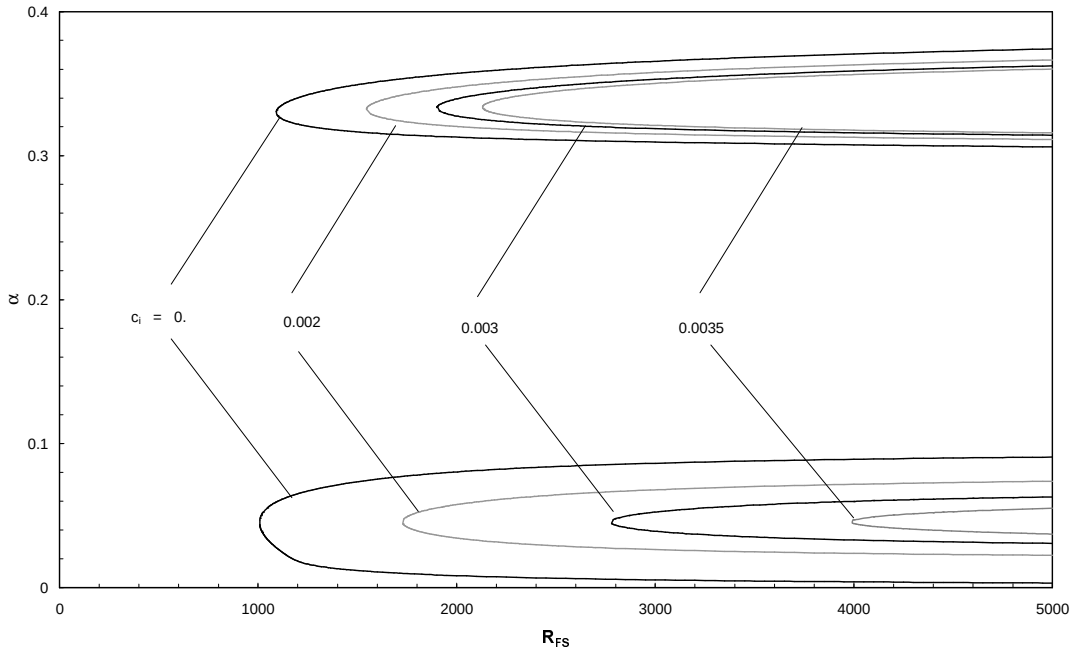

Figure 5.10 Constant temporal amplification curves for plane waves at M=4.

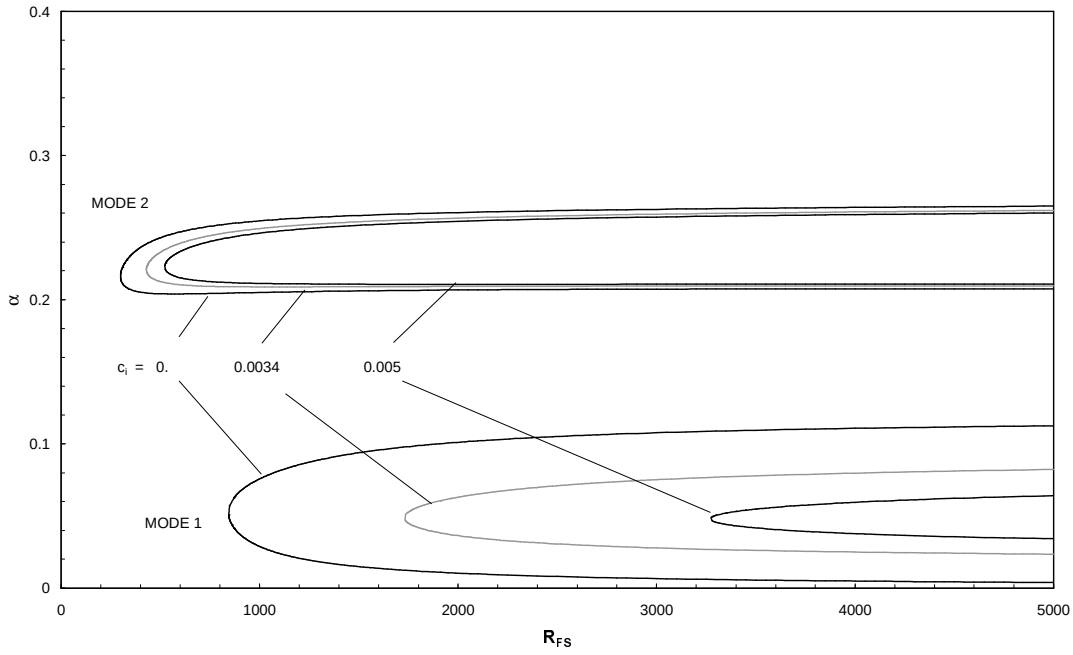

Figure 5.11 Constant temporal amplification curves for plane waves at M=5.

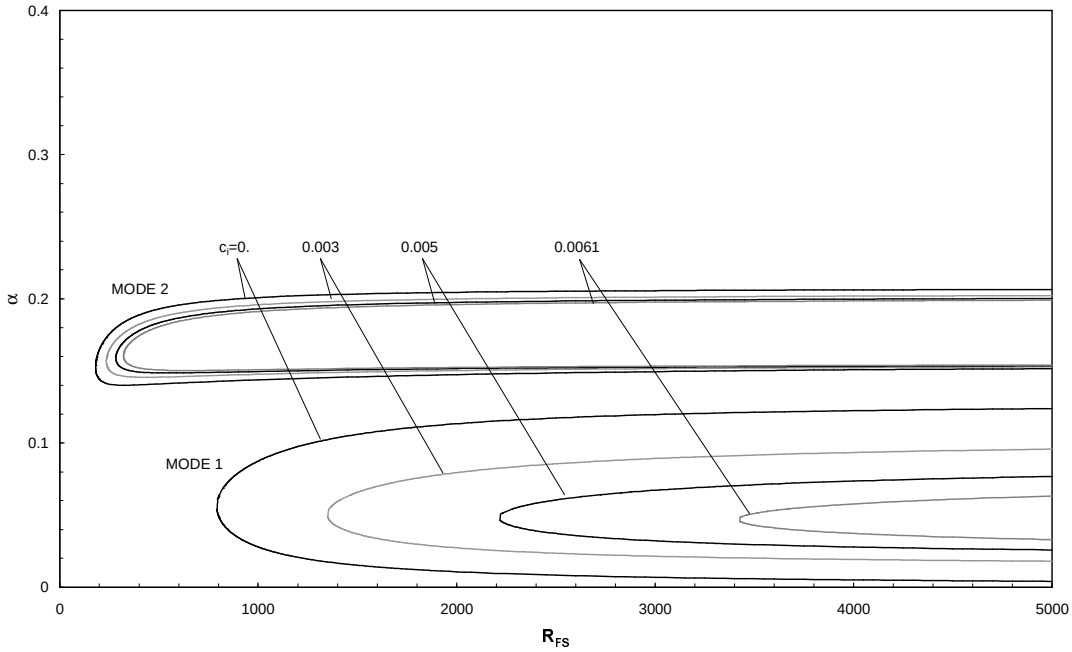

Figure 5.12 Constant temporal amplification curves for plane waves at M=6.

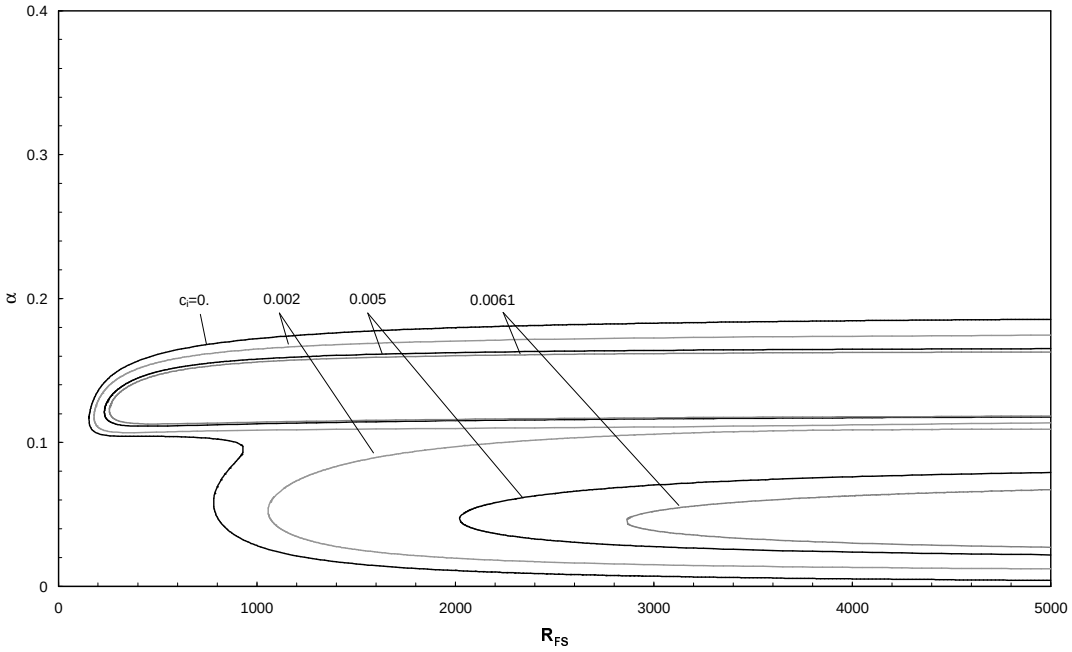

Figure 5.13 Constant temporal amplification curves for plane waves at M=7.

However, $c_i = 0.0035$ is not the highest amplification factor for M=5 as well as M=6. In addition, the minimum Reynolds number at which this mode starts occurring reduces to smaller values letting the higher amplification curves appear.

For the second mode, the observations are quite similar except for the rapid change in the shape of the amplification factors as well as the rapid increase in their numerical values between M=4 and M=5. The translation of the minimum Reynolds number for the instability from the first mode to the second happens at that point. At M=5 and M=6, the second mode has lower critical Reynolds number and hence, it is more unstable than the TS mode.

In Figure 5.13, another exciting phenomenon is illustrated such that the two unstable regions are joined. In this case, there is only one neutral curve with a large unstable region. Looking at the inner isolines, one can see that the existence of multiple solutions is still valid for the higher amplification factors.

As previously mentioned, the acoustic mode starts appearing at M=2.2 but with very large wave numbers compared to the first mode. As the Mach number increases, the second mode switches to lower and lower wave numbers such that at M=4, it is able to be visualized in a range compatible with the first mode. The effect of Mach number continues at higher flow speeds and these two modes come closer further until they join. This is better depicted in Figure 5.14 displaying only the neutral stability curves at the specified Mach numbers.

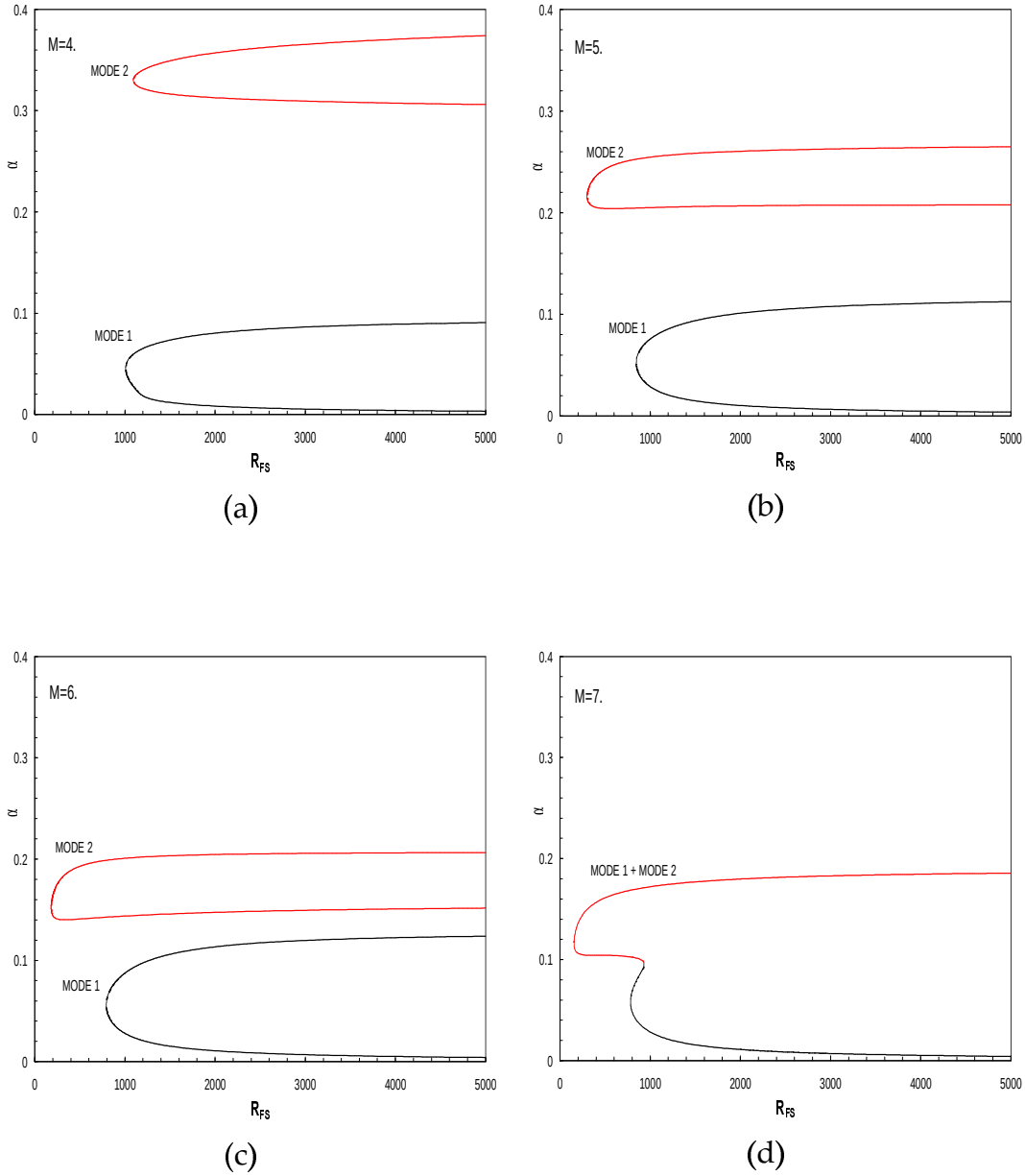

Figure 5.14 Neutral stability curves for plane waves at Mach numbers between M=4 and M=7.

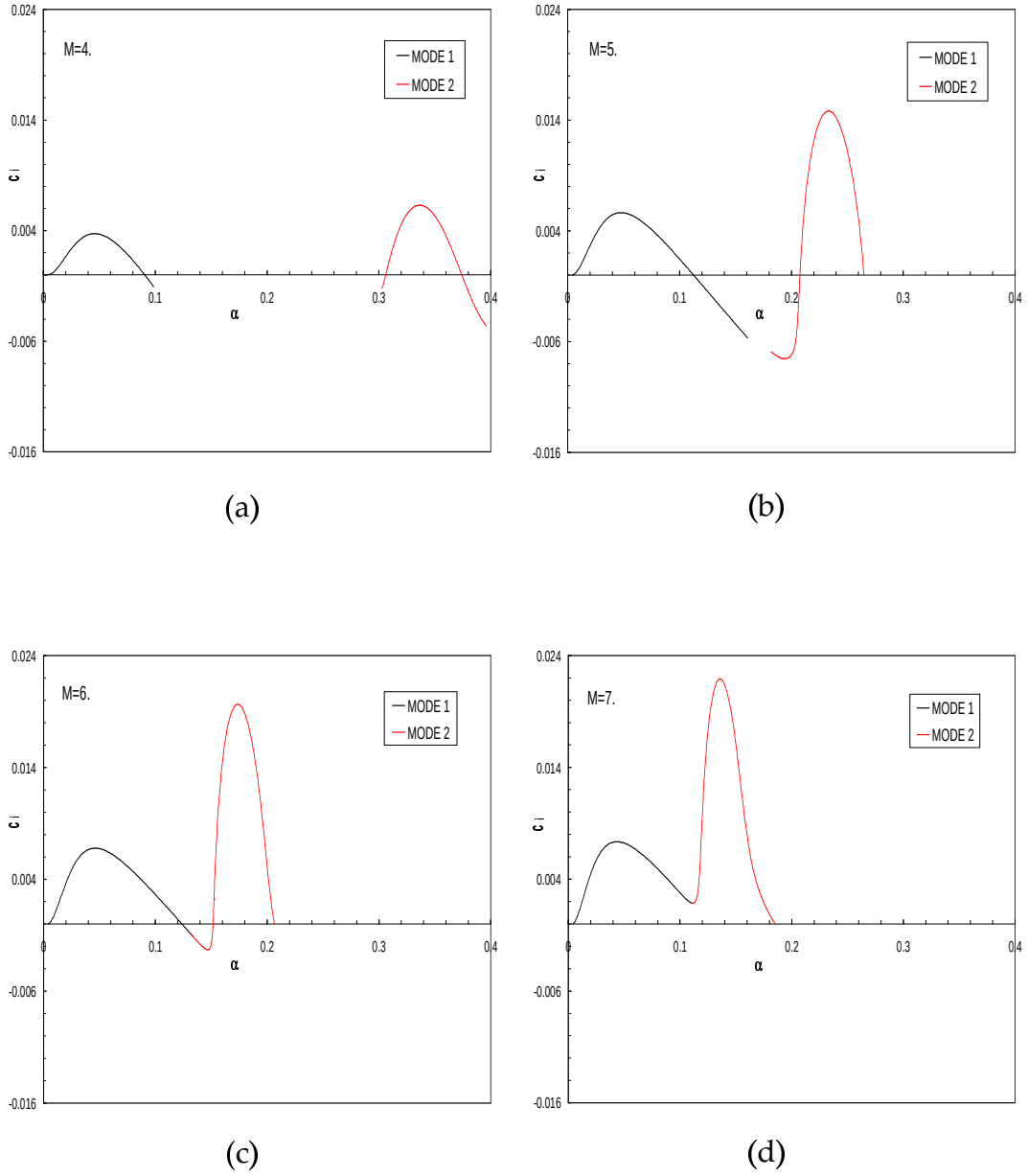

Figure 5.15 α-c_i curves for plane waves at Mach numbers between M=4 and M=7, at $R_{FS} = 5000$.

Figure 5.15 gives a different representation of this phenomenon. Each diagram in this figure shows the variation of amplification factor with the wave number at a specified Reynolds number, $R_{FS} = 5000$. As seen, in each diagram except for the curve at M=7 there are four points intersecting the $c_i = 0$ line. Here, one recognizes that the curves merge at M=6. This should not be confused with the joining of neutral stability curves demonstrated in Figure 5.14(d). In this case, the connection shows the minimum c_i value at which the second mode first appears. In this respect, at M=6 there is still a second mode of neutral stability curve. At M=7 whereas, this connection happens at positive c_i value meaning that the multiple solutions are obtained only in the unstable region corresponding to the positive amplification factors.

The variation of *highest* amplification factors with respect to the freestream Mach number for both modes at that Reynolds value is well depicted in Figure 5.15. The slight variation in the viscous mode is replaced by a considerably high increase in the acoustic mode most of which occurs between M=4 and M=5.

The final representation, Figure 5.16 gives the minimum Reynolds numbers for both first and the second modes at all investigated Mach numbers. At M=7, even though the modes join to form a single neutral stability curve, the figure shows two minimum Reynolds numbers as if they were separate. This is nothing but to yield a continuous identification of Mach number effect. Here, one observes much clearly that for the TS mode, the stabilizing effect of freestream Mach number occurring up to M=4 turns into a destabilizing influence after that point whereas, for the second mode,

one recognizes a continuous destabilizing effect. Figure 5.16 also points out the dominating instability of the second mode after M=4.

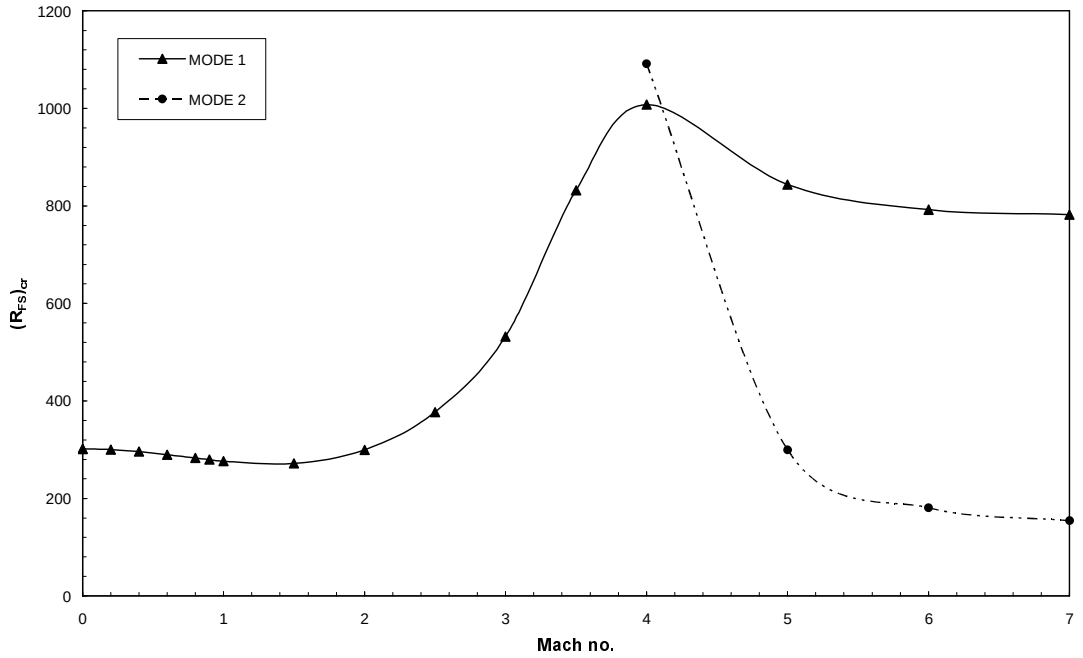

Figure 5.16 Effect of Mach number on critical Reynolds number of both TS and acoustic modes for plane waves, from M=0 to M=7.

The next step is the comparison of the current results with the ones belonging to similar studies in literature. Unfortunately, lack of existing data does not let all numerical results be compared and discussed. The investigations of Masad and Malik [14] present the curve of neutral stability in hypersonic adiabatic flow over a flat plate at M=8 and $T_e^* = 300K$ which is quite similar to what has been used in the current study. A qualitative comparison is hence possible with the current M=7 case represented in Figure 5.14 concluding with an excellent agreement.

An extensive analysis about this topic has only been performed by Arnal [2] and Mack [11]. Arnal's analysis, based on spatial amplification theory depicts the second mode first at M=4.5 and accordingly, it joins the first mode immediately at M=4.8. This means, the acoustic mode appears at lower wave numbers only in that Mach range which is in fact, not so meaningful. Actually, it would be too much to expect a perfect match with what Arnal had represented because of the reasons mentioned in previous paragraphs. One should bear in mind that, his current study gives only the formulation of two-dimensional incompressible stability problem in spite of the results reported for more complex cases, such as compressible flows with oblique waves. For this reason, it is not possible to comment on those illustrations.

Similar results were also obtained Mack [11]. His study gives a detailed problem solution based on the temporal amplification theory about the present case. In previous Chapter 2 and Chapter 3, it was declared that the current numerical analysis including the governing equations and the uniform mean flow solutions were in excellent agreement with Mack's analysis [11]. In latter steps of the solution procedure whereas, conflictions are observed leading to considerable differences in results. The points in confliction were mentioned in the related chapters but to remind, the first difference is about the Prandtl number which is treated as a temperature variable in calculations of Mack. In addition, the viscosity parameter which is related to temperature by Sutherland's formula, is obtained in a different way by Mack [11]. This also causes the coefficient of thermal conductivity to vary. Moreover, in his related calculations the reference temperature is taken as the wind-tunnel temperature, $T_e^* = 50K$ which is $T_e^* = 288K$ in the current

analysis. Above all, it is questionable how the energy equation of the mean flow had been included to the problem.

If one asked whether these reasons can create such differences at higher speeds, the answer would be *yes*. At supersonic and hypersonic speeds, the results are much dependent on the numerical values of these coefficients as well as the freestream temperature.

5.3 Three-dimensional Disturbance Case

What has been done up to now covers the investigations at zero wave angle. In this section, similar stability analysis will be performed for various wave angles at different Mach numbers so as to find the most unstable conditions (wave angles) for the disturbances at corresponding speeds. Because the mathematical formulations in this study were derived for the most general case like three-dimensional flows with three-dimensional disturbances, there is no need to undertake away additional effort except for applying different wave angles.

In previous chapters, the complexity of three-dimensionality in disturbances was highly felt not only through the algebraic formulations but also in theoretical applications. Here, it shows its complexity one more time. Although the current code is capable of solving the stability problem for oblique case, it exerts much effort compared to the previous case while converging the proper combinations of stability characteristics.

The effect of wave angle on instability is recognizable even at M=0, the incompressible case. Figure 5.17 shows the variation of neutral stability curve with respect to this parameter at that Mach number. The slight change seen in the curve indicates that the region of instability occurs at smaller α values as the inclusion of the normal component of the wave number increases. Moreover, the location at which the unstable disturbances first enter the boundary layer moves further downstream. One can refer to Figure 5.18 to see the change of related Reynolds number, i.e., R_{cr} with respect to three-dimensionality in disturbances better.

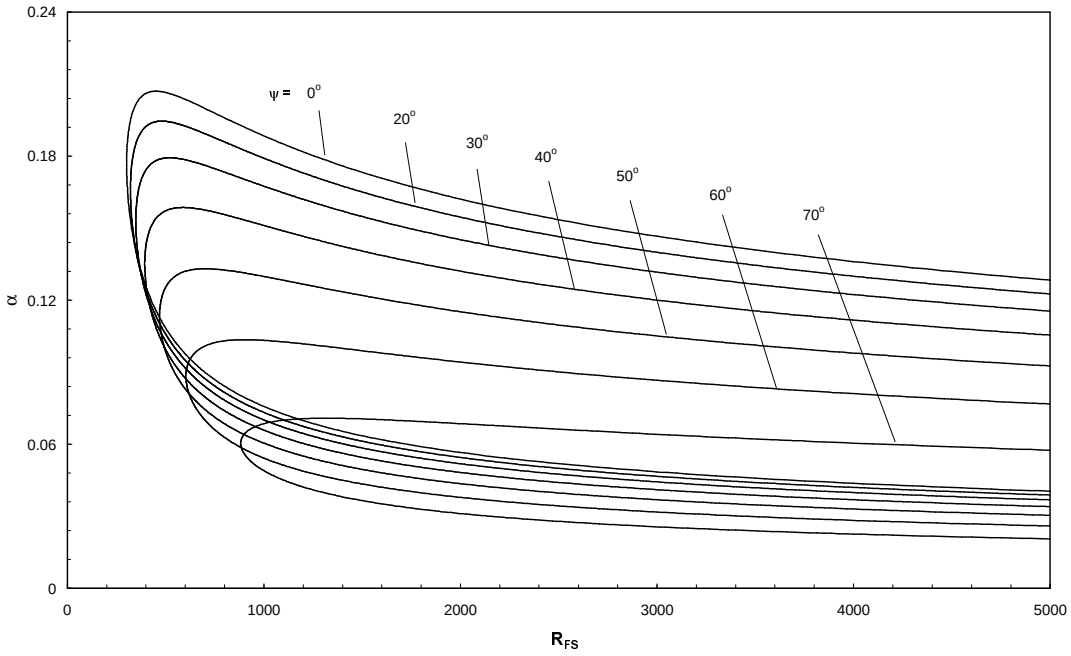

Figure 5.17 Neutral stability curves for oblique waves at M=0.

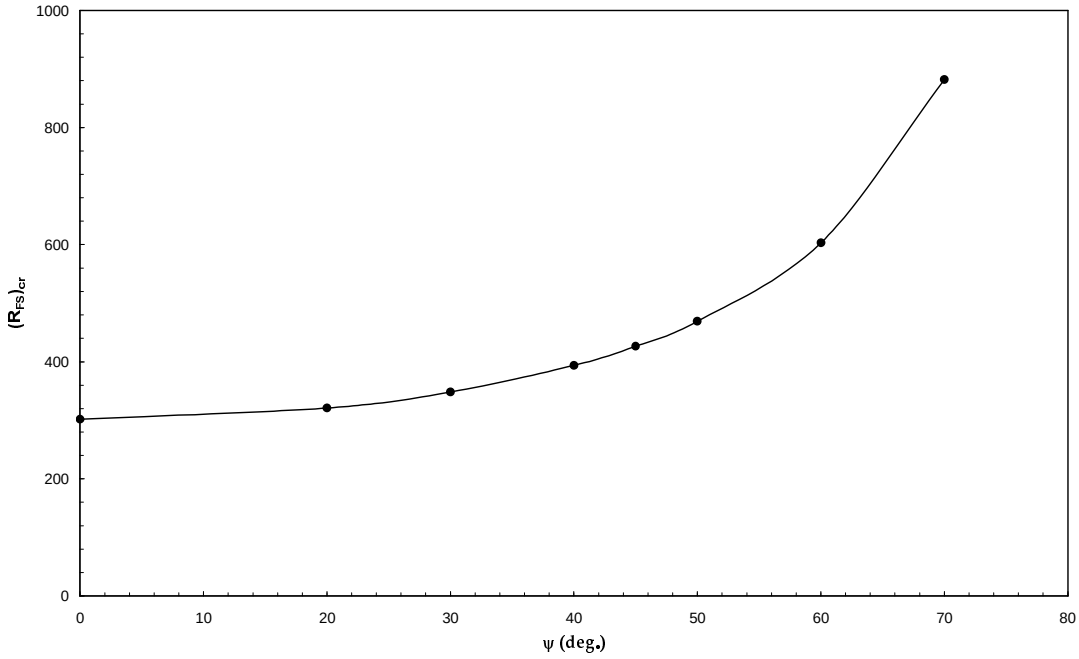

Figure 5.18 Effect of wave angle on critical Reynolds number at M=0.

It is clearly understood from the increasing attitude of the critical Reynolds in Figure 5.18 that at zero Mach, the most unstable waves are to be the ones with zero wave angle, i.e., the plane waves. This implies that the wave angle has a stabilizing effect on the current boundary layers which has been also declared by Squire in 1933 [10]. His theorem [12] regarding the stability of *2D incompressible* parallel boundary layer flows over flat plates, is based on the transformation of oblique wave formulation into a completely two-dimensional problem (2D flows with plane waves). This method is known as the *Squire's transformation* in literature concluding that two-dimensional disturbances are more unstable than three-dimensional disturbances for incompressible 2D flows. This is exactly what Figure 5.18 refers to.

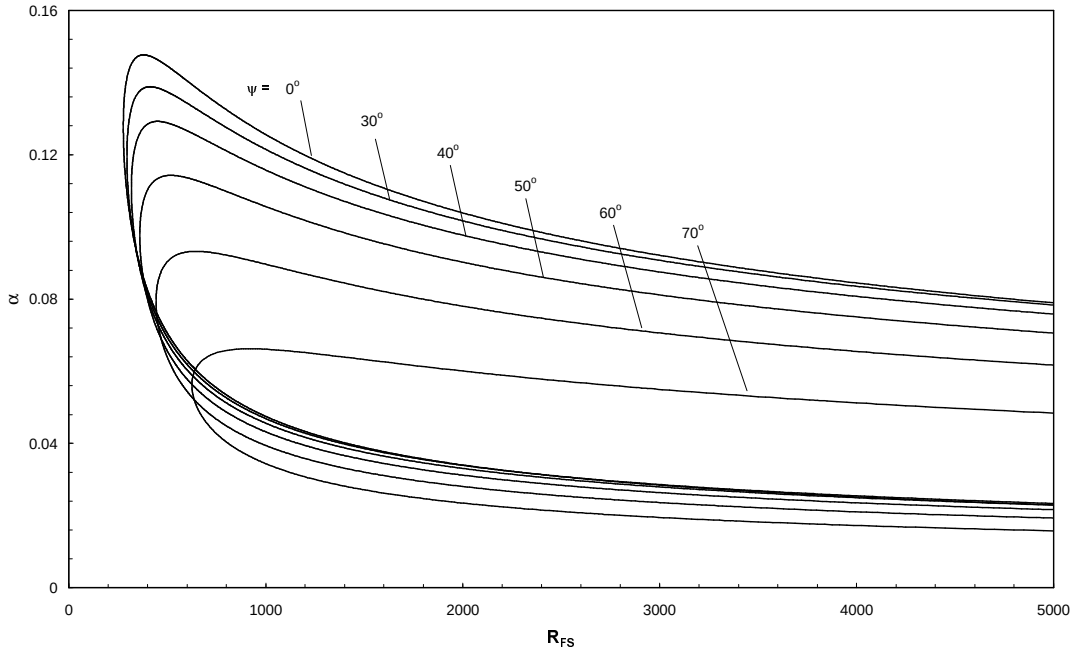

Figure 5.19 Neutral stability curves for oblique waves at M=1.

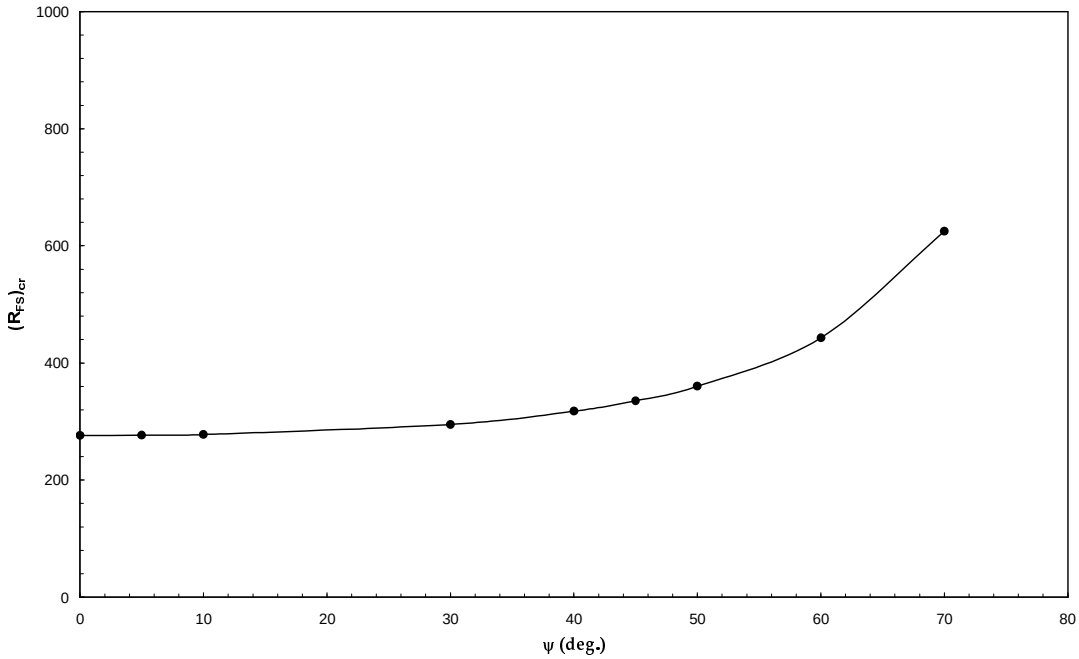

Figure 5.20 Effect of wave angle on critical Reynolds number at M=1.

A similar phenomenon is observed at a higher speed, M=1. In this case, the variation of the neutral stability curve shown in Figure 5.19 is again towards the smaller streamwise component of the wave number. Comparing with the previous case, one can say that here, a distinguishable degeneration in the curve starts at a wave angle, $\psi = 50^{\circ}$. The unstable region whereas, gets much narrower with the increase of wave angle. Besides, even though the occurrence of β causes the critical Reynolds number to increase in both Mach cases, its variation is more gradual now as seen in Figure 5.20.

With the increase of Mach number, three-dimensionality starts losing its pure stabilizing effect. This is clearly observed at a slightly higher speed, M=1.5. Figure 5.21 depicts the change in the curve of neutral stability at that Mach number. Accordingly, the corresponding curve appears at slightly larger α values as the wave angle increases up to 45°. In spite of its upper motion, the initial shape is conserved. However, as the wave angle increases further, its influence on the neutral curve starts differing such that α values at which the region of instability is identified now get smaller accompanied by shrinkage in the region. As seen in Figure 5.21(b), this time the shape of the curve is deformed in such a way that it tends to be parallel to the longitudinal axis much earlier. This implies that the inviscid theory starts dominating on the instability at smaller Reynolds numbers.

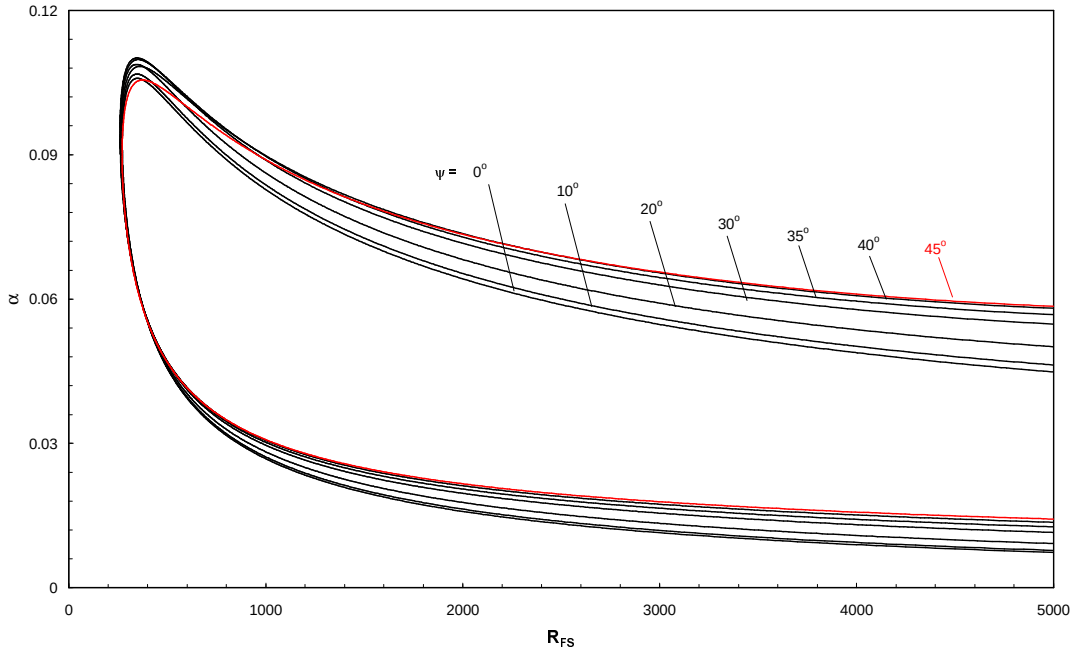

(a)

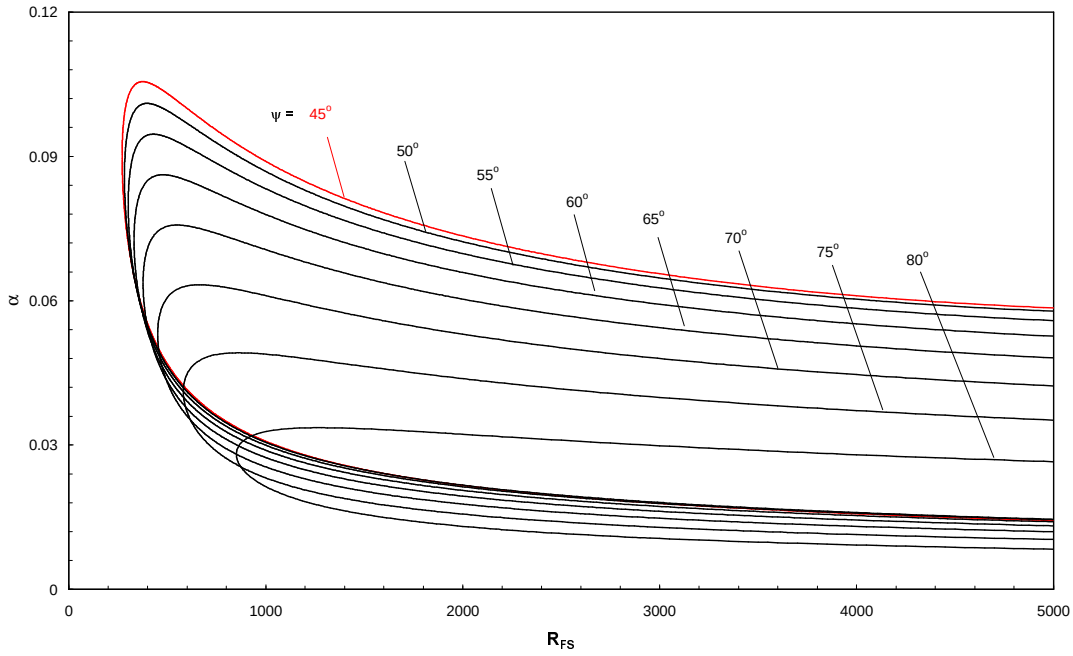

(b)

Figure 5.21 Neutral stability curves for oblique waves at M=1.5.

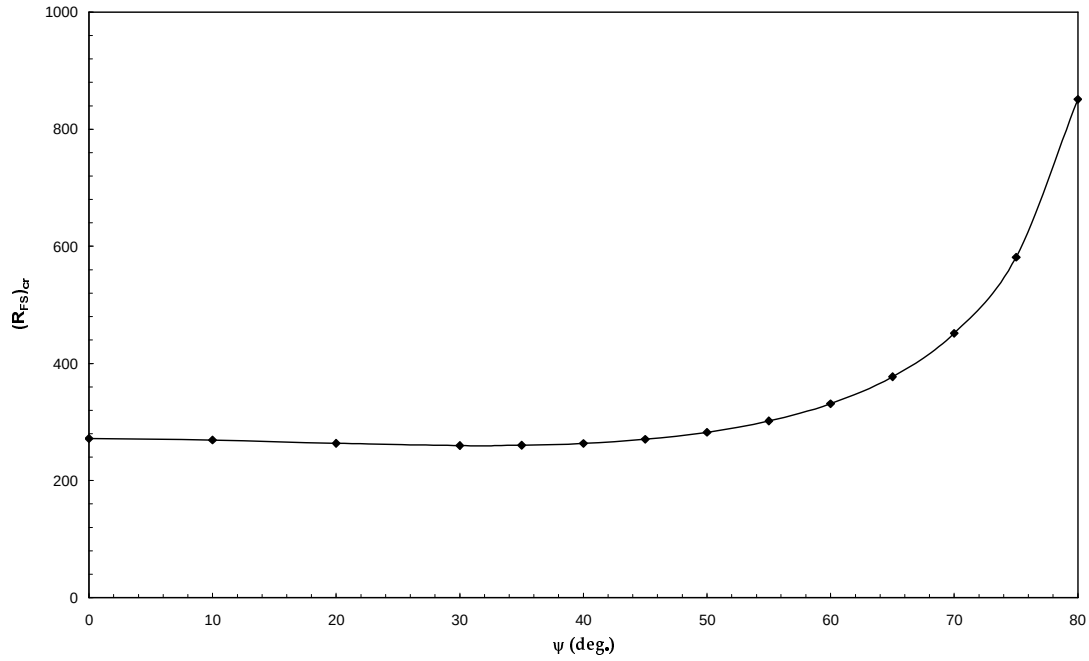

Figure 5.22 Effect of wave angle on critical Reynolds number at M=1.5.

Not only the shape of neutral stability curve, but also the minimum Reynolds number varies with three-dimensionality, as well. The curve illustrated in Figure 5.22 is nothing but a way of expressing the influence of wave angle on the critical Reynolds number. Opposite to previous cases, here it reaches to minimum at oblique cases with a slight difference from the plane waves. In this respect, the most unstable disturbances are the ones with $\psi = 30^{\circ}$. Afterwards, the wave angle continues its stabilizing effect.

At M=2, three-dimensionality effect on instability is perceived much strongly. Figure 5.23 clarifies that the curve surrounding the unstable region moves in the upper direction as the contribution of β increases. Here, different from the previous Mach number, its shape is deformed such that the unstable region is extremely enlarged with the increase of wave angle.

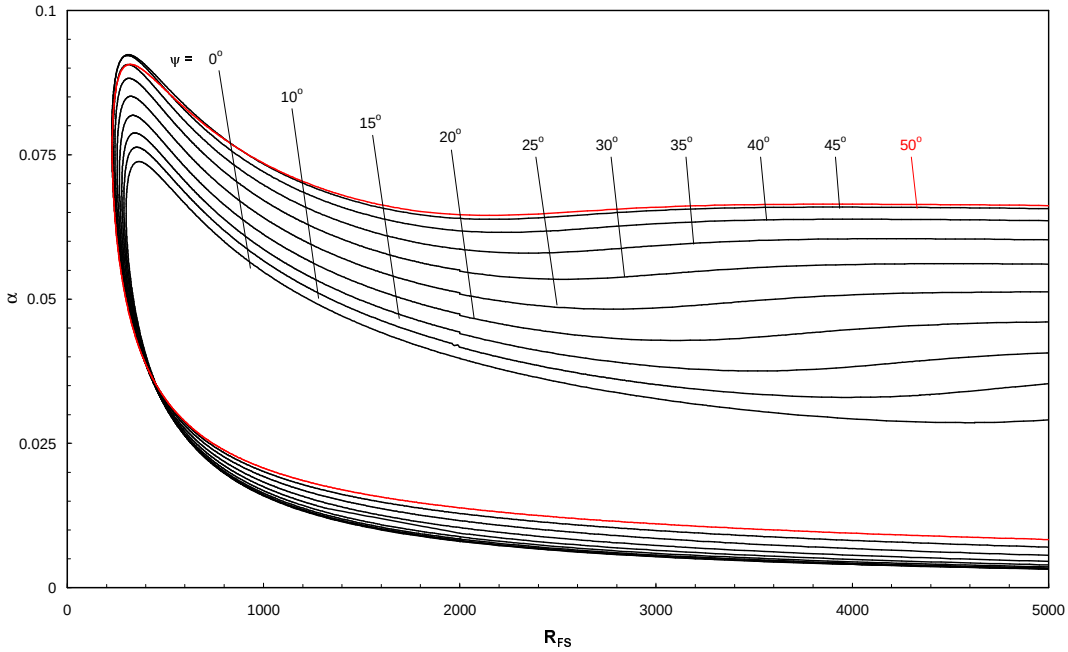

(a)

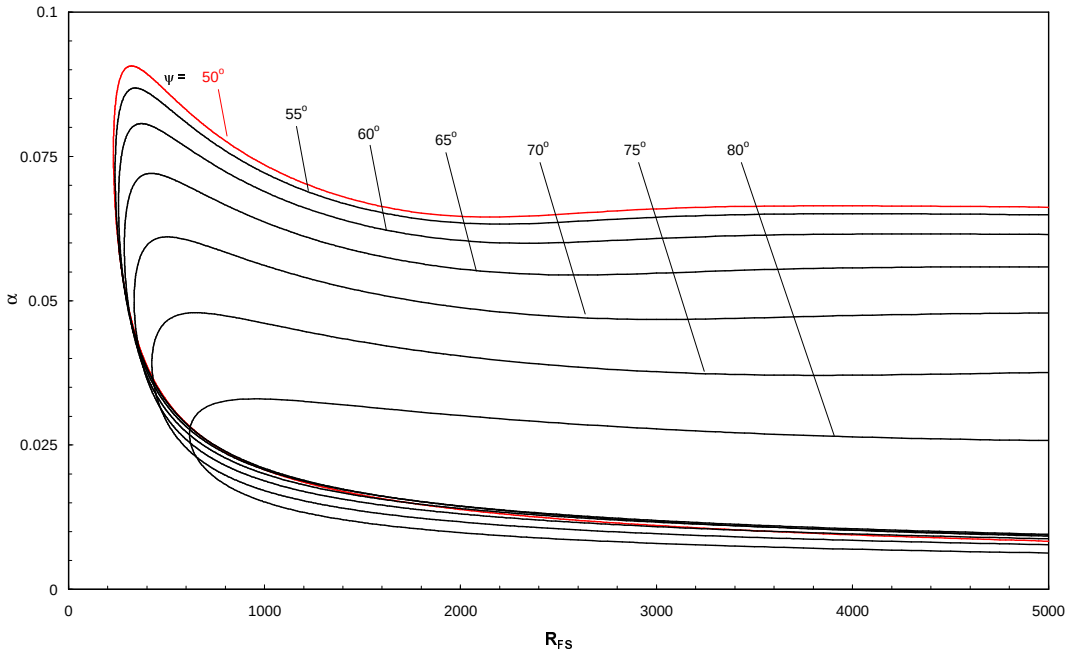

(b)

Figure 5.23 Neutral stability curves for oblique waves at M=2.

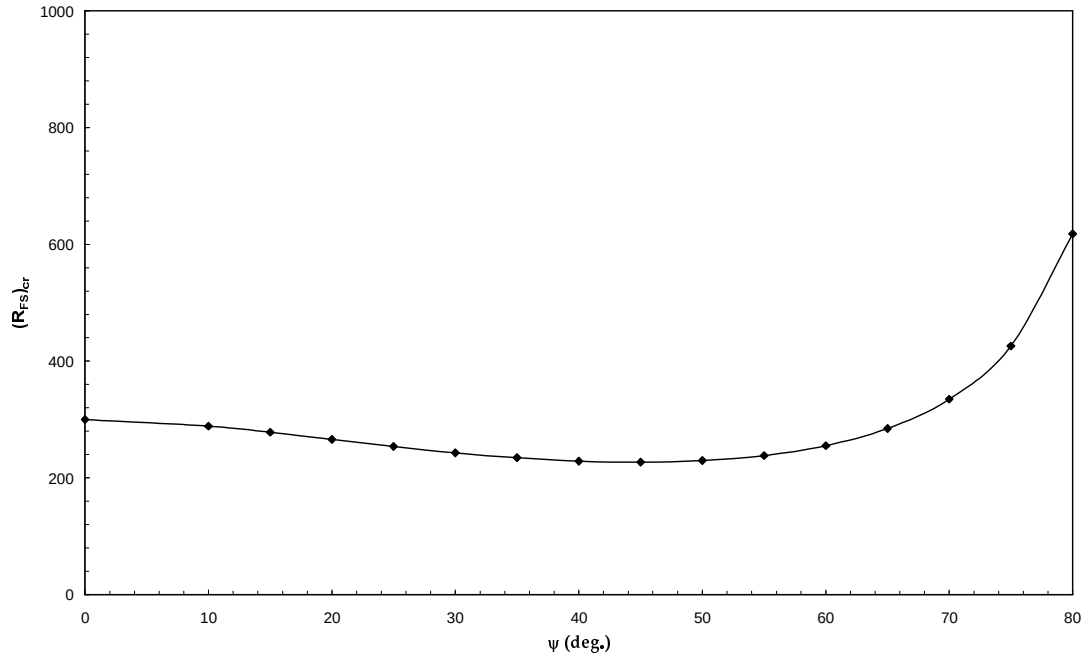

Figure 5.24 Effect of wave angle on critical Reynolds number at M=2.

However, these facts are observed up to $\psi = 50^{\circ}$. After that, the neutral stability curve starts moving downwards through the diagram with the tendency of being much parallel to x-axis and the change in the unstable region turns into a considerable narrowing as observed in Figure 5.23(a).

For the wave angle at which the disturbances are most unstable for M=2, one can refer to Figure 5.24. It well demonstrates that the location where the unstable disturbances are first introduced to boundary layer moves a bit upstream on the flat plate until $\psi = 45^{\circ}$, but after this value it starts shifting downstream. Different from Figure 5.22, the decrease in the critical Reynolds number is much considerable now. Besides, the inviscid instability starts dominating at much smaller Reynolds numbers. This is well identified in the first part of Figure 5.23.

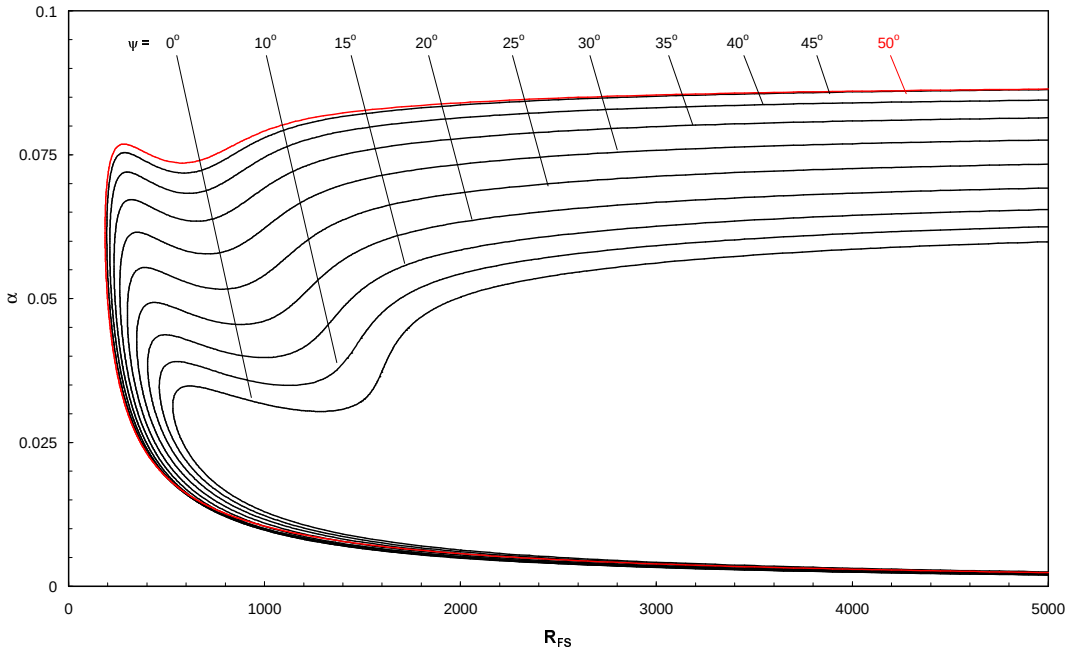

(a)

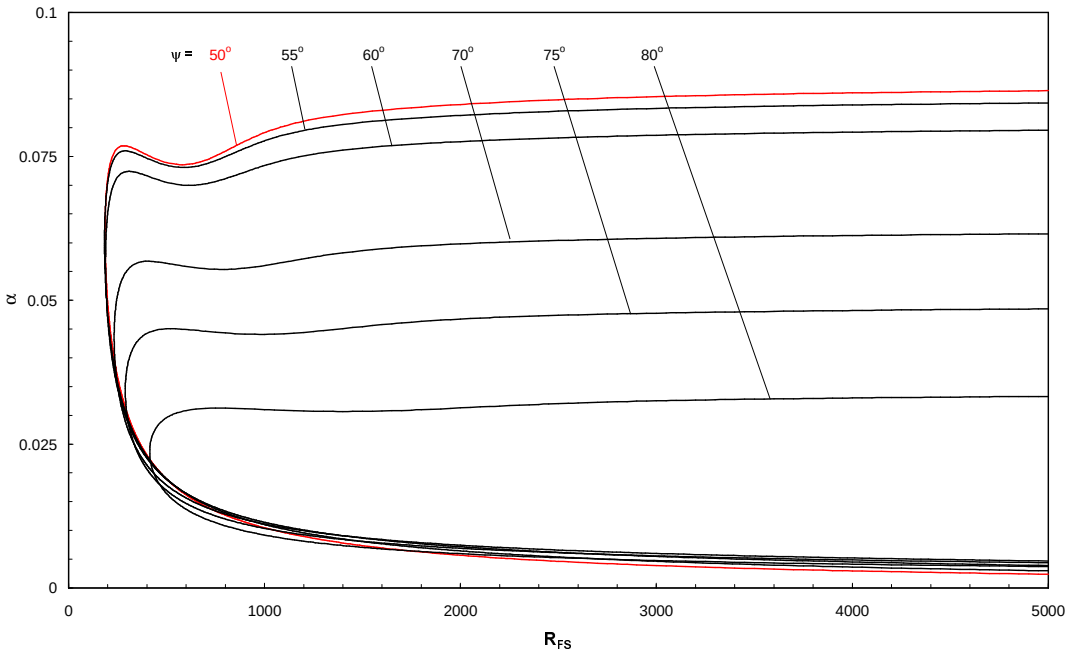

(b)

Figure 5.25 Neutral stability curves for oblique waves at M=3.

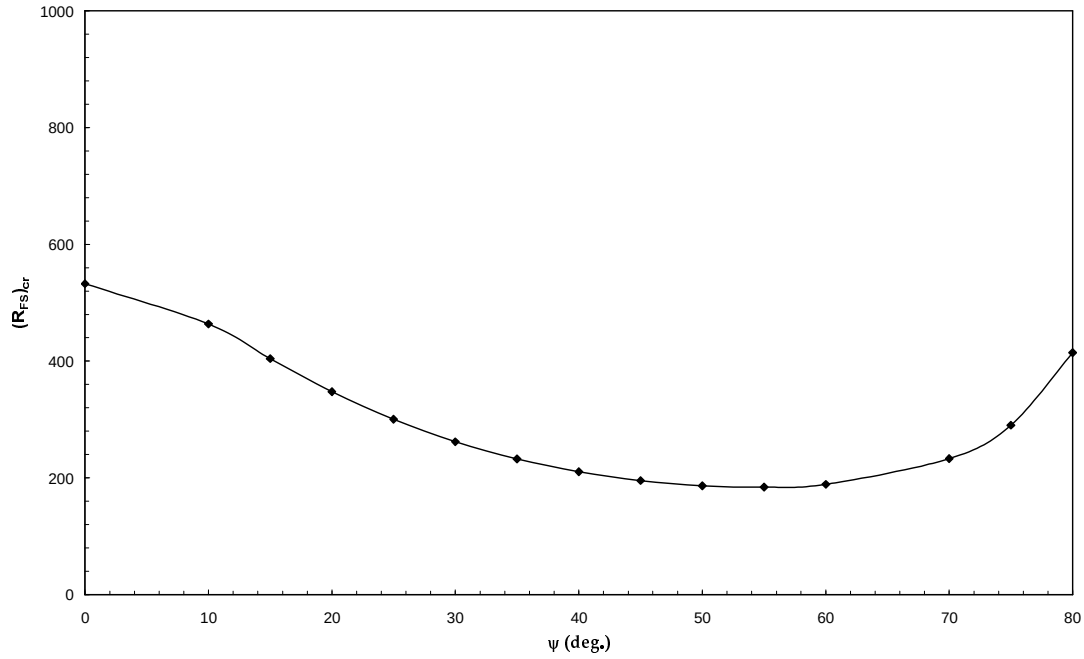

Figure 5.26 Effect of wave angle on critical Reynolds number at M=3.

What has been mentioned at M=2 is much distinctly visualized at M=3. With the effect of wave angle, the neutral stability curve starts appearing at larger and larger α values. Figure 5.25(a) depicts that in spite of a negligible deformation in its shape, the enlargement in the region where the disturbances are amplified is much more pronounced now compared to M=2. However, looking at the second diagram in Figure 5.25 corresponding to higher wave angles, one observes that the effect of wave angle starts differing after $\psi = 50^{\circ}$ such that, α values at which the neutral stability curve appears show a rapid decrease and the unstable region narrows down opposite to previous smaller wave angles. Moreover, the curve gets parallel to the x-axis much earlier.

As clarified in the previous section, the inflectional instability becomes more and more important at higher speeds. In this case, one can conclude that this effect is enhanced by the wave orientation as well. This is clearly identified by the curves in Figure 5.25(b) for the angles higher than 55° which are getting almost totally parallel to R_{FS}-axis. This angle is also the one at which the disturbances are most unstable. Figure 5.26 gives the decrease in critical Reynolds number up to 55° followed by a rapid increase. Needless to say, the decrease in critical Reynolds number is now much distinguishable compared to lower Mach numbers.

It was recognized earlier while investigating the plane wave case that the stability analysis becomes much more exciting at Mach 4 with the introduction of an additional mode, the *second mode*. The reason why it appears was clarified in the previous section. Here, Figure 5.27 illustrates the variation of this mode with the wave angle in addition to the variation of the viscous mode. The first mode shows similar reactions with the previous case at M=3. Accordingly, it initially enlarges but now showing a considerable deformation in the neutral stability curve which is accompanied by the greater increase in the *maximum* α values at which the mode appears. This behavior is valid up to $\psi = 45^{\circ}$. What happens at higher angles is that, these *maximum* α values decrease faster than the minimum values. Consequently, the unstable region narrows down with a considerable amount as seen in Figure 5.27(b).

For the same Mach case, different from the viscous mode, the effect of wave angle on the second mode follows a much simpler path such that with increase of β contribution, the corresponding unstable region directly gets

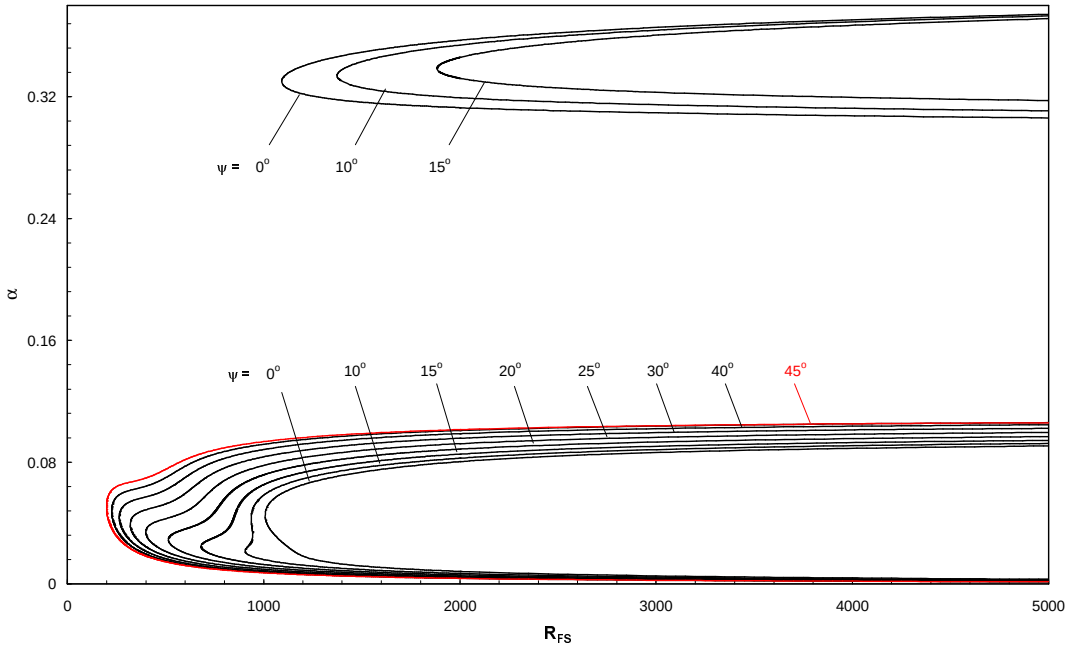

(a)

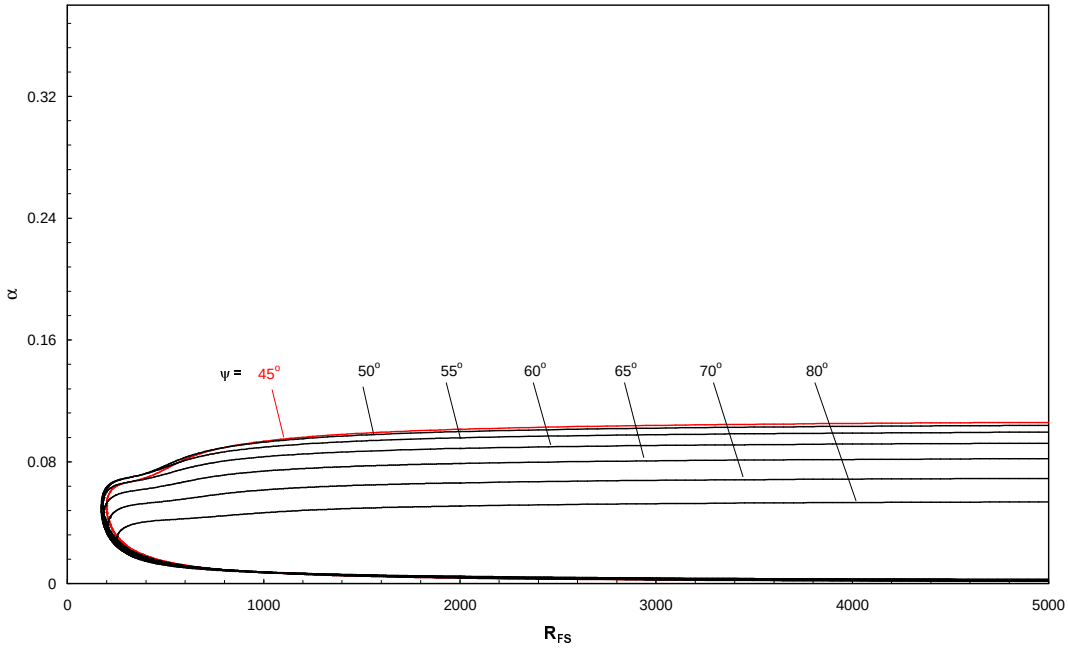

(b)

Figure 5.27 Neutral stability curves for oblique waves at M=4.

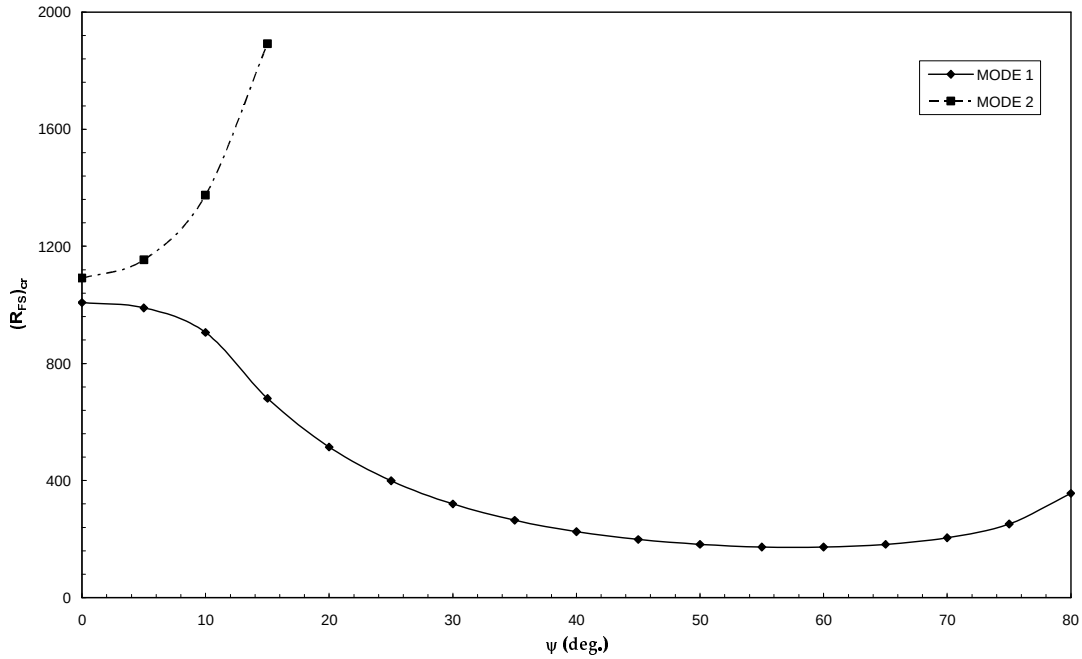

Figure 4.28 Effect of wave angle on critical Reynolds number at M=4.

smaller without a significant change in its maximum α values. This rapid decrease ends up with the disappearance of the mode at $\psi = 15^{\circ}$. This is why it is observable only in the first diagram of Figure 5.27.

At the current speed, the critical Reynolds number of the first mode also shows variation similar to previous cases as well but this time it is minimized at an angle of 60°. Figure 4.28 clearly depicts the decrease in Reynolds number up to its minimum. Even though the same decrease is observed previously, here it is much greater.

The same figure signifies the effect of critical Reynolds number with the wave orientation for also the second mode. In this manner, the most unstable direction seems to be the zero angle, i.e., two-dimensional case. It

shows nothing but the stabilizing effect of the wave angle on the acoustic mode leading to its disappearance.

These current observations about the first and the second modes are also supported by the studies of Mack [11] with the following words, "3D first-mode waves are indeed more unstable than 2D waves and second mode 3D waves are more stable than the corresponding 2D waves." Even though these words are related to M=4.5, the case at which the acoustic modes were claimed to be initially observed by Mack [11], this is a valid argument for M=4 here because this is where the acoustic modes are first observed in the present study.

Considering a slightly higher speed, M=4.5, the effect of wave orientation on the neutral stability curve for both first and the second modes is pretty much similar to the case of M=4 as indicated in Figure 5.29. One difference is that the enlargement in the unstable region of the first mode continues up to a little smaller angle, $\psi = 40^{\circ}$ following the increase in the upper limit of α values. At higher wave angles, the trend gets opposite such that the region where the disturbances are amplified gets narrower and narrower. The second mode on the other hand, shrinks as the effect of β increases. Here, it again differs from the previous case, M=4 by the existence of the acoustic mode up to a slightly larger angle, $\psi = 25^{\circ}$. This is also the reason why it is not visualized in Figure 5.29(b).

The next figure, Figure 5.30 points out the most unstable condition for both modes at M=4.5. Accordingly, this is $\psi = 60^{\circ}$ for the first mode, whereas it is $\psi = 0^{\circ}$, the plane wave condition, for the second mode. They are actually

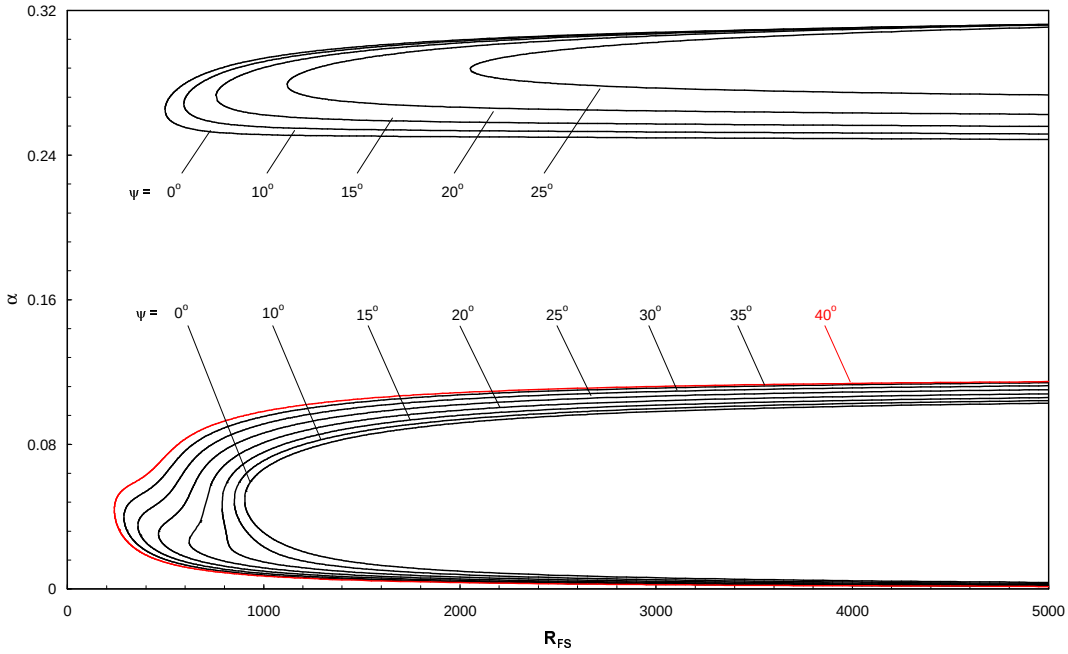

(a)

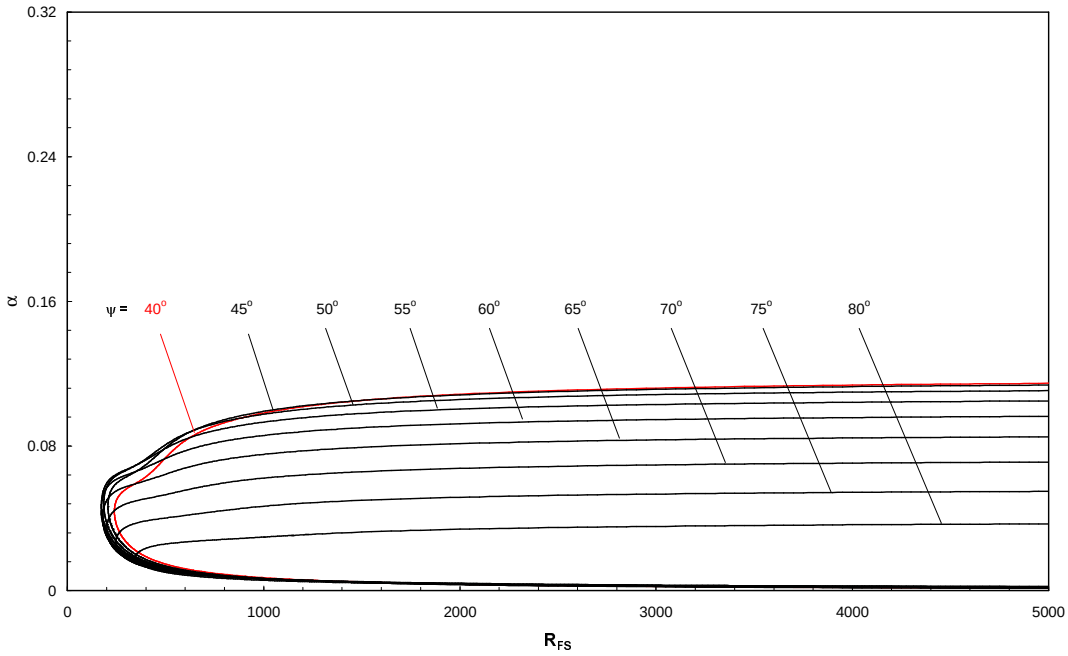

(b)

Figure 5.29 Neutral stability curves for oblique waves at M=4.5.

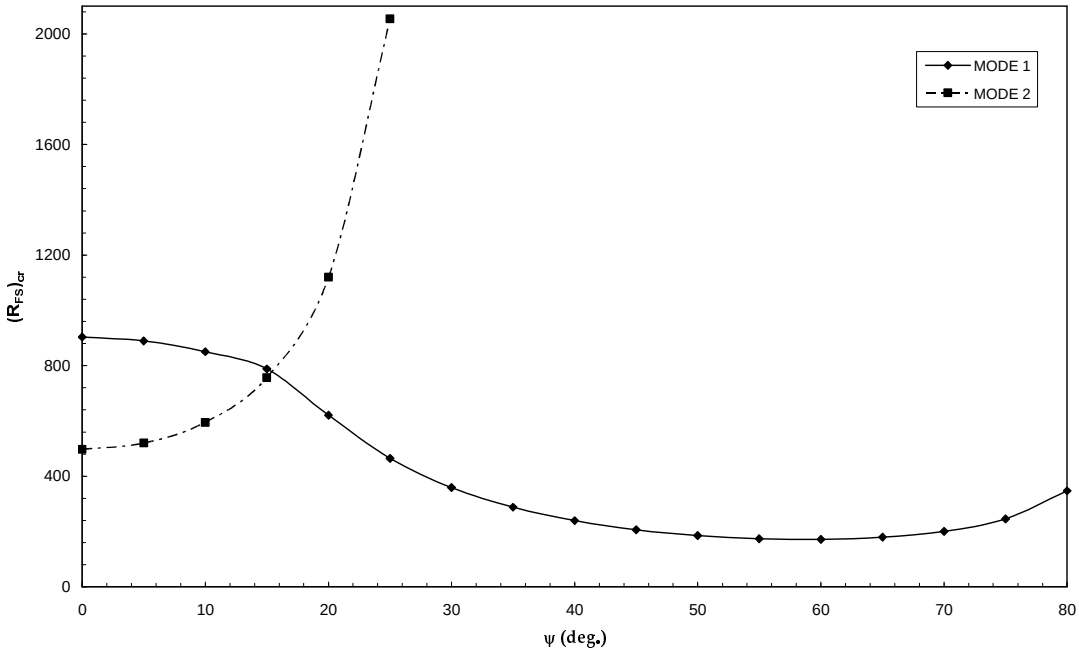

Figure 5.30 Effect of wave angle on critical Reynolds number at M=4.5.

the same with the directions reaching the minimum critical Reynolds numbers at M=4.

The last case studied in this section is the boundary layer flow at M=5. As denoted in Figure 5.31, the appearance of the second mode lasts until $\psi = 30^{\circ}$ which is a greater value compared to the previous two cases where this mode is observable. What happens to first mode is quite similar to those at M=4 and M=4.5. In this case, the unstable region enlarges up to $\psi = 40^{\circ}$.

The variations in the critical Reynolds numbers for both modes quite resemble the case of M=4.5. In Figure 5.32, it is well indicated that the most unstable waves are in the direction of $\psi = 60^{\circ}$ for the first mode. For the acoustic mode whereas, 2D case is still the most unstable one.

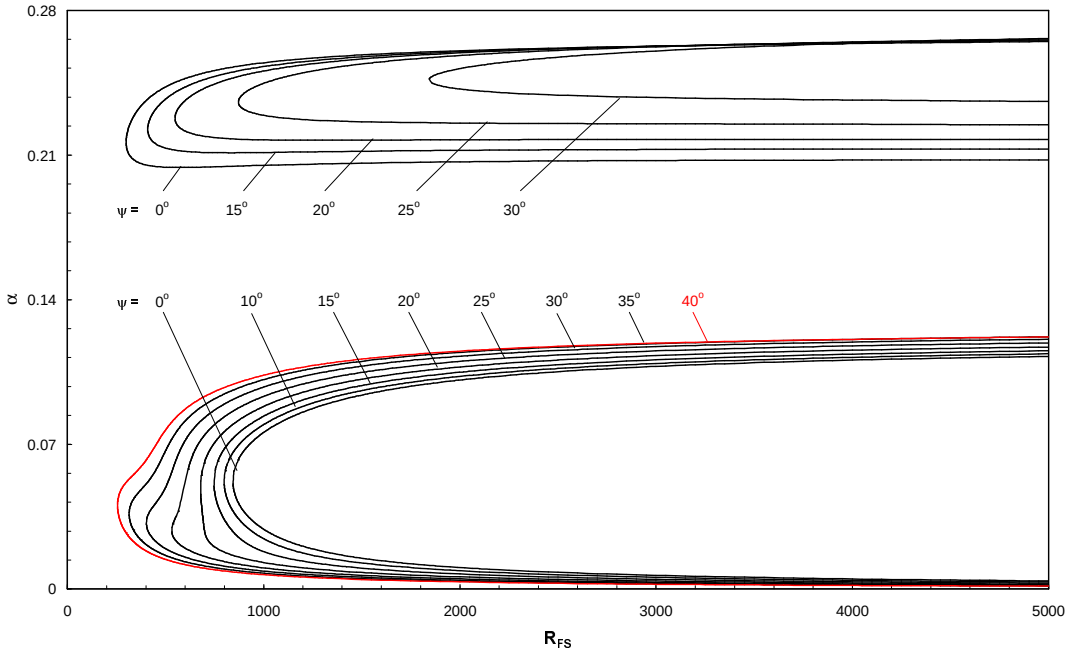

(a)

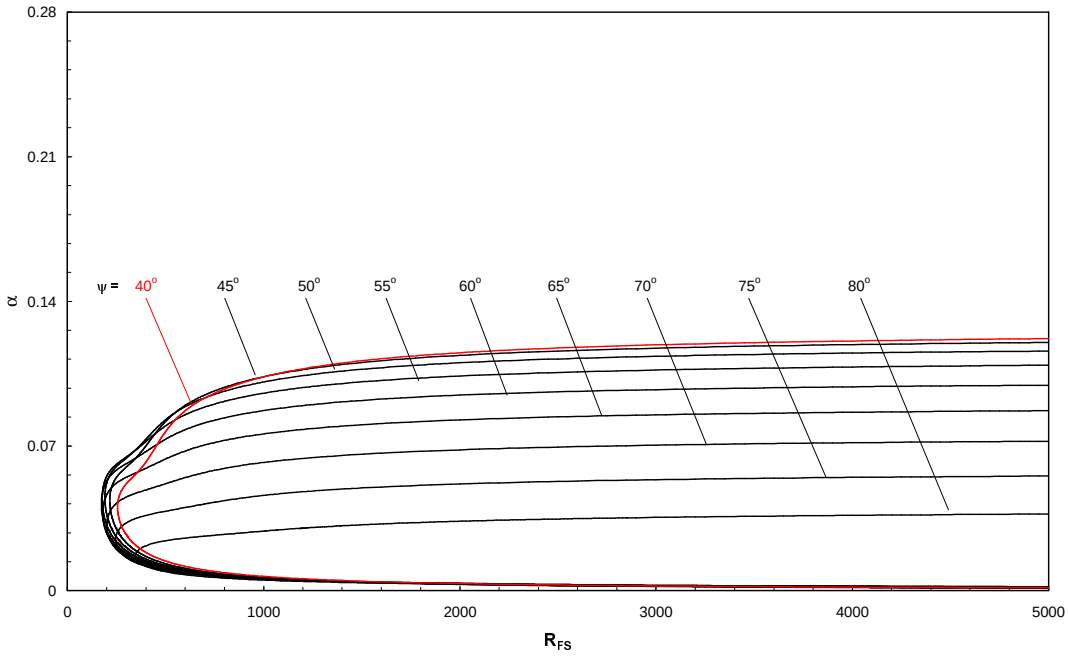

(b)

Figure 5.31 Neutral stability curves for oblique waves at M=5.

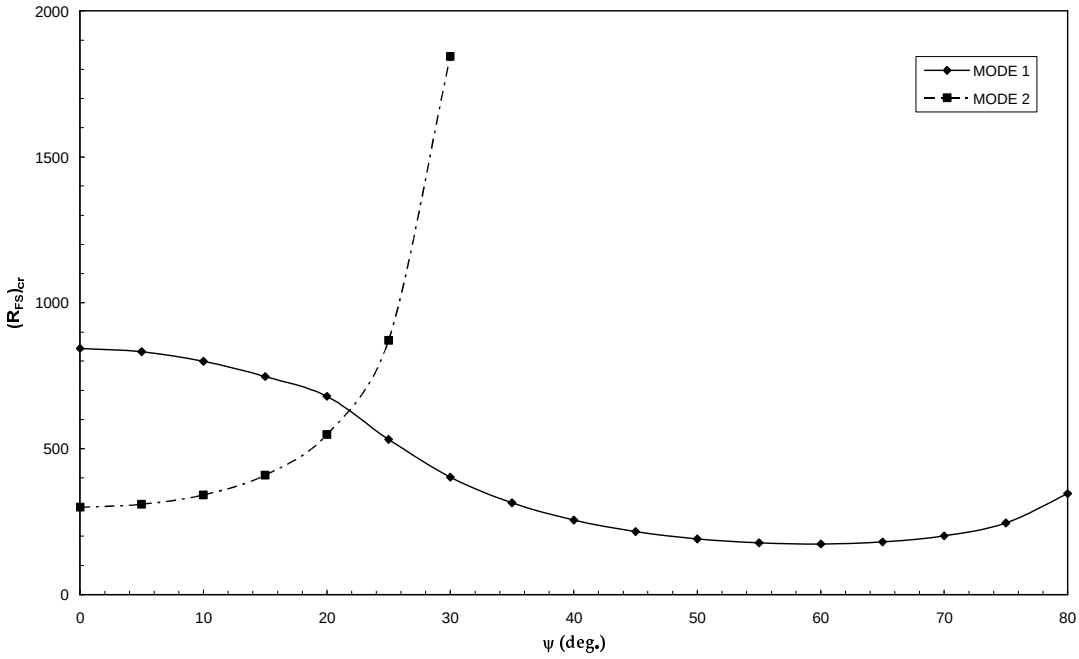

Figure 5.32 Effect of wave angle on critical Reynolds number at M=5.

Eventually, the points at which the most unstable disturbances first enter the boundary layer for the investigated speeds are summarized in Figure 5.33. The angles displayed in this figure indicate the directions of the most unstable waves at each Mach number. In this respect, one can better realize that 2D disturbances are always more unstable than the 3D disturbances for the *second* modes. The same is also declared by Arnal [2] and Masad [14] as well as Mack [11]. They further claim that, "the most unstable *first-mode* disturbance is always oblique at all supersonic Mach numbers". This is nothing but one of the consequences obtained by the present analysis and visualized in Figure 5.33.

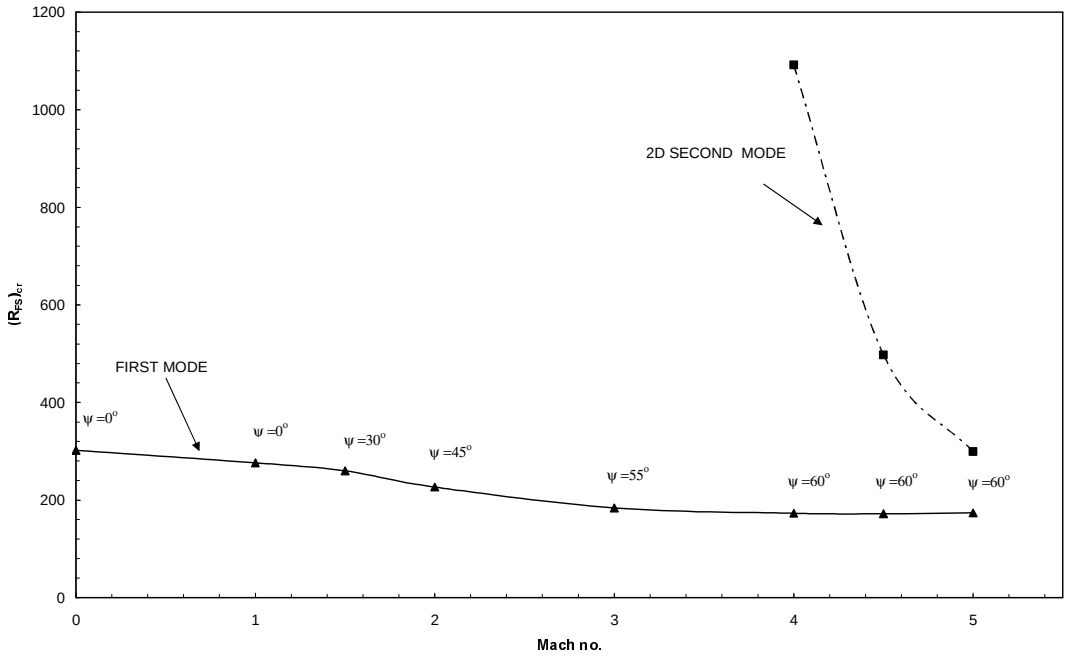

Figure 5.33 Effect of Mach number on critical Reynolds numbers in the most unstable directions.

Beyond all, Figure 5.33 essentially demonstrates the Mach number effect on the critical Reynolds number. Accordingly, for the first mode, the critical Reynolds number shows gradual decrease which points out the destabilizing effect. For the second mode whereas, the destabilizing effect is much apparent. In literature, unfortunately such a detailed investigation about the critical Reynolds number concerning the various wave angles at several Mach numbers does not exist. However, the next section including the transition prediction analysis based on the most unstable conditions, i.e., based on the results of the current section, will give an opportunity for an indirect comparison with previous studies.

Up to now, the effect of three-dimensionality has been investigated for only the neutral stability curves and the critical Reynolds number. What happens to growth rates with the wave orientation is the last question to be answered in this section. In this manner, Figure 5.34, Figure 5.35 and Figure 5.36 display the constant temporal amplification isolines for both the plane waves and the most unstable oblique waves at M=3, M=4 and M=4.5, respectively. With these figures, one can conclude that the amplification of the most unstable disturbances is much larger compared to 2D disturbances.

Arnal [2] identifies the most unstable wave in his studies by searching for the maximum growth rate and its corresponding direction in order to handle the transition prediction in this most unstable condition. According to his proposal, the most unstable direction is to be the one having maximum growth rate. Considering the definition of the growth rate and its relation with the amplification factors yielding a direct proportionality, this argument is indeed, in great agreement with what is revealed by these figures.

Unfortunately, there is neither experimental nor theoretical data about constant temporal amplification isolines denoting the variation of α with Reynolds number at present oblique conditions. The only exception is M=4.5 case studied by Arnal [2]. He accordingly demonstrates the similar configurations for the adiabatic flat plate boundary layer at that Mach number in order to show the effect of wave orientation on the amplification rate. In his related diagrams comparing the $\psi = 0^\circ$ with $\psi = 60^\circ$ which is the most unstable angle he obtained, one can easily observe that in the first mode the amplification factors increase in magnitude whereas, the second mode disappears completely at $\psi = 60^\circ$. All these are in perfect agreement with the

current results expressed in Figure 5.36.

Bear in mind that the present results are based on temporal theory however, Arnal [2] uses the spatial theory throughout his analysis. Besides, he gives results in terms of displacement thickness. For these reasons, one should not expect for both cases to match in a numerical point of view.

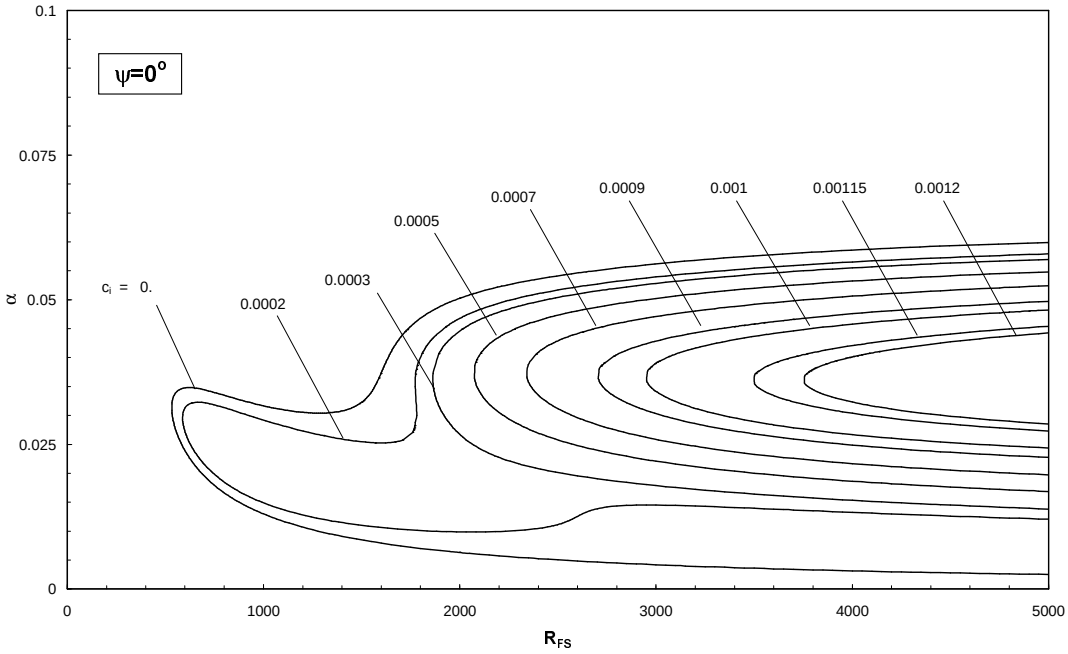

(a)

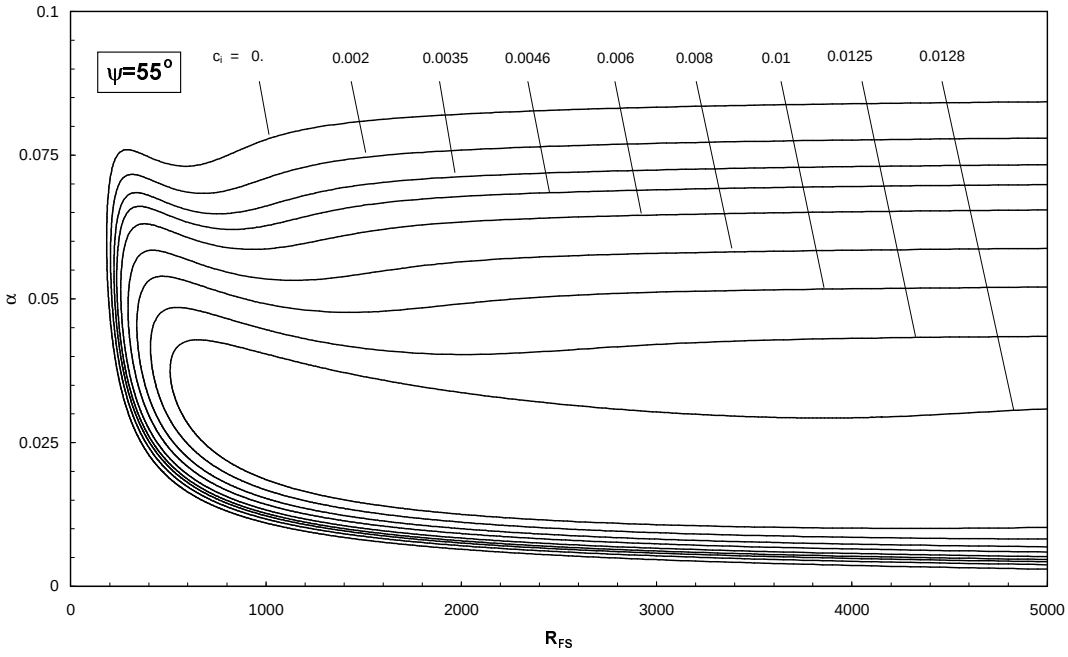

(b)

Figure 5.34 Constant temporal amplification curves for **(a)** the plane waves and **(b)** the most unstable oblique waves at M=3.

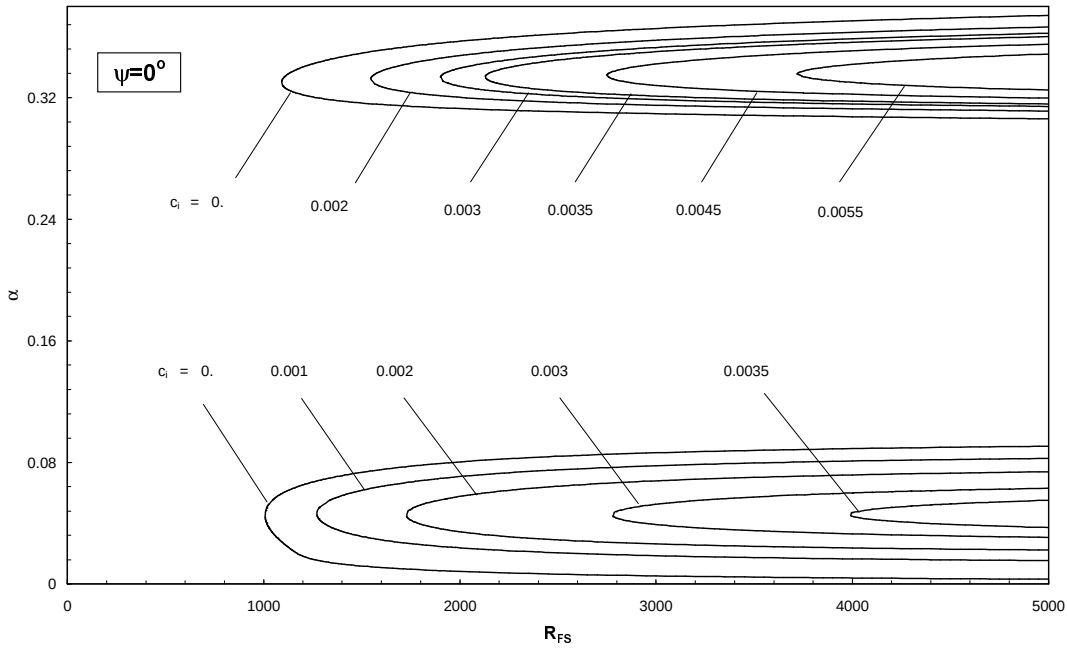

(a)

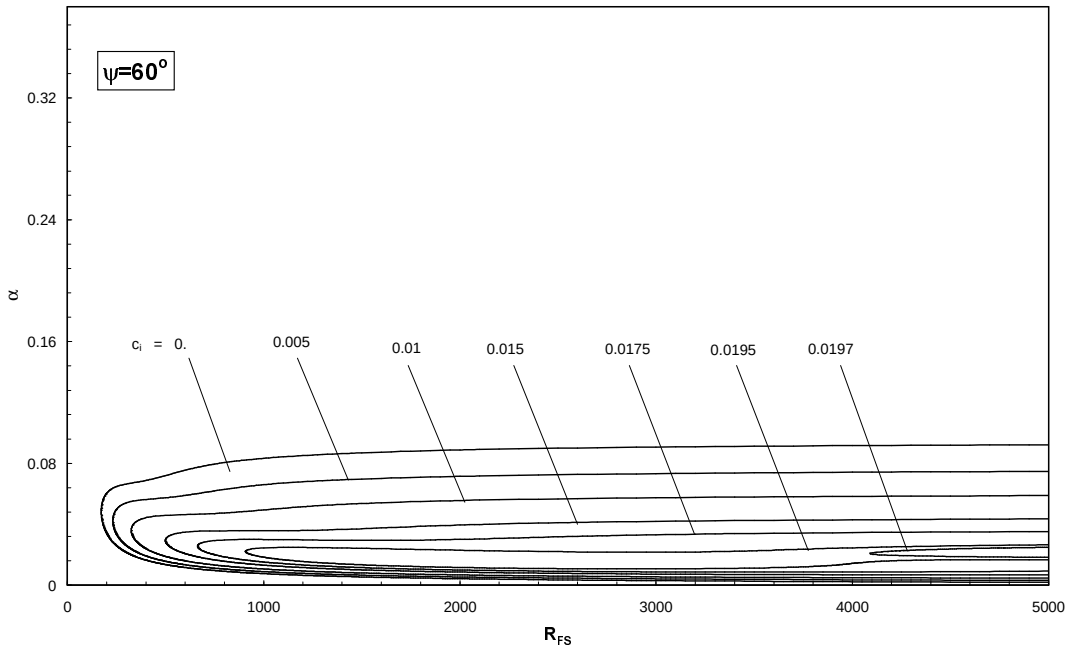

(b)

Figure 5.35 Constant temporal amplification curves for **(a)** the plane waves and **(b)** the most unstable oblique waves at M=4.

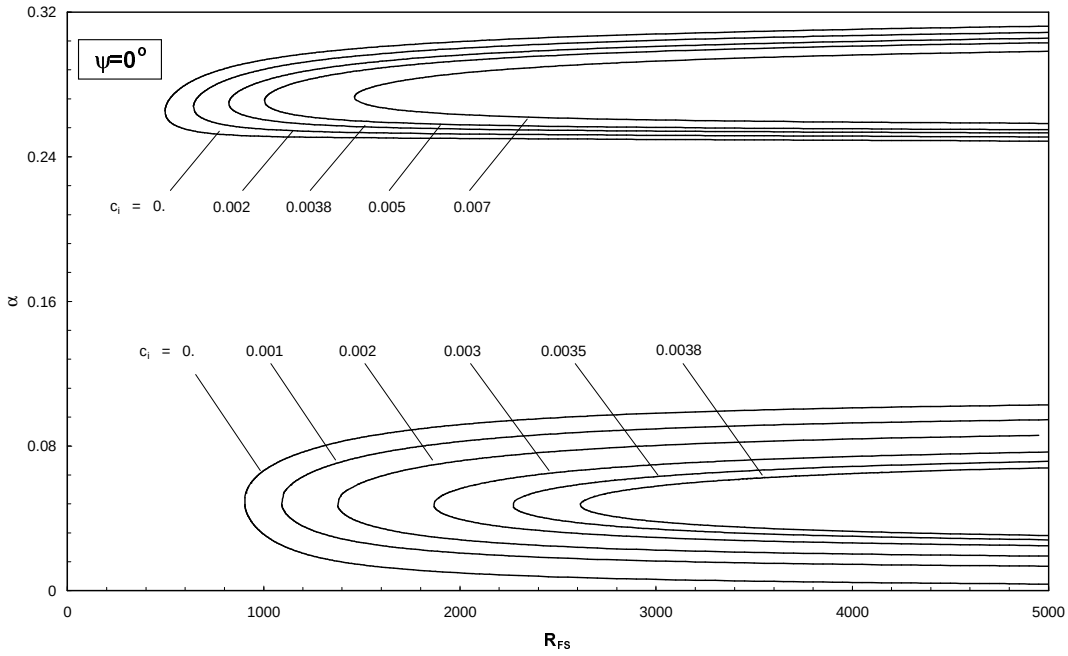

(a)

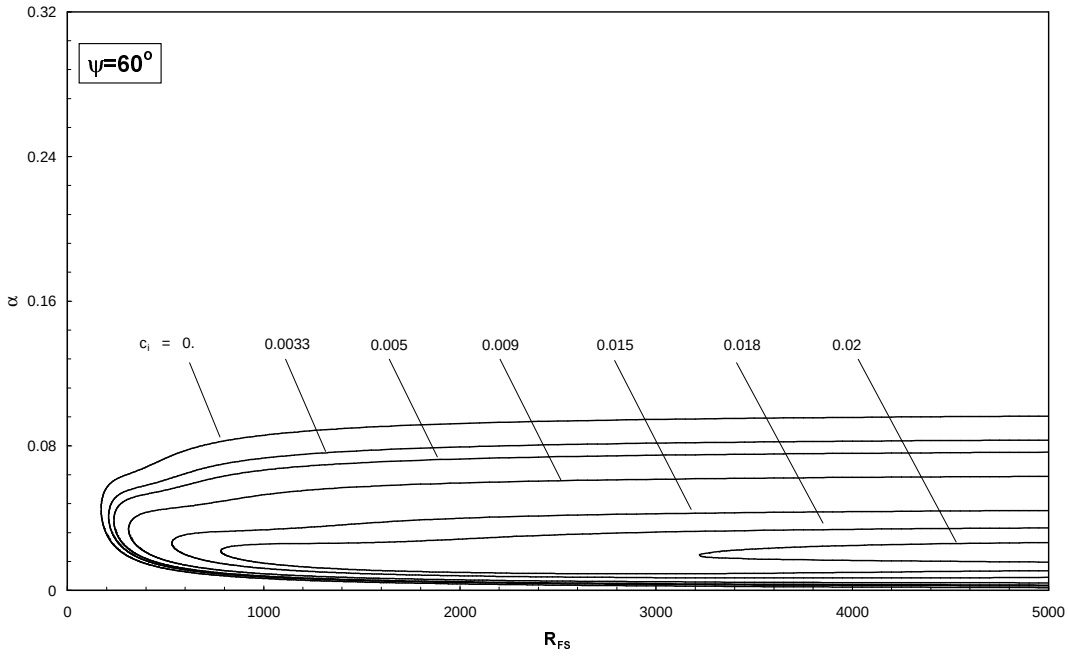

(b)

Figure 5.36 Constant temporal amplification curves for **(a)** the plane waves and **(b)** the most unstable oblique waves at M=4.5.

5.4 Prediction of Transition Location

The preceding steps have been performed not only to demonstrate the effect of Mach number on the stability characteristics but also to examine the influence of three-dimensionality on instability at specified Mach numbers. One important outcome of those analyses is the determination of the direction giving the most unstable wave which is first introduced to the boundary layer. However, it is still questionable where transition occurs and which frequency yields it earliest. The present section hence is concentrated on predicting the transition location which is undertaken by these most unstable disturbances.

It is known that nature always chooses the wave of most unstable frequency in the most unstable direction to yield the transition. Even though the direction at which the transition will occur is identified now, it is still unknown which of the constant frequency waves will go through the transition earlier at those directions.

The different combinations of the stability characteristics obtained by the code are capable of finding the curves of constant frequency waves. A detailed explanation about the methodology is available in Chapter 4. These curves basically represent the integrated growth rates of the corresponding waves. Plotting these constant frequency curves in the most unstable direction, which is one of the most important consequences of the linear stability theory, is the last step before estimating the transition Reynolds number.

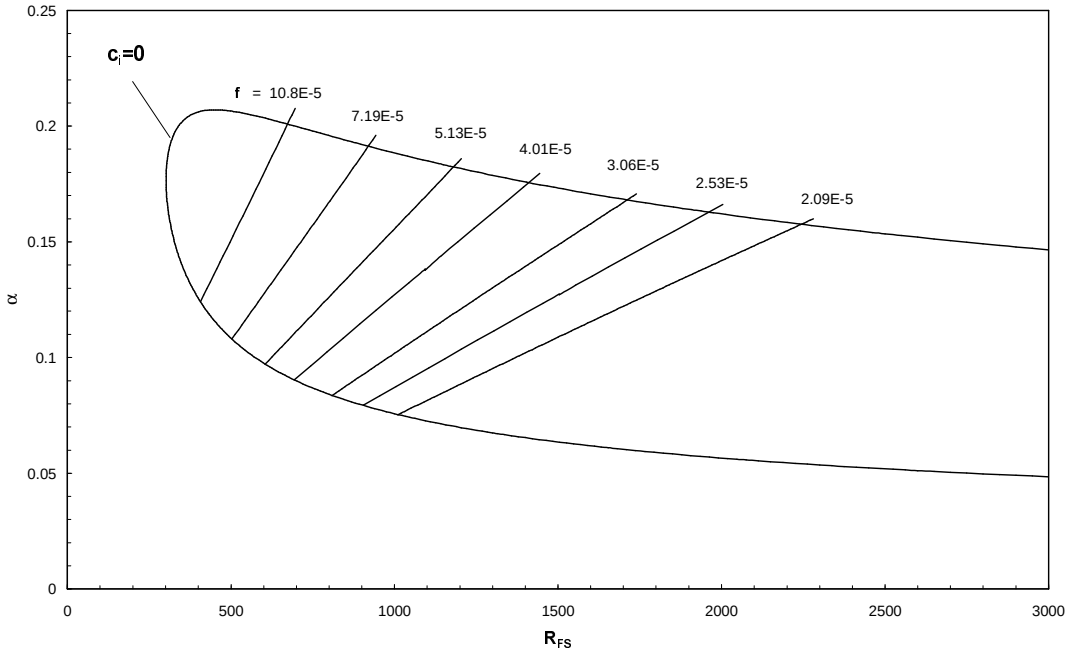

Figure 5.37 Neutral stability curve and the wave trajectories of some single frequency waves through the unstable region for plane waves at M=0.

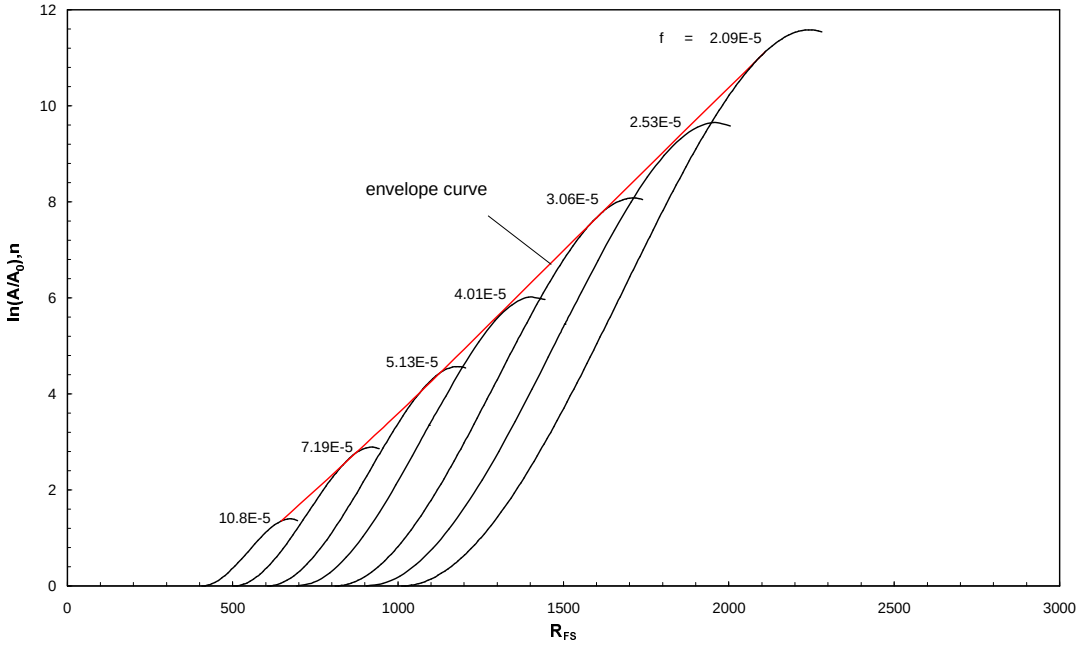

Figure 5.38 Integrated growth rates and the envelope curve of the constant frequency waves in the most unstable direction, $\psi = 0^\circ$ at M=0.

Figure 5.37 is an example to illustrate the trajectories of some constant frequency waves at $M = 0$ in (α, R) plane through the unstable region where they are amplified. It is important to note that, the following representations throughout this section are all in the most unstable directions at corresponding flow speeds. The current diagram is then the one at $\psi = 0^{\circ}$, plane wave condition at zero Mach.

Here, it is clear that smaller frequencies pass through the unstable region with longer trajectories. The figure well depicts the Reynolds number values, i.e., the locations for each wave where it starts amplifying (R_0) and where it starts damping (R_1). If transition occurs within these locations by any of the constant frequency, then the corresponding wave continues to grow as moving further downstream even though the current configuration of the linear theory says it should damp after sometime. This means, the (α, R) diagram loses its validity in representing the disturbance behaviors after the point of transition. This was earlier mentioned in Chapter 4.

Another point is that the amplification of the disturbances is much stronger for smaller frequencies. It is better visualized in Figure 5.38. Here, the same frequency waves in Figure 5.37 at $M = 0$ are figured out in a different plane showing their local integrated growth rates. Each S-shape representing the local $\ell n(A/A_0)$ is set to zero at $R = R_0$ where the amplification starts. Besides, at the boundary points of amplification, at $R = R_0$ and $R = R_1$, each curve demonstrates a zero slope.

Remember that, this figure has been previously visualized in Chapter 4 for the reader to have an idea about the growth rates and the curve of envelope which is the tangent line to these S-shapes. This curve giving the maximum amplification possible at any Reynolds number is the final step of the stability problem. The latter is to investigate the value of envelope, 'n' yielding to transition so that the corresponding Reynolds number on this curve would be the one at which breakdown to turbulence occurs; that is the *transition Reynolds number (R_{tr})*. In the current study, these parts will be discussed after the envelope curves are found for all related Mach numbers in the next pages.

Mack [11] has a similar configuration showing the variation of $\ell n(A/A_0)$ as a function of R_{FS} for 2D Blasius boundary layer. Comparison of Figure 5.38 with his diagram results in a perfect match not only for the frequency waves but also the envelope curve as well. This can be easily verified by checking the Reynolds number values corresponding to similar n-factors on this curve.

Figure 5.39 and Figure 5.40 represent the integrated growth rates of some constant frequency waves at M=0.5 and at sonic speed, respectively. Here, the most unstable disturbances are again two-dimensional similar to M=0 case. The smaller frequencies have more pronounced amplifications as expected because the paths they follow in unstable region are longer. In the meantime, one recognizes that the frequencies that yield similar n-factors get smaller as the Mach number increases from zero to one. This is in fact observable up to M=2 (see the next figures).

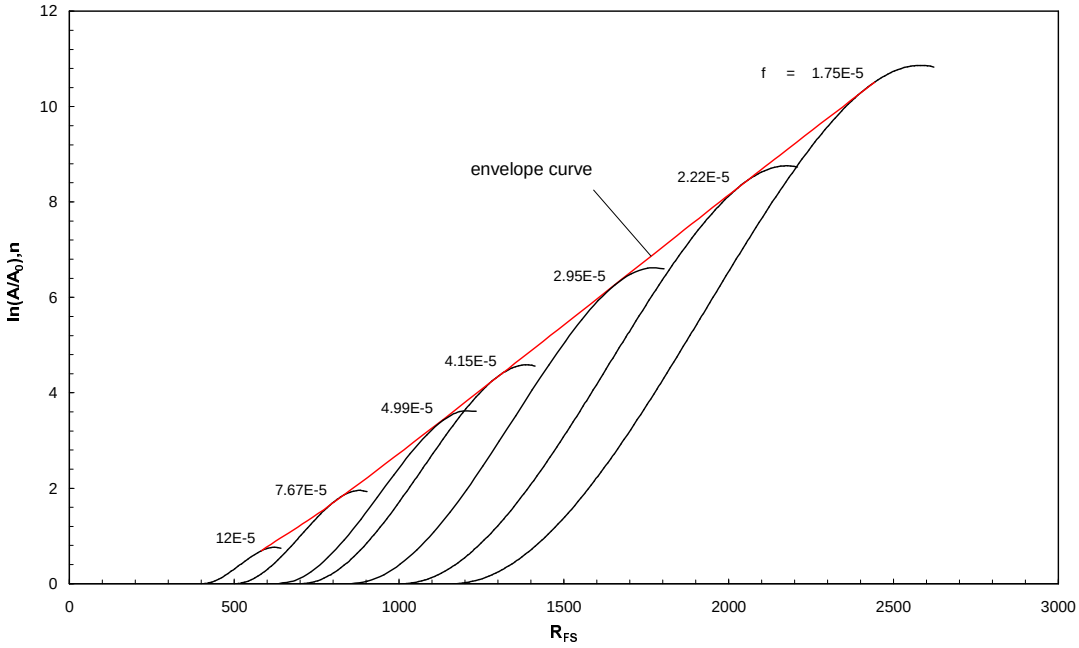

Figure 5.39 Integrated growth rates and the envelope curve of the constant frequency waves in the most unstable direction, $\psi = 0^{\circ}$ at M=0.5.

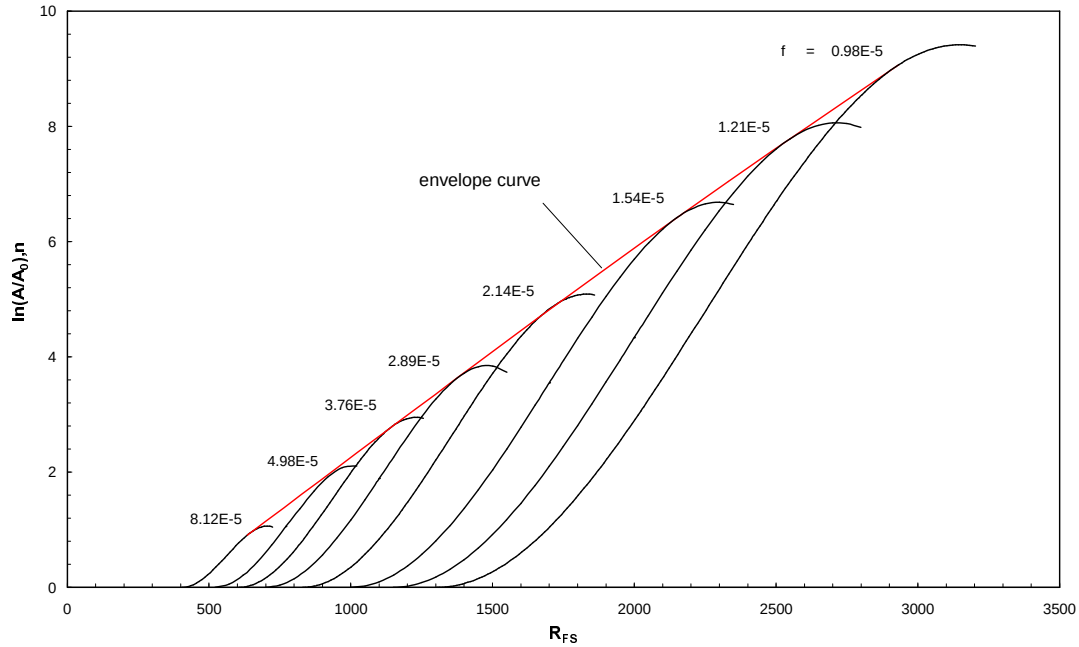

Figure 5.40 Integrated growth rates and the envelope curve of the constant frequency waves in the most unstable direction, $\psi = 0^{\circ}$ at M=1.

Another effect of Mach number observed in $M = 0 - 1$ range is the considerable motion of envelope curve towards the longitudinal axis accompanied by the noticeable decrease in its slope. This will be recognized better while handling with only the maximum amplification curves in the next pages.

Looking at Figure 5.41 plotted for the oblique waves in the direction of $\psi = 30^{\circ}$ at M=1.5, one sees that the growth speed of amplification rates slows down for smaller frequencies. What it causes is the further decrease in the slope of the maximum amplification curve meaning that same n-factors are pronounced now at larger Reynolds numbers compared to previous cases.

The effect of the Mach number on the maximum amplification curve including M=1.5 achieves a reversed trend as the Mach number increases further. This is first observed in Figure 5.42. In this case where the Mach number is M=2 and the most unstable direction is 45°, the envelope curve shows a little increase in its slope.

Figure 5.43 is the demonstration of the integrated growth rates at M=3 for again oblique waves but now with an angle of $\psi = 55^{\circ}$. Here, it is more distinguishable than M=2 case that the similar growth rates occur at lower Reynolds numbers compared to smaller Mach numbers. Another observation could be the gradual increase in frequency values compared to the ones corresponding to the same maximum amplification ratio at smaller Mach numbers. This increase actually starts at M=2 but it is hardly recognizable there. At higher Mach numbers whereas, this is much more pronounced.

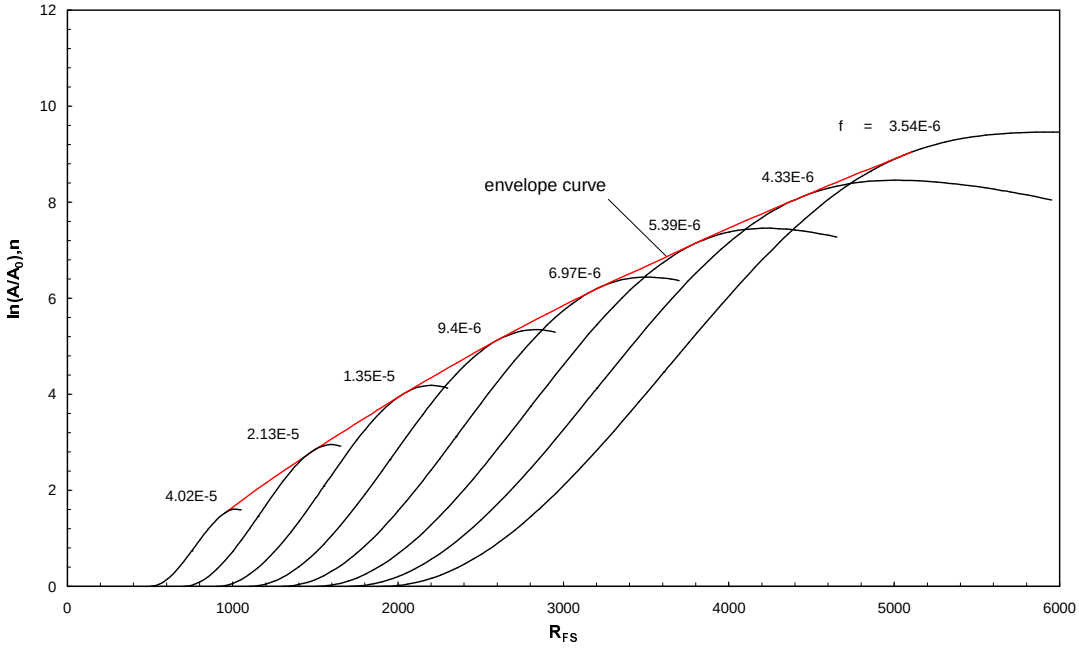

Figure 5.41 Integrated growth rates and the envelope curve of the constant frequency waves in the most unstable direction, $\psi = 30^{\circ}$ at M=1.5.

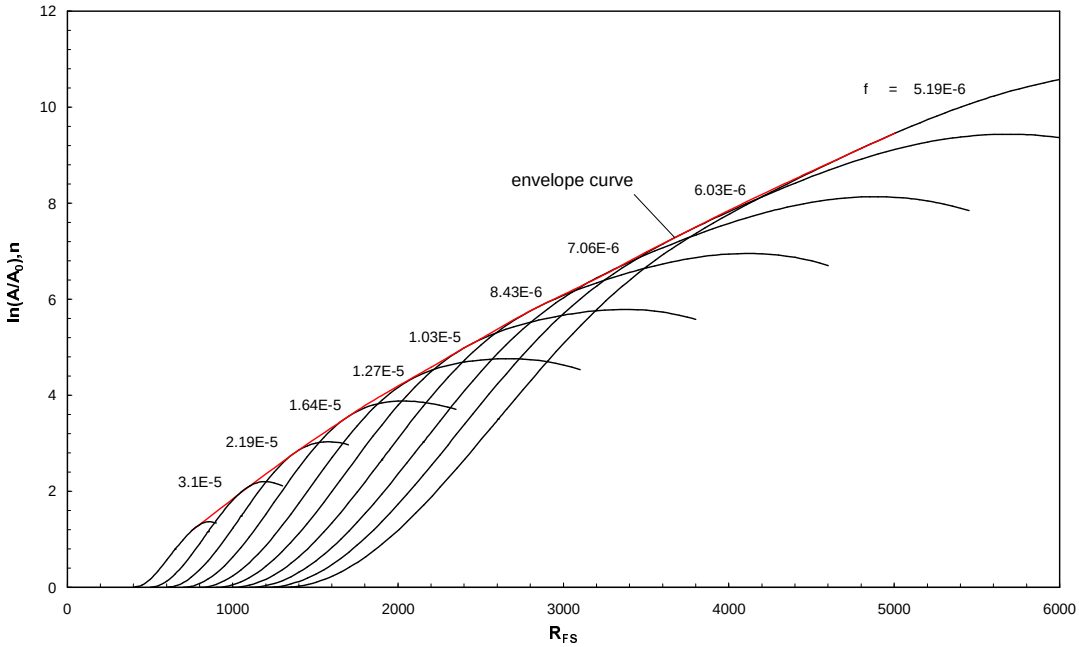

Figure 5.42 Integrated growth rates and the envelope curve of the constant frequency waves in the most unstable direction, $\psi = 45^{\circ}$ at M=2.

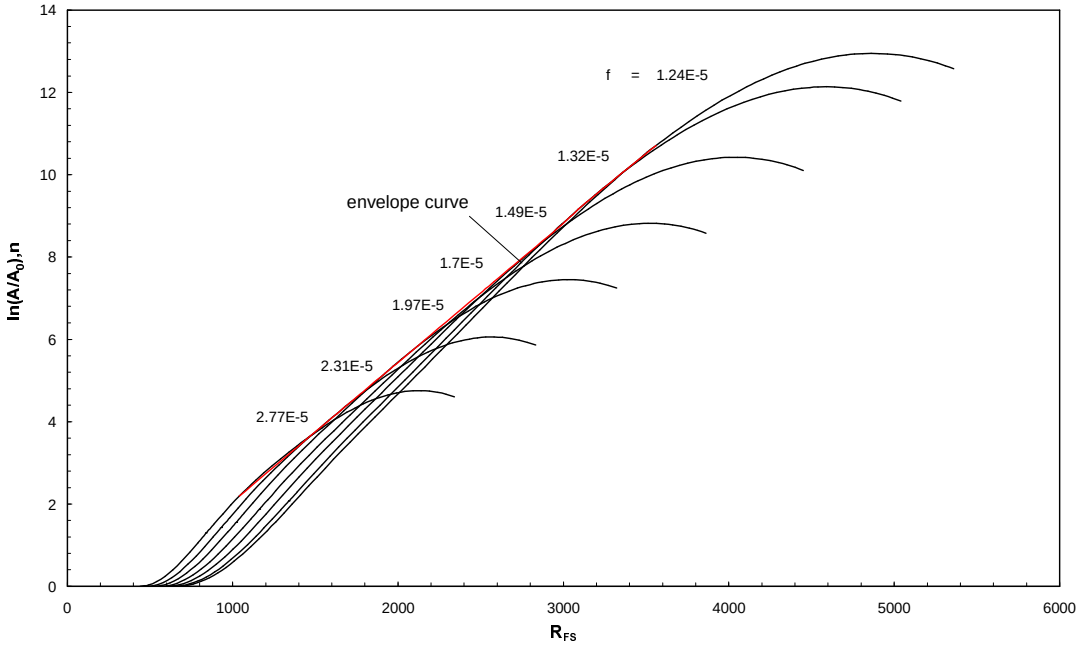

Figure 5.43 Integrated growth rates and the envelope curve of the constant frequency waves in the most unstable direction, $\psi = 55^{\circ}$ at M=3.

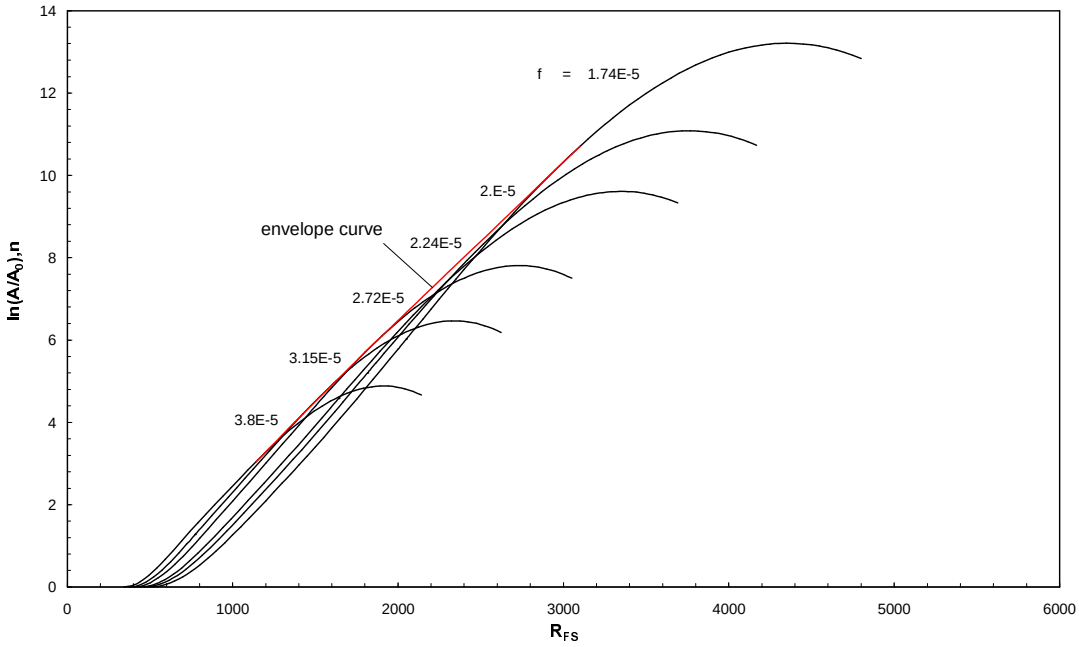

Figure 5.44 Integrated growth rates and the envelope curve of the constant frequency waves in the most unstable direction, $\psi = 60^{\circ}$ at M=4.

Mack's investigations [12] include the local growth rates of the unstable waves at the same Mach number and the same direction of Figure 5.43. His results are represented in exponential terms, i.e., in terms of (A/A_0) and perfectly agree with the present case when converted into the current representation of $\ell n(A/A_0)$.

In Figure 5.44, amplification behaviors of the single frequency waves in the most unstable direction at M=4 is presented. Here, one can spot the apparent shift of envelope curve towards the lateral axis similar to M=2 and M=3. This in fact, causes the location of transition to move further upstream towards the leading edge meaning an earlier transition.

The effect of Mach number in its current trend is preserved up to M=4. Figure 5.45 plotted at M=4.5 well demonstrates that the amplification rate of a disturbance yields to maximum at a Reynolds number which is slightly larger than at M=4. Consequently, the point where the transition occurs would be a bit downstream at Mach 4.5. This is a valid observation if maximum n-factor giving the transition location is larger than 3. Whereas, for $n \langle 2-3$ it is the opposite; the location where the amplification rate is maximum on the flat plate moves upstream. At any specified n-factor, Figure 5.45 also depicts that similar to previous three cases, the minimum frequency value reaching to the corresponding amplification ratio slightly increases.

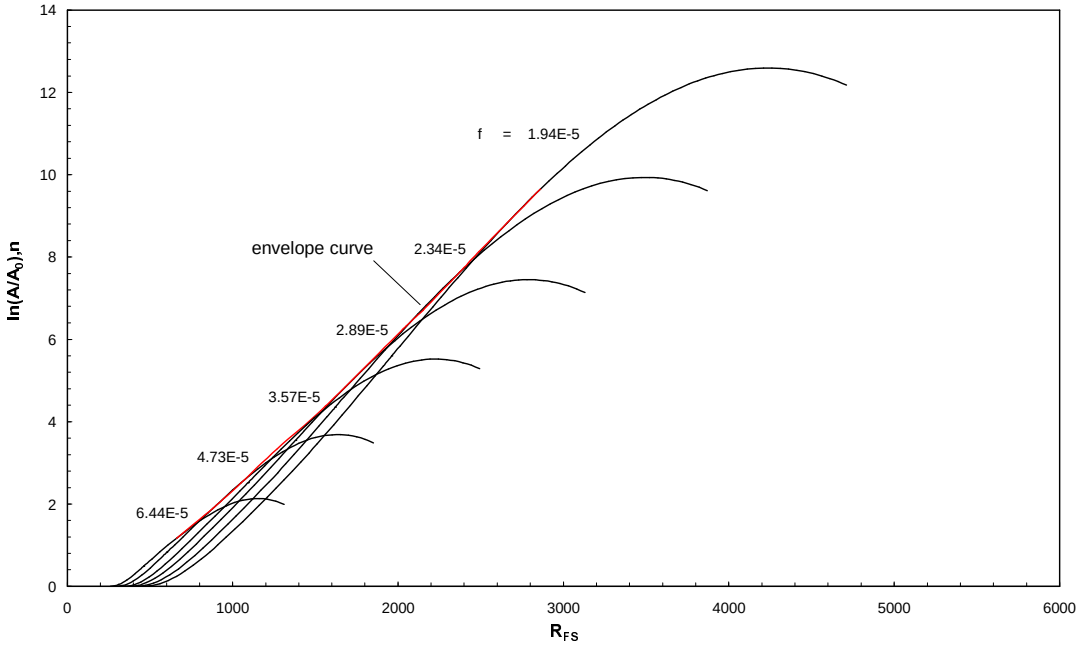

Figure 5.45 Integrated growth rates and the envelope curve of the constant frequency waves in the most unstable direction, $\psi = 60^{\circ}$ at M=4.5.

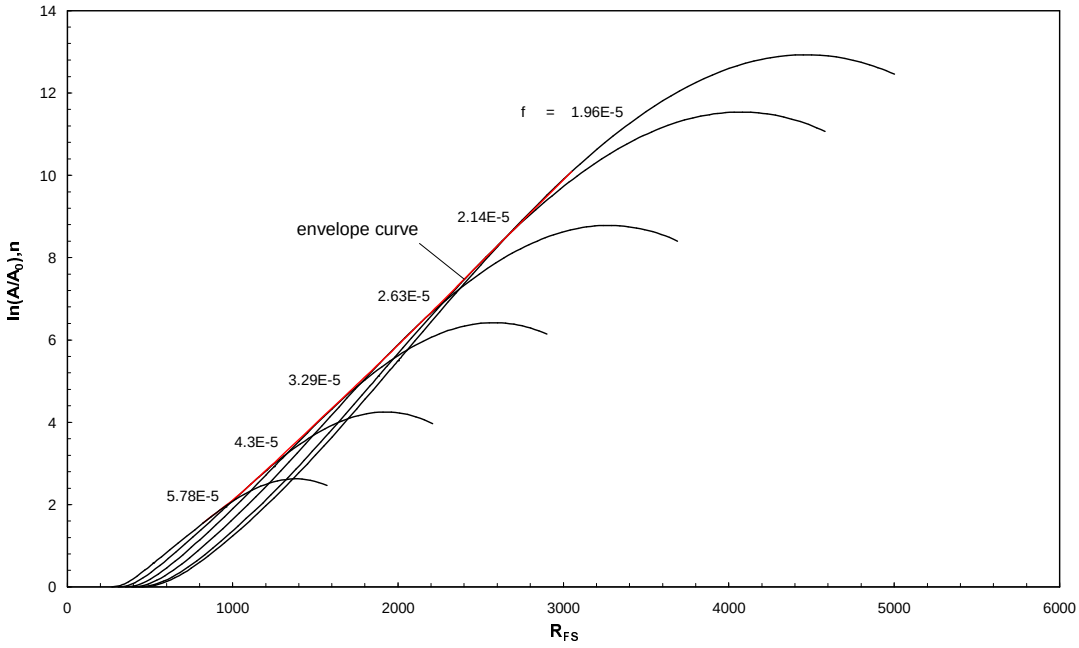

Figure 5.46 Integrated growth rates and the envelope curve of the constant frequency waves in the most unstable direction, $\psi = 60^{\circ}$ at M=5.

Mack's studies [12] about the same topic at M=4.5 with a wave angle of $\psi = 60^{\circ}$ demonstrate exponentially the integrated growth rates for a few frequencies. Converting them into suitable forms of $\ell n(A/A_0)$, one observes a very good match with the results given in Figure 5.45.

The last case investigated in this section is 2D boundary layer flow at M=5 in its most unstable direction, $\psi = 60^{\circ}$. The related configuration, Figure 5.46 shows that the effect of Mach number on the envelope curve and on the corresponding frequencies is similar to what is observed at M=4.5. Here, the shift in the envelope curve is towards slightly larger Reynolds numbers compared to M=4.5.

Figure 5.47 summarizes the effect of freestream Mach number on maximum amplification rates clarified before for each case individually. Once again, the envelope curve moves to larger Reynolds numbers with a decrease in its slope from M=0 to M=1.5. Then, it moves in the opposite direction towards smaller Reynolds numbers up to M=4. The reversal in trend occurs within the range of M=2 and M=3. After M=4, the curve shifts again to larger Reynolds number gradually up to M=5.

The influence of the freestream Mach number on the maximum amplification ratios can also be used to estimate roughly the behavior of the transition Reynolds number. Then, with regard to Figure 5.47, R_{tr} would increase between M=0 and M=2 followed by a decrease from M=2 to M=4 and again increase after M=4. This is exactly what Arnal [2] and Mack [11] mention about the Mach number effect on transition location.

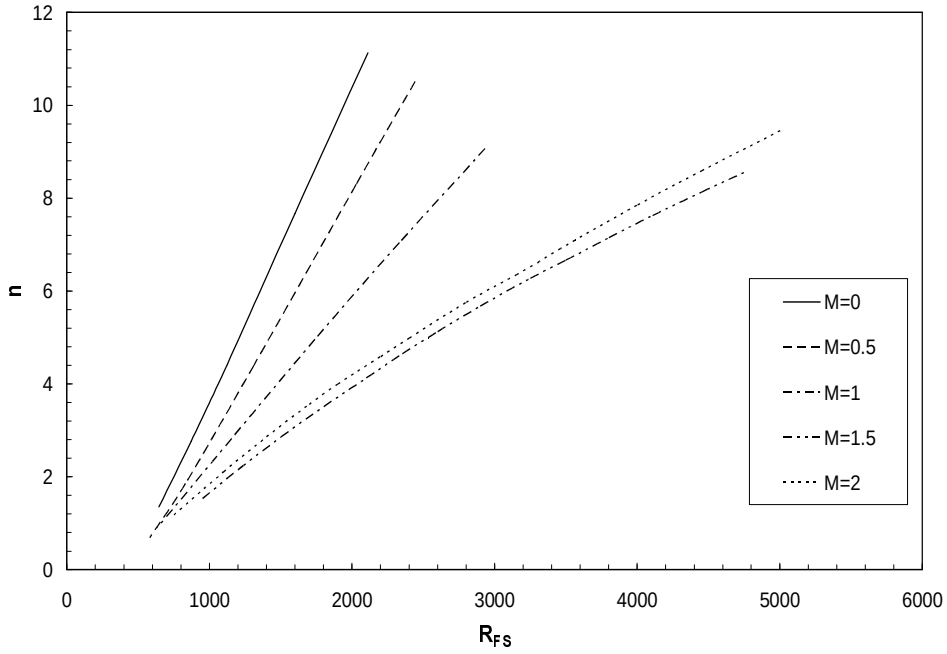

(a)

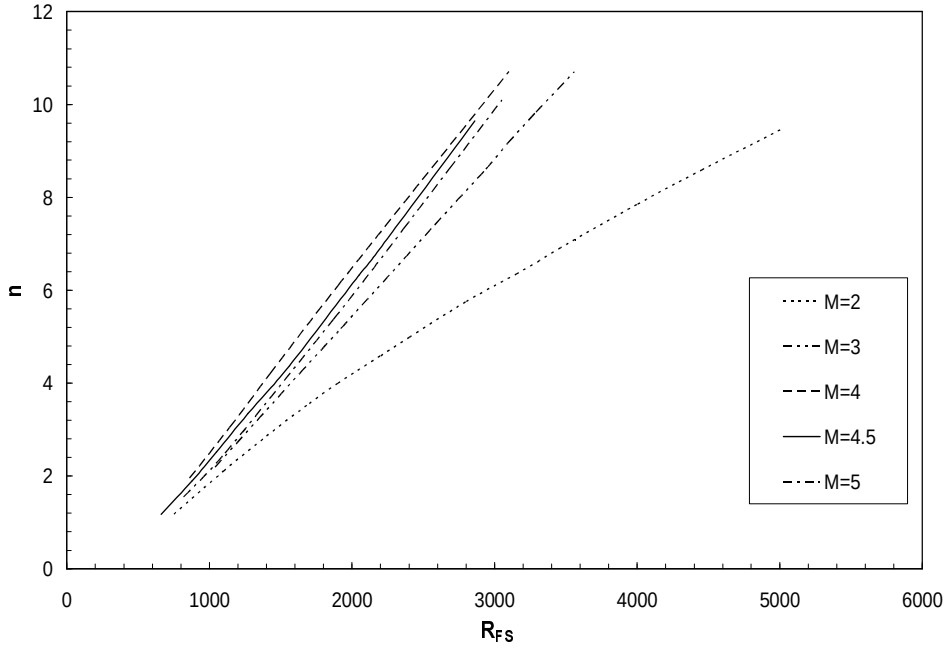

(b)

Figure 5.47 Effect of Mach number on envelope curves within a range of **(a)** M=0 to M=2, **(b)** M=2 to M=5.

Referring to [2] and [11], one will observe that both correlate the transition location directly to stability, i.e., they depict the increasing/decreasing effect of Mach number on transition Reynolds number as stabilizing/destabilizing of flow. Considering the definition of critical Reynolds number as *the point where the instability first occurs*, it is in fact, much more meaningful to concentrate on this critical value while investigating the stabilizing or destabilizing effect of any factor rather than transition Reynolds number. The results of the present study are then discussed in this respect. Anyway, what is actually meant by Arnal [2] and Mack [11] is the Mach number effect on transition Reynolds number which shows perfect agreement with the current estimations.

As mentioned in the beginning, it would be a rough estimation to consider only the behaviors of the envelope curve against the Mach number while analyzing its influence on transition location even though the results are quite compatible with the literature. The reason is that n-factor yielding to transition is still not identified. In this manner, the next is the investigation of the n-factor giving the transition Reynolds number.

The estimation of n_{max} (or, n_{tr}) is based on Mack's proposal [12] which has been clarified in Chapter 4 within a detailed format including the reasons of its use. To remind, the methodology was performed by Mack [12] as a trial and error process in order to converge the transition locations found by some wind tunnel experiments. The same technique has been used in the current study. Referring to Eq. (4.27) and Eq. (4.28), the procedure is repeated for $A/A_r = 100,\ 150,\ 200,\ 300$ and 400. The n-factors obtained by each ratio at the corresponding Mach numbers are then listed in Table 5.3.

Table 5.3 Maximum amplification ratios yielding to transition at related Mach numbers evaluated by the selected A/A_r ratios.

Mach no.	$n_{transition}$ $(A/A_r = 100)$	$n_{transition}$ $(A/A_r = 150)$	$n_{transition}$ $(A/A_r = 200)$	$n_{transition}$ $(A/A_r = 300)$	$n_{transition}$ $(A/A_r = 400)$
0.0	4.61	5.01	5.30	5.70	6.0
0.5	4.61	5.01	5.30	5.70	6.0
1.0	4.61	5.01	5.30	5.70	6.0
1.5	4.32	4.72	5.01	5.42	5.70
2.0	3.74	4.15	4.43	4.84	5.13
3.0	2.93	3.34	3.62	4.03	4.31
4.0	2.36	2.76	3.05	3.46	3.74
4.5	2.12	2.53	2.81	3.22	3.5
5.0	1.90	2.32	2.60	3.0	3.30

It is necessary to remember that for the cases of $M < 1.3$, the initial amplitude, A_0 is accepted to be equal to the reference amplitude, A_r, i.e., the effect of local Mach number is to be neglected in Eq. (4.27) and the relation is simplified to $A/A_r = A/A_0$. This is the reason why the first three rows representing the n-factors at M=0, M=0.5 and M=1 are exactly the same.

The remaining is the estimation of Reynolds numbers corresponding to each of these n-factors using the envelope curves of related Mach cases. Figure 5.48 illustrates these values together with the experimental data found in literature. This is in fact, a demonstration of the Mach number effect on the transition Reynolds number estimated for different amplitude ratios of A/A_r.

Each curve corresponds to a distinct amplitude ratio and the individual symbols represent the experimentally obtained transition Reynolds numbers. The different colors are used to distinguish the

experiments performed by different scientists meaning different wind tunnels (probably different disturbance environments as well). Accordingly, for M=0, the flat plate transition Reynolds number of Schubauer and Skramstad [5] has been used. For M=1.6, Kendall's result [37] has been used.

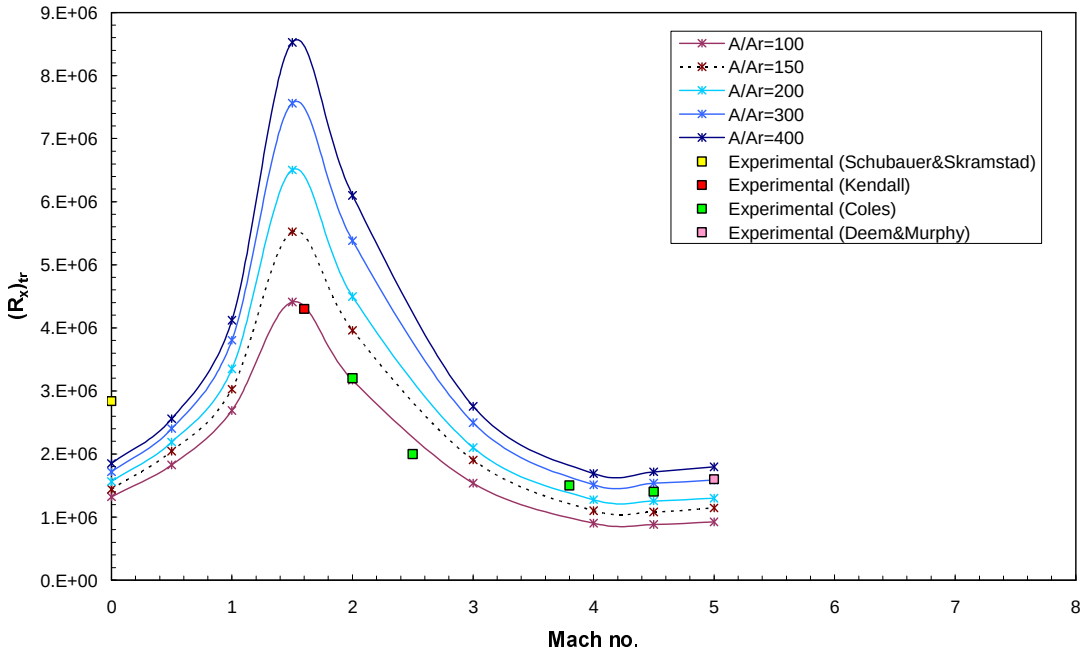

Figure 5.48 Application of A/A_r method and visualization of the Mach number effect on transition Reynolds number.

Four transition locations between M=2 and M=4.5 in Figure 5.48 have been covered by Coles' data [38] for a flat plate in a different wind tunnel. The last point corresponding to M=5 whereas belongs to Deem and Murphy [39]. It is important to notice that these experimental criteria are exactly the ones that have been also used by Mack [12] in comparison of his own results.

Here in Figure 5.48, R_x is nothing but the streamwise Reynolds number defined as $\left(\rho_e^* U_e^* x^* / \mu_e^*\right)$ [12]. It is used just to attain an easy comparison not only with the experimental data but also with the Mack's results [12] as well.

As seen in this diagram, the transition locations at M=1.6, M=2 and at M=2.5 are in perfect agreement with the curve plotted by current results for $A/A_r = 100$. However, the locations for the Mach numbers from M=3.8 to M=5 show a quite high compatibility with the present results for $A/A_r = 300$ in such a way that at M=5 they almost exactly match. Beyond this, the experiments of Laufer and Marte [40] conclude with a maximum at M=1.6. This is also proven by the peaks observed in each curve of Figure 5.48.

For the first point corresponding to M=0, one can notice the high disagreement with the estimated Reynolds numbers. Remember that, for the incompressible cases, the n-factor yielding to transition is between 7and 9 (see Chapter 4). Hence, for M=0 case representing the incompressible flow, such a difference is pretty much expected considering the n-factors used in the current estimations (see Table 5.3). Taking a typical factor of $n = 9$, the corresponding Reynolds number on the related envelope curve in Figure 5.47(a) yields $R_{FS} = 1800$, i.e., $R_x = 3.24 \text{x} 10^6$. Although it is slightly larger than the experimental value of $R_x = 2.84 \text{x} 10^6$ [5], a perfect agreement is maintained by many studies in literature, one of which is Cebeci [20]. Cebeci further clarifies that the numerical results agree well with experiment for a factor of 8.2. The same conclusion is valid for also the present study giving

exactly the experimental value. One can easily verify this by again using the corresponding curve of envelope in Figure 5.47(a).

Table 5.4 Comparison of the transition Reynolds numbers obtained using the ratios of $A/A_r = 100$, 150 and 200 with the experimental data.

Mach no.	$(R_x)_{tr}$ x10^{-6} (Exper.)	$(R_x)_{tr}$ x10^{-6} $(A/A_r = 100)$	% dif.	$(R_x)_{tr}$ x10^{-6} $(A/A_r = 150)$	% dif.	$(R_x)_{tr}$ x10^{-6} $(A/A_r = 200)$	% dif.
0.0	2.84	1.32	53.5	1.44	49.3	1.56	45.1
1.6	4.30	4.30	0.	5.4	25.6	6.40	48.9
2.0	3.20	3.17	0.9	3.90	21.8	4.49	40.3
2.5	2.00	2.30	15.	2.80	40.	3.10	55.
3.8	1.50	1.00	33.3	1.20	20.	1.30	13.3
4.5	1.40	0.88	37.1	1.08	22.8	1.25	10.7
5.0	1.60	0.92	42.5	1.15	28.1	1.23	23.1

Table 5.5 Comparison of the transition Reynolds numbers obtained using the ratios of $A/A_r = 300$ and 400 with the experimental data.

Mach no.	$(R_x)_{tr}$ x10^{-6} (Exper.)	$(R_x)_{tr}$ x10^{-6} $(A/A_r = 300)$	% dif.	$(R_x)_{tr}$ x10^{-6} $(A/A_r = 400)$	% dif.
0.0	2.84	1.72	39.4	1.85	34.8
1.6	4.30	7.45	73.2	8.45	96.5
2.0	3.20	5.39	68.4	6.10	90.6
2.5	2.00	3.80	90.	4.25	112.
3.8	1.50	1.65	10.	1.85	23.3
4.5	1.40	1.54	10.	1.72	22.8
5.0	1.60	1.59	0.6	1.79	11.8

The numerical comparison of the remaining current data with the experimental transition criteria is given in Table 5.4 and Table 5.5 together with the percentage differences. It is now much clear that $A/A_r = 150$ case seems the best even though some of the results agree perfectly with

$A/A_r = 100$ and some with $A/A_r = 300$. Knowing the effect of wind tunnel size on transition as depicted by Pate and Schueler [8] (see Chapter 1), here one should bear in mind that the current comparison may not give universally correct results since these data are from the measurements of different wind tunnels.

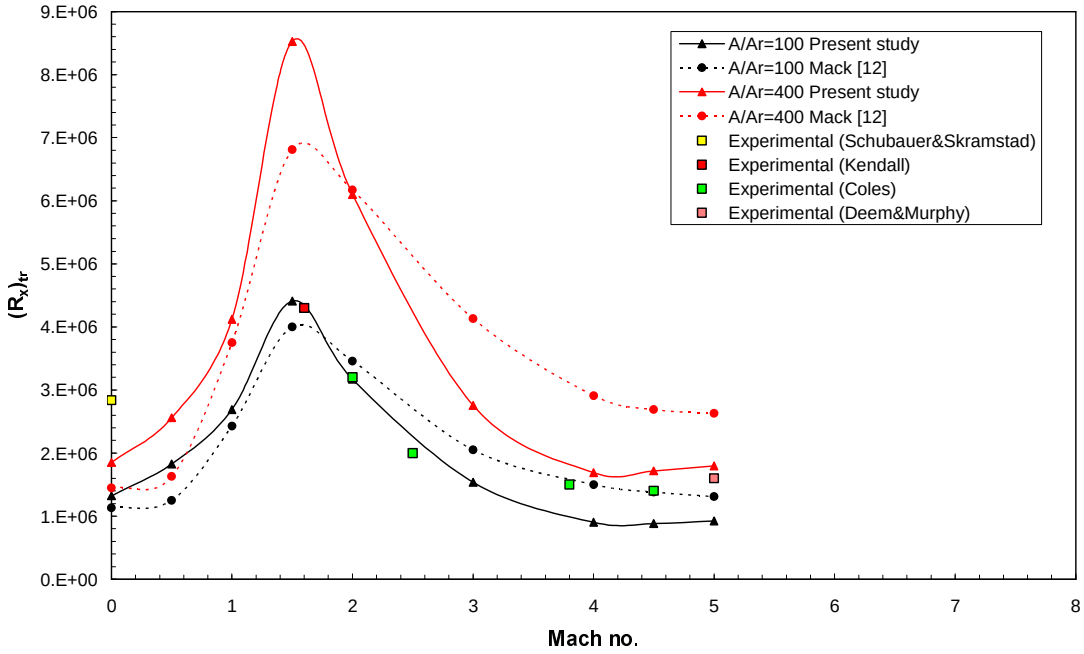

Figure 5.49 Comparison of the currently obtained transition Reynolds numbers with both graphical values of Mack [12] and the experimental data.

Here, it is necessary to declare that the similar disagreements exist in Mack's results, too. Figure 5.49 visualizes the estimated values from a graphical representation which has been plotted by Mack with a curve fitting in [12]. Here, one can see the differences in Mack's data and the experimental transition data as well as the discrepancies with the present results.

Table 5.6 Comparison of the currently obtained transition Reynolds numbers with the numerical results in [12].

Mach no.	$(R_x)_{tr}$ x10^{-6} $(A/A_r = 100)$		% dif.	$(R_x)_{tr}$ x10^{-6} $(A/A_r = 400)$		% dif.
	Mack [12]	Present study		Mack [12]	Present study	
0.0	1.13	1.32	16.8	1.45	1.85	27.6
0.5	1.25	1.83	46.4	1.63	2.56	57.1
1.0	2.43	2.69	10.7	3.75	4.13	10.1
1.5	4.	4.41	10.2	6.81	8.53	22.6
2.0	3.56	3.17	10.9	6.37	6.10	4.2
3.0	2.25	1.55	31.1	4.13	2.76	33.2
4.0	1.5	0.90	40.	2.81	1.69	39.8
4.5	1.38	0.88	36.2	2.69	1.72	36.
5.0	1.31	0.92	29.8	2.63	1.8	31.5

To compare numerically the current data with Mack's results [12], one can refer to Table 5.6. The percentage values show considerable differences at some Mach numbers as well as good agreements at some others. A graphical representation of this comparison can be seen in Figure 5.49. The reasons for the disagreements were clarified in the previous chapters. To remind, in the current study the parameter of Prandtl number is taken as constant unlike Mack [11]. Another difference is about the definition of the viscosity parameter. In the current study, Sutherland's formula has been used for this purpose, whereas Mack defines it with a different relation with constant coefficients in cgs system. As a consequence of discrepancies of these, the definition of coefficient of thermal conductivity shows a variation as well.

The reference temperature is another point creating confliction with the current study. It is taken as $50\,K$ by Mack [11, 12] for higher Mach numbers which is quite low compared to the current value, $288\,K$. This can indeed cause considerable discrepancies in numerical results.

One last point is that in spite of his detailed numerical formulations represented in [12], Mack does not give any clue about the usage of energy equation while defining the mean flow. This is an important detail considering the high effect of mean flow profiles on the results.

CHAPTER 6

CONCLUSIONS AND RECOMMENDATIONS

The present study is based on the analysis of stability and transition for two-dimensional, viscous, compressible boundary layers over adiabatic flat plates. In the respect of linear stability theory and its fundamental tools depicted in Chapter 2, the current equation system has been modeled yielding an eigenvalue problem. The numerical analysis has been performed by developing a FORTRAN code shaped by the methods clarified in Chapter 3 so that the stability problem could be handled for either 2D or 3D mean flows with either two- or three-dimensional sinusoidal disturbances. In the present study however, only 2D mean flow case has been investigated considering both types of disturbances. The determination of the stability characteristics and following the transition prediction analysis performed by the current code concentrate on temporal amplification theory.

The preliminary step was the investigation of the stability characteristics for *plane waves*. Starting from M=0 to higher Mach numbers including M=7, the eigenvalues of the compressible problem have been obtained and represented in various configurations. The commonly preferred was the demonstration of constant temporal amplification curves in (α, R_{FS}) plane implying the variation of wave number with respect to the

Reynolds number. The analysis has started with plotting such diagrams for M=0, M=1 and M=2 to examine the Mach number effect on the isolines of such low flow speeds. The importance of zero Mach case which has been declared previously is to be its correspondence to the simplest and commonly studied incompressible case. The first step in confirmation of the solution method and the code written in this study was hence to be the comparison of this case with the incompressible data in literature and the result was an excellent agreement both graphically and numerically rendering the current study worthwhile.

With the increase of flow speed in M=0-2 range, one has recognized that the amplification factor curves get slightly closer to the peak point. But the shapes do not alter in a significant manner. This is nothing but due to the dominant effect of the viscous instability which was indicated in the stability diagrams of Arnal [2] as well. Comparing his results with the current ones has yielded a very good agreement bearing in mind the difference in applied amplification theories.

For specified Mach numbers in small increments within the range of M=0 to M=3.5, the curves of neutral stability, i.e., the $c_i = 0$ isolines have been plotted isolated from other c_i-curves to demonstrate the instability behavior better. The first observation was the dominancy of inflectional instability occurring after M=2 unlike the lower Mach numbers. At higher speeds, the range where it is dominant became smaller and smaller in stability diagram meaning that the destabilizing effect of viscosity weakened further. This is also supported by Mack's observations [11] and Arnal's numerical solutions [2] as well. One should again notice while comparing with Arnal's results

that, the amplification theories applied in both the current and his cases are different. That's why, a quantitative match can not be expected.

From these isolated neutral stability curves, it was also possible to observe the influence of Mach number on critical Reynolds number for plane waves. Accordingly, the critical Reynolds number initially decreases up to M=1.5. Then, it increases continuously as the flow speeds up further. This indicates that the Mach number has a destabilizing effect on plane waves following with a stabilizing effect after M=1.5. As an additional effort, these values have been converted to proper ones based on displacement thickness so as to compare with what Arnal has found in [2]. A detailed numerical comparison has then been concluded with a very good agreement except for M=3. The discrepancy was followed by the corresponding neutral stability curve as well. The reason was most probably due to the different approaches handled for some key parameters during the solution of the stability problem which have been clarified in previous chapter with a detailed format. The results have also been compared by Mack's proper data [11] by representing them at a different scale. Except for a small discrepancy, the compatibility with those by Mack has been well established. The reasons for the small disagreement have been declared in the previous chapter.

A further increase in Mach number let the additional mode, the second mode be visualized. From M=4 to M=7, the neutral stability curves have depicted the behavior of two modes very well. Accordingly, as the Mach number increases, the first mode goes through a slight enlargement in its unstable region and the second mode appears at much smaller wave numbers so that they join each other concluding with a single neutral

stability curve and unstable region. The motion of these two modes shows great compatibility with the numerical results present in literature. However, the Mach number range through which these modes are separate in related preceding studies does not agree with the current range. The related discussions have concluded with that a perfect match can not be expected because of the discrepancies observed in value of reference temperature, the variety of Prandtl number, the definition of viscosity coefficient as well as the thermal conductivity. Beyond all, it is inevitable to suspect those in literature about how they had introduced the energy equation to mean flow problem.

The next step was the investigation of stability properties for *oblique waves*. In this case, the freestream Mach number has been restricted to M=5 because of the chemical reactions possibly occurring at hypersonic speeds which is out of the scope of the current study. In the preceding step, i.e., the plane wave case, hypersonic speeds have been investigated just to illustrate the behaviors of higher mode under the effect of Mach number. In this respect, the analysis has been performed for various wave angles at each flow speed in this range in order to identify the effect of three-dimensionality on instability. Accordingly, the results of M=0 and M=1 have shown that the wave angle has a stabilizing effect meaning that the plane waves are more unstable than oblique waves within M=0-1. At that point, referring to the preceding studies in literature, one has resulted in a perfect agreement rendering the effort worthwhile.

However, at higher Mach numbers this pure stabilizing effect has been replaced by initially a destabilizing effect. Then, it has been followed by stabilizing effect again. At each increment of Mach number, the range of the

directions stabilizing the disturbances has been enlarged. In this manner, the angle at which the waves are most unstable has increased so that at M=4, the most unstable direction has referred to $\psi = 60^{\circ}$. The second mode occurring after M=4 whereas, has been observed to be stabilized with the wave orientation. Eventually, these results have been compared with the arguments through numerical solutions of other scientists and excellent match has been converged.

The analysis of transition prediction for compressible flow has been performed after finding the most unstable direction at corresponding flow speeds. The S-shapes representing the local integrated growth rates of constant frequency disturbances have been demonstrated in those most unstable directions. In this respect, the influence of the flow speed on frequencies has been visualized and confirmed by the available ones in literature. Following, the behavior of the envelope curve under the effect of the Mach number has been investigated by visualizing them independently. Lack of experimental or numerical data about the envelope curves at supersonic speeds in literature has led us to just go further next step. It was indeed encouraging to obtain a complete match with the arguments in literature even by a rough estimation of transition location using a guessed n-factor at these curves.

Lastly, the current study has concentrated on the value of n-factor leading to transition. For this purpose, a different method based on Mack's proposal [12] was undertaken. The procedure has been repeated to find the best case that gives Reynolds numbers close to the experimental transition criteria which were also used by Mack [12]. The results were quite

satisfactory so that in some case exactly same Reynolds numbers have been found for some Mach numbers. However, a perfect match could not be maintained because of the nonlinearities possibly affecting the experimental results. To remind, these effects are neglected by the linear theory.

To conclude, the results obtained in this study are the products of a set of complete and a well-proven theory. The great compatibility with the preceding numerical studies in literature at each current stage renders this effort worthwhile as well as the excellent agreement provided with the theoretical background. The satisfactory results obtained by the method of transition prediction besides complement the study in a successive manner. The limitations of the method and the code could be just due to the range of validity of the empirical relation used for the viscosity and the assumption of constant Prandtl number.

A further investigation in this area could be the stability analysis for a much complex case, 3D mean flows led by the introduction of crossflow velocity profile. Because the compressible system has been currently governed for a general flow case, the only need for the present code would be a few modifications; may be in definitions of stability characteristics.

Another forward step would be to take the chemical reactions into account for hypersonic Mach numbers. This could complicate the analysis at least by an order of magnitude but there are examples of such studies in literature that achieved success.

REFERENCES

[1] Saric W.S., "Physical Description of Transition: Experimental Evidence" *AGARD FDP/VKI* Special Course on Progress in Transition Modeling, Madrid, March 1993 and Brussels, March-April 1993.

[2] Arnal, D., "Boundary Layer Transition: Predictions Based on Linear Theory", *AGARD Report 793*, Special Course on Progress in Transition Modeling, Brussels, 1993.

[3] Morkovin, M.V., "On the Many Faces of Transition", *Viscous Drag Reduction*, Ed. C. S. Wells, Plenum, 1969.

[4] Schlichting, H., *Boundary Layer Theory*, McGraw-Hill, Inc., 1979.

[5] Schubauer, G.B. and Skramstad, H.K., "Laminar Boundary Layer Oscillations and Transition on a Flat Plate", *Report 909* NACA, 1948.

[6] Lees, L. and Lin, C.C., "Investigation of the Stability of the Laminar Boundary Layer in a Compressible Fluid", *NACA TN n° 1115*, 1946.

[7] Spangler, J.G. and Wells, C.S., "Effects of Freestream Disturbances on Boundary Layer Transition", *AIAA Journal*, Vol. 6, n° 3, pp. 543-545, 1968.

[8] Pate, S.R. and Schueler, C.J., "Radiated Aerodynamic Noise Effects on Boundary Layer Transition in Supersonic and Hypersonic Wind Tunnels", *AIAA Journal*, Vol. 7, nº 3, pp. 450-457, 1969.

[9] Reshotko, E., "Stability Theory as a Guide to the Evaluation of Transition Data", *AIAA Journal*, Vol. 7, nº 6, pp. 1086-1091, 1969.

[10] Reshotko, E., "Boundary Layer Stability and Transition", *Ann. Rev. Fluid Mech.*, 1976.

[11] Mack, L.M., "Boundary Layer Linear Stability Theory", *Special Course on Stability and Transition of Laminar Flows*, *AGARD Report* nº 709, 1984.

[12] Mack, L.M., "Linear Stability Theory and the Problem of Supersonic Boundary Layer Transition", *AIAA J.*, Vol. 13, nº 3, pp. 278-289, 1975.

[13] Arnal, D., "Laminar-Turbulent Transition Prediction in Three Dimensional Flows", *Progress in Aeros. Sciences*, nº 3, pp.173-191, 2000.

[14] Masad, J.A. and Abid, R., "On Transition in Supersonic and Hypersonic Boundary Layers", *Int. J. Engng Sci.*, Vol. 33, nº 13, pp. 1893-1919, 1995.

[15] Baines, P.G., Majumdar, S.J. and Mitsudera H., "The mechanics of the Tollmien-Schlichting wave", *J. Fluid Mech.*, Vol. 312, pp. 107-124, 1996.

[16] Hu, S. and Zhong, X., "Linear Stability of Viscous Supersonic Plane Couette Flow", *Physics of Fluids*, Vol. 10, nº 3, pp. 709-729, 1997.

[17] Özgen, S., *Two-layer Flow Stability in Newtonian and Non-Newtonian Fluids*, Ph.D. Dissertation, Univeriste Libre de Bruxelles, Von Karman Institute For Fluid Dynamics, Brussels, 1999.

[18] Atalayer, H.S. and Özgen, S., "Analysis of Stability and Transition in Compressible Boundary Layers Using Linear Stability Theory", *WSEAS Conference on Fluid Dynamics, Corfu, Greece*, 2004.

[19] Anderson, J.D., *Fundamentals of Aerodynamics*, McGraw-Hill, Inc., 1991.

[20] Cebeci, T. and Cousteix, J., *Modeling and Computation of Boundary Layer Flows*, Springer, 1998.

[21] Schetz, J.A., *Foundations of Boundary Layer Theory for Momentum, Heat and Mass Transfer*, Prentice-Hall, Inc., 1984.

[22] Gaster, M., "A note on a Relation Between Temporally Increasing and Spatially Increasing Disturbances in Hydrodynamic Stability", *J. Fluid Mech.,* Vol. 14, pp. 222-224, 1962.

[23] Gaster, M., "On the Generation of Spatially Growing Waves in a Boundary Layer", *J. Fluid Mech.,* Vol. 22, pp. 433-441, 1965.

[24] Drazin, P.G and Reid, W.H., *Hydrodynamic Stability*, Cambridge Uni. Press, 1981.

[25] Brown, W.B., "A Stability Criterion for Three-Dimensional Laminar Boundary Layer", *Boundary Layer and Flow Control*, Pergamon Press, Vol. 2, pp. 913-923, 1961.

[26] Press, W.H., Teukolsky, S.A., Vetterling, W.T. and Flannery, B.P., *Numerical Recipes in Fortran 77*, Vol. 1, Cambridge Uni. Press, 1996.

[27] Nachtsheim, P.R. and Swigert, P., "Satisfaction of Asymptotic Boundary Conditions in Numerical Solution of Systems of Nonlinear Equations of boundary Layer type", TND-3004, NASA, 1965.

[28] Van Driest, E.R., "Investigation of Laminar Boundary Layer in Compressible Fluids Using Crocco Method", NACA TN 2579, 1952.

[29] Mack, L.M., "A Numerical Study of the Temporal Eigenvalue Spectrum of the Blasius Boundary Layer", *J. Fluid Mech.*, Vol. 301, 1976.

[30] Nelder, J.H. and Mead, R., *Computer Journal* 7: 308-313, 1965.

[31] Smith, AMO and Gamberoni, N., "Transition, Pressure Gradient and Stability Theory", Report ES 26388, Douglas Aircraft Co., Calif., 1956.

[32] Lees, L., "Instability of Laminar Flows and Transition to Turbulence", Report ZA-7-006, Consolidated Aircraft Corp., San Diego, 1952.

[33] Laufer, J., "Some Statistical Properties of the Pressure Field Radiated by a Turbulent Boundary Layer", *Physics of Fluid*, Vol. 7, nº 8, pp.1191-1197, 1964.

[34] Gaster, M., "On the Effects of Boundary Layer Growth on Flow Stability", J. Fluid Mech., Vol. 66, pp. 465-480, 1974.

[35] Bertolotti, F.P., "Compressible Boundary Layer Analyzed with the PSE equations", AIAA Paper nº 91-1637, 1991.

[36] Chang, C.L., Malik, M.R., Erlebacher, G., Hussaini M.Y., "Compressible Stability of Growing Boundary Layers Using Parabolized Stability Equations", AIAA Paper nº 91-1636, 1991.

[37] Kendall, J.M., "JPL Experimental Investigations", *Proceedings of the Boundary Layer Transition Workshop*, Vol. IV, Aerospace Corp. California, 1971.

[38] Coles, D., "Measurements of Turbulent Friction on a Smooth Flat Plate in Supersonic Flow", J. of Aeronautical Sciences, Vol. 21, nº 7, pp. 433-448, 1954.

[39] Deem, R.E. and Murphy, J.S., "Flat Plate Boundary Layer Transition at Hypersonic Speeds", AIAA Paper Vol. 65, New York, 1965.

[40] Laufer, J. and Marte, J.E., "Results and a Critical Discussion of Transition Reynolds Number Measurements on Insulated Cones and Flat Plates in Supersonic Wind Tunnels", Report 20-96, Jet Propulsion Lab., California, 1973.

APPENDIX A

COEFFICIENT MATRIX OF THE GOVERNING SYSTEM OF FIRST ORDER DIFFERENTIAL EQUATIONS

In Chapter 2, Eqs. (2.42)-(2.47) are reorganized in the form of first order differential equations in order to proceed with a convenient numerical solution. In this respect, the new variables are defined as Z_i (i=1,8) and the basic equations of the compressible stability theory are rearranged as:

$$DZ_1 = Z_2, \tag{A.1}$$

$$\begin{aligned} DZ_2 &= D(DZ_1) \\ &= \left[\frac{iR}{\mu T}B + A\right]Z_1 + \left[-\frac{1}{\mu}\frac{d\mu}{dT}DT\right]Z_2 \\ &+ \left[\frac{R}{\mu T}(\alpha DU + \beta DW) - \frac{i}{3}A\frac{DT}{T} - \frac{i}{\mu}\frac{d\mu}{dT}ADT\right]Z_3 \\ &+ \left[\frac{R}{\mu}iA - \frac{AB}{3}\gamma M^2\right]Z_4 \\ &+ \left[\frac{AB}{3T} - \frac{1}{\mu}\frac{d\mu}{dT}(\alpha D^2U + \beta D^2W) - \frac{1}{\mu}\frac{d^2\mu}{dT^2}DT(\alpha DU + \beta DW)\right]Z_5 \\ &+ \left[-\frac{1}{\mu}\frac{d\mu}{dT}(\alpha DU + \beta DW)\right]Z_6, \end{aligned} \tag{A.2}$$

$$
\begin{aligned}
DZ_3 &= D\bar{v} \\
&= [-i]Z_1 \\
&+\left[\frac{DT}{T}\right]Z_3 \\
&+\left[-iB\gamma M^2\right]Z_4 \\
&+\left[\frac{iB}{T}\right]Z_5, \qquad \text{(A.3)}
\end{aligned}
$$

$$
\begin{aligned}
DZ_4 &= \frac{D\bar{p}}{\gamma M^2} \\
&= \left[-\frac{i}{E}\left(\frac{2}{\mu}\frac{d\mu}{dT}DT+\frac{4}{3}\frac{DT}{T}\right)\right]Z_1+\left[-\frac{i}{E}\right]Z_2 \\
&+\left[\frac{1}{E}\left(\frac{-iR}{\mu T}B+\frac{4}{3}\frac{D^2T}{T}-A+\frac{4}{3\mu}\frac{d\mu}{dT}\frac{(DT)^2}{T}\right)\right]Z_3 \\
&+\left[-\frac{i}{E}\frac{4}{3}\gamma M^2\left(\frac{DT}{T}B+\alpha DU+\beta DW+\frac{1}{\mu}\frac{d\mu}{dT}BDT\right)\right]Z_4 \\
&+\left[\frac{i}{E}\left((\alpha DU+\beta DW)\left(\frac{4}{3T}+\frac{1}{\mu}\frac{d\mu}{dT}\right)+\frac{4}{3}\frac{1}{\mu}\frac{d\mu}{dT}\frac{DT}{T}B\right)\right]Z_5 \\
&+\left[\frac{i}{E}\frac{4}{3}\frac{B}{T}\right]Z_6, \qquad \text{(A.4)}
\end{aligned}
$$

$$
DZ_5 = Z_6, \qquad \text{(A.5)}
$$

$$DZ_6 = D(DZ_5)$$

$$= \left[-(\gamma - 1)\Pr M^2 \frac{2}{A}(\alpha DU + \beta DW) \right] Z_2$$

$$+ \left[\frac{R\Pr}{\mu}\frac{DT}{T} - 2i(\gamma - 1)M^2 \Pr(\alpha DU + \beta DW) \right] Z_3$$

$$+ \left[\frac{-(\gamma - 1)\Pr R}{\mu} iBM^2 \right] Z_4$$

$$+ \left[\frac{\Pr R}{\mu T} iB + A - \frac{1}{\kappa}\frac{d\kappa}{dT} D^2 T - \frac{1}{\kappa}\frac{d^2\kappa}{dT^2}(DT)^2 + (\gamma - 1)M^2 \frac{\Pr}{\mu}\frac{d\mu}{dT}\left((DU)^2 + (DW)^2\right) \right] Z_5$$

$$+ \left[-\frac{2}{\kappa}\frac{d\kappa}{dT} DT \right] Z_6$$

$$+ \left[-(\gamma - 1)\Pr M^2 \frac{2}{A}(\alpha DW - \beta DU) \right] Z_8, \qquad (A.6)$$

$$DZ_7 = Z_8, \qquad (A.7)$$

$$DZ_8 = D(DZ_7)$$

$$= \left[\frac{R}{\mu T}(\alpha DW - \beta DU) \right] Z_3$$

$$+ \left[-\frac{1}{\mu}\frac{d\mu}{dT}(\alpha D^2 W - \beta D^2 U) - \frac{1}{\mu}\frac{d^2\mu}{dT^2} DT(\alpha DW - \beta DU) \right] Z_5$$

$$+ \left[-\frac{1}{\mu}\frac{d\mu}{dT}(\alpha DW - \beta DU) \right] Z_6$$

$$+ \left[\frac{R}{\mu T} iB + A \right] Z_7$$

$$+ \left[-\frac{1}{\mu}\frac{d\mu}{dT} DT \right] Z_8 . \qquad (A.8)$$

where, $A=\left(\alpha^2+\beta^2\right)$, $B=\left(\alpha U+\beta W-\omega\right)$, $E=\left[R/\mu+i4/3\gamma M^2 B\right]$ and 'D' denotes the differentiation with respect to dimensionless y distance. These equations can also be represented in the following matrix form as well:

$$DZ_i=\sum_{j=1}^{8}a_{ij}Z_j, \qquad i=1,8, \tag{A.9}$$

so that,

$$a_{11}=a_{13}=a_{14}=a_{15}=a_{16}=a_{17}=a_{18}=0,$$

$$a_{12}=1,$$

$$a_{21}=\frac{iR}{\mu T}B+A,$$

$$a_{22}=-\frac{1}{\mu}\frac{d\mu}{dT}DT,$$

$$a_{23}=\frac{R}{\mu T}\left(\alpha DU+\beta DW\right)-\frac{i}{3}A\frac{DT}{T}-\frac{i}{\mu}\frac{d\mu}{dT}ADT,$$

$$a_{24}=\frac{R}{\mu}iA-\frac{AB}{3}\gamma M^2,$$

$$a_{25}=\frac{AB}{3T}-\frac{1}{\mu}\frac{d\mu}{dT}\left(\alpha D^2U+\beta D^2W\right)-\frac{1}{\mu}\frac{d^2\mu}{dT^2}DT\left(\alpha DU+\beta DW\right),$$

$$a_{26}=-\frac{1}{\mu}\frac{d\mu}{dT}\left(\alpha DU+\beta DW\right),$$

$$a_{27}=a_{28}=0,$$

$$a_{31}=-i,$$

$$a_{32}=0,$$

$$a_{33} = \frac{DT}{T},$$

$$a_{34} = -iB\gamma M^2,$$

$$a_{35} = \frac{iB}{T},$$

$$a_{36} = a_{37} = a_{38} = 0,$$

$$a_{41} = -\frac{i}{E}\left(\frac{2}{\mu}\frac{d\mu}{dT}DT + \frac{4}{3}\frac{DT}{T}\right),$$

$$a_{42} = -\frac{i}{E},$$

$$a_{43} = \frac{1}{E}\left(\frac{-iR}{\mu T}B + \frac{4}{3}\frac{D^2T}{T} - A + \frac{4}{3\mu}\frac{d\mu}{dT}\frac{(DT)^2}{T}\right),$$

$$a_{44} = -\frac{i}{E}\frac{4}{3}\gamma M^2\left(\frac{DT}{T}B + \alpha DU + \beta DW + \frac{1}{\mu}\frac{d\mu}{dT}BDT\right),$$

$$a_{45} = \frac{i}{E}\left((\alpha DU + \beta DW)\left(\frac{4}{3T} + \frac{1}{\mu}\frac{d\mu}{dT}\right) + \frac{4}{3}\frac{1}{\mu}\frac{d\mu}{dT}\frac{DT}{T}B\right),$$

$$a_{46} = \frac{i}{E}\frac{4}{3}\frac{B}{T},$$

$$a_{47} = a_{48} = 0,$$

$$a_{51} = a_{52} = a_{53} = a_{54} = a_{55} = a_{57} = a_{58} = 0,$$

$$a_{56} = 1,$$

$$a_{61} = 0,$$

$$a_{62} = -(\gamma - 1)\Pr M^2\frac{2}{A}(\alpha DU + \beta DW),$$

$$a_{63} = \frac{R\Pr}{\mu}\frac{DT}{T} - 2i(\gamma - 1)M^2\Pr(\alpha DU + \beta DW),$$

$$a_{64} = \frac{-(\gamma-1)\Pr R}{\mu} iBM^2,$$

$$a_{65} = \frac{\Pr R}{\mu T} iB + A - \frac{1}{\kappa}\frac{d\kappa}{dT} D^2T - \frac{1}{\kappa}\frac{d^2\kappa}{dT^2}(DT)^2 + (\gamma-1)M^2\frac{\Pr}{\mu}\frac{d\mu}{dT}\left((DU)^2 + (DW)^2\right),$$

$$a_{66} = -\frac{2}{\kappa}\frac{d\kappa}{dT} DT,$$

$$a_{67} = 0,$$

$$a_{68} = -(\gamma-1)\Pr M^2 \frac{2}{A}(\alpha DW - \beta DU),$$

$$a_{71} = a_{72} = a_{73} = a_{74} = a_{75} = a_{76} = a_{77} = 0,$$

$$a_{78} = 1,$$

$$a_{81} = a_{82} = 0,$$

$$a_{83} = \frac{R}{\mu T}(\alpha DW - \beta DU),$$

$$a_{84} = 0,$$

$$a_{85} = -\frac{1}{\mu}\frac{d\mu}{dT}\left(\alpha D^2W - \beta D^2U\right) - \frac{1}{\mu}\frac{d^2\mu}{dT^2} DT(\alpha DW - \beta DU),$$

$$a_{86} = -\frac{1}{\mu}\frac{d\mu}{dT}(\alpha DW - \beta DU),$$

$$a_{87} = \frac{R}{\mu T} iB + A,$$

$$a_{88} = -\frac{1}{\mu}\frac{d\mu}{dT} DT. \qquad \text{(A.10)}$$

APPENDIX B

FORMULATION OF VELOCITY AND TEMPERATURE PROFILES

The formulation for *2D mean flow* over a flat plate having zero pressure gradient starts with the compressible boundary layer equations [19]:

Continuity: $$\frac{\partial}{\partial x^*}\left(\rho^* U^*\right)+\frac{\partial}{\partial y^*}\left(\rho^* V^*\right)=0,$$

x-momentum: $$\rho^* U^* \frac{\partial U^*}{\partial x^*}+\rho^* V^* \frac{\partial U^*}{\partial y^*}=\frac{\partial}{\partial y^*}\left(\mu^* \frac{\partial U^*}{\partial y^*}\right),$$

y-momentum: $$\frac{\partial P^*}{\partial y^*}=0,$$

Energy: $$\rho^* U^* \frac{\partial h^*}{\partial x^*}+\rho^* V^* \frac{\partial h^*}{\partial y^*}=\frac{\partial}{\partial y^*}\left(\kappa^* \frac{\partial T^*}{\partial y^*}\right)+\mu^*\left(\frac{\partial U^*}{\partial y^*}\right)^2. \qquad \text{(B.1)}$$

For the velocity profiles, x-momentum equation of the compressible boundary-layer equations is taken into consideration. For the temperature profiles whereas, one has to refer to the energy equation.

Here, the well-known procedure, transformation of independent variables is performed with $\zeta^* = x^*$ and $y=\sqrt{U_e^*/\nu_e^* x^*}\,y^*$ so that the derivatives become:

$$\frac{\partial}{\partial x^*} = \frac{\partial}{\partial \zeta^*} + \frac{\partial y}{\partial x^*}\frac{\partial}{\partial y}, \qquad \frac{\partial}{\partial y^*} = \sqrt{\frac{U_e^*}{\nu_e^* x^*}}\frac{\partial}{\partial y}. \tag{B.2}$$

As mentioned in Chapter 2, the dimensionless stream function is defined by the following:

$$f_{FS} = \frac{\Psi^*}{\sqrt{U_e^* \nu_e^* x^*}}. \tag{B.3}$$

Using this parameter and knowing that $U^* = \partial\psi^*/\partial y^*$, $V^* = -\partial\psi^*/\partial x^*$, one obtains:

$$\rho^* U^* = \rho_e^* U_e^* f'_{FS} \qquad \Rightarrow \qquad f'_{FS} = U\rho, \tag{B.4}$$

and,

$$\rho^* V^* = -\rho_e^* \left(\frac{1}{2}\sqrt{\frac{\nu_e^* U_e^*}{x^*}} f_{FS} + \frac{\partial y}{\partial x^*}\sqrt{\nu_e^* U_e^* x^*}\, f'_{FS} \right). \tag{B.5}$$

Substituting all into the x-momentum equation in Eqs. (B.1) and making necessary rearrangements one ends up with:

$$2\left[\mu\left(\frac{f'_{FS}}{\rho}\right)'\right]' + f_{FS}\left(\frac{f'_{FS}}{\rho}\right)' = 0 \quad \text{or,} \quad 2\left[\mu U'\right]' + f_{FS} U' = 0. \tag{B.6}$$

Similarly, with the substitution of all into energy equation and in addition, bearing in mind that for a calorically perfect gas, $dh^* = c_p^* dT^*$; the following equation is maintained:

$$2\left[\frac{\mu}{Pr}g'\right]' + f_{FS}g' = -2(\gamma-1)M^2\mu(U')^2. \qquad (B.7)$$

Eqs. (B.6) and (B.7) defining the velocity and temperature profiles constitute the mean flow equations for a compressible boundary layer over an adiabatic flat plate with zero pressure gradient.

APPENDIX C

UNIFORM MEAN FLOW SOLUTIONS

At a sufficient distance, y_e from the wall, the flow is uniform meaning that $U = U_e$, $W = W_e$, $T = 1$, $\mu = 1$, $\kappa = 1$ and all y derivatives of mean flow quantities are zero. Applying these conditions to Eqs. (2.49) or the expanded version as Eqs. (A.1)-(A.8), one obtains the following system with constant coefficients:

$$
\begin{aligned}
DZ_1 &= Z_2, \\
DZ_2 &= \left[iRB_e + A\right]Z_1 + \left[iRA - \frac{AB_e}{3}\gamma M^2\right]Z_4 + \left[\frac{AB_e}{3}\right]Z_5, \\
DZ_3 &= \left[-i\right]Z_1 + \left[-iB_e\gamma M^2\right]Z_4 + \left[iB_e\right]Z_5, \\
DZ_4 &= \left[-\frac{i}{E_e}\right]Z_2 + \left[\frac{-1}{E_e}\left(A + iRB_e\right)\right]Z_3 + \left[\frac{i}{E_e}\frac{4}{3}B_e\right]Z_6, \\
DZ_5 &= Z_6, \\
DZ_6 &= \left[-i(\gamma - 1)\Pr RB_e M^2\right]Z_4 + \left[i\Pr RB_e + A\right]Z_5, \\
DZ_7 &= Z_8, \\
DZ_8 &= \left[iRB_e + A\right]Z_7,
\end{aligned}
\tag{C.1}
$$

where, $A=\left(\alpha^2+\beta^2\right)$, $B_e=\left(\alpha U_e+\beta W_e-\omega\right)$ and $E_e=\left[R+i4/3B_e\gamma M^2\right]$. The general form of the solution of this first order system is hence:

$$Z_i(y)=\vec{\varphi}_i e^{\lambda_i y}, \qquad i=1,8. \tag{C.2}$$

Here, Z_i is the eight component solution vector formed by eight component *characteristic vectors*, $\vec{\varphi}_i$ and eight component *characteristic values*, λ_i.

The first six of Eqs. (C.1) are coupled and can be written as three 2nd order equations having variables, Z_1, Z_4 and Z_5 in the following manner:

$$\begin{aligned} D^2Z_1 &= DZ_2 \\ &= \left[iRB_e+A\right]Z_1+\left[iRA-\frac{A}{3}B_e\gamma M^2\right]Z_4+\left[\frac{A}{3}B_e\right]Z_5, \end{aligned}$$

$$\begin{aligned} D^2Z_4 &= D\left(DZ_4\right) \\ &= \left[A+\frac{R}{E_e}B_e^2M^2\left(\frac{4}{3}\Pr\left(\gamma-1\right)-\gamma\right)\right]Z_4+\frac{R}{E_e}B_e^2\left[1-\frac{4}{3}\Pr\right]Z_5, \end{aligned}$$

$$\begin{aligned} D^2Z_5 &= DZ_6 \\ &= \left[-iR\Pr\left(\gamma-1\right)M^2B_e\right]Z_4+\left[A+iR\Pr B_e\right]Z_5, \end{aligned} \tag{C.3}$$

or, in matrix form:

$$\begin{bmatrix} D^2Z_1 \\ D^2Z_4 \\ D^2Z_5 \end{bmatrix}=\begin{bmatrix} b_{11} & b_{12} & b_{13} \\ 0 & b_{22} & b_{23} \\ 0 & b_{32} & b_{33} \end{bmatrix}\begin{bmatrix} Z_1 \\ Z_4 \\ Z_5 \end{bmatrix}. \tag{C.4}$$

For convenience, the system can be rewritten as:

$$\begin{bmatrix} D^2X_1 \\ D^2X_2 \\ D^2X_3 \end{bmatrix} = \begin{bmatrix} b_{11} & b_{12} & b_{13} \\ 0 & b_{22} & b_{23} \\ 0 & b_{32} & b_{33} \end{bmatrix} \begin{bmatrix} X_1 \\ X_2 \\ X_3 \end{bmatrix}, \tag{C.5}$$

with the coefficients of:

$$b_{11} = A + iRB_e,$$

$$b_{12} = A\left[iR - \frac{1}{3}B_e\gamma M^2 \right],$$

$$b_{13} = \frac{1}{3}AB_e,$$

$$b_{22} = A - \frac{R}{E_e}\left[\gamma - \frac{4}{3}\Pr(\gamma - 1) \right] M^2 B_e{}^2,$$

$$b_{23} = \frac{R}{E_e}\left[1 - \frac{4}{3}\Pr \right] B_e{}^2,$$

$$b_{32} = -iR\Pr(\gamma - 1)M^2 B_e,$$

$$b_{33} = A + iR\Pr B_e. \tag{C.6}$$

This system can be regarded as an independent eigenvalue problem resulting in the following characteristic values:

$$\lambda_{1,2} = \pm\sqrt{b_{11}},$$

$$\lambda_{3,4} = \pm\sqrt{\frac{(b_{22} + b_{33})}{2} + \frac{1}{2}\sqrt{(b_{33} - b_{22})^2 + 4b_{23}b_{32}}},$$

$$\lambda_{5,6} = \pm\sqrt{\frac{(b_{22} + b_{33})}{2} - \frac{1}{2}\sqrt{(b_{33} - b_{22})^2 + 4b_{23}b_{32}}}. \tag{C.7}$$

Chapter 3 well depicts the reason why only the *negative signed* values are taken into consideration. In this respect, the general form of solution of system defined as Eqs. (C.5) would become:

$$X_i(y) = c_1\vec{\xi}_1 e^{\lambda_1 y} + c_3\vec{\xi}_3 e^{\lambda_3 y} + c_5\vec{\xi}_5 e^{\lambda_5 y} \quad \text{for} \quad i = 1,3, \tag{C.8}$$

accompanied by the characteristic vectors of:

$$\vec{\xi}_1 = \begin{bmatrix} \xi_{11} \\ \xi_{12} \\ \xi_{13} \end{bmatrix} = \begin{bmatrix} 1 \\ 0 \\ 0 \end{bmatrix} \qquad \text{for } \lambda_1, \tag{C.9}$$

$$\vec{\xi}_3 = \begin{bmatrix} \xi_{31} \\ \xi_{32} \\ \xi_{33} \end{bmatrix} = \begin{bmatrix} \dfrac{b_{12}\left(b_{33} - \lambda_3^2\right) - b_{32}b_{13}}{b_{32}\left(b_{11} - \lambda_3^2\right)} \\ -\dfrac{1}{b_{32}}\left[b_{33} - \lambda_3{}^2\right] \\ 1 \end{bmatrix} \qquad \text{for } \lambda_3, \tag{C.10}$$

$$\vec{\xi}_5 = \begin{bmatrix} \xi_{51} \\ \xi_{52} \\ \xi_{53} \end{bmatrix} = \begin{bmatrix} \dfrac{b_{12}\left(b_{33} - \lambda_5^2\right) - b_{32}b_{13}}{b_{32}\left(b_{11} - \lambda_5^2\right)} \\ -\dfrac{1}{b_{32}}\left[b_{33} - \lambda_5{}^2\right] \\ 1 \end{bmatrix} \qquad \text{for } \lambda_5. \tag{C.11}$$

Further rearranging, the characteristic vectors take the form of:

$$\vec{\xi} = \begin{bmatrix} 1 & \dfrac{b_{12}(b_{33}-\lambda_3^2)-b_{13}b_{32}}{(\lambda_3^2-b_{11})} & \dfrac{b_{12}(b_{33}-\lambda_5^2)-b_{13}b_{32}}{(\lambda_5^2-b_{11})} \\ 0 & \left(b_{33}-\lambda_3^2\right) & \left(b_{33}-\lambda_5^2\right) \\ 0 & -b_{32} & -b_{32} \end{bmatrix}. \qquad \text{(C.12)}$$

However, for the solution of the whole system expressed in Eqs. (C.2), one has to find the other solution vectors, Z_2, Z_3, Z_6, Z_7 and Z_8, as well. Referring to the first of Eqs. (C.1), one will see that the solution, $Z_2(y)$ is found by taking directly derivative of $Z_1(y)$ with respect to y; that is:

$$Z_2(y) = c_1\xi_{11}\lambda_1 e^{\lambda_1 y} + c_3\xi_{31}\lambda_3 e^{\lambda_3 y} + c_5\xi_{51}\lambda_5 e^{\lambda_5 y}. \qquad \text{(C.13)}$$

Eqs. (C.1) also show that the solution, $Z_6(y)$ is the direct derivative of $Z_5(y)$ with respect to y:

$$Z_6(y) = c_1\xi_{13}\lambda_1 e^{\lambda_1 y} + c_3\xi_{33}\lambda_3 e^{\lambda_3 y} + c_5\xi_{53}\lambda_5 e^{\lambda_5 y}. \qquad \text{(C.14)}$$

For the solution, $Z_3(y)$ is determined by substituting the solution vectors, $Z_1(y)$, $Z_4(y)$, $Z_5(y)$ into DZ_3 expressed in Eqs. (C.1) and integrating it once. Then, it becomes:

$$Z_3(y) = c_1\left[-i\left(\frac{\xi_{11} + B_e\left(\gamma M^2\xi_{12} - \xi_{13}\right)}{\lambda_1}\right)\right]e^{\lambda_1 y} + c_3\left[-i\left(\frac{\xi_{31} + B_e\left(\gamma M^2\xi_{32} - \xi_{33}\right)}{\lambda_3}\right)\right]e^{\lambda_3 y}$$

$$+c_5\left[-i\left(\frac{\xi_{51} + B_e\left(\gamma M^2\xi_{52} - \xi_{53}\right)}{\lambda_5}\right)\right]e^{\lambda_5 y}. \qquad \text{(C.15)}$$

As clarified in Chapter 3, the last two, DZ_7 and DZ_8 of Eqs. (C.1) are decoupled from the first six equations so that they could be solved independently. The system formed by these two independent equations is then:

$$D^2 Z_7 = \left[iRB_e + A\right]Z_7. \qquad \text{(C.16)}$$

and the characteristic values forming the its solution are:

$$\lambda_{7,8} = \lambda_{1,2} = \pm\sqrt{b_{11}}. \qquad \text{(C.17)}$$

Here also, only the negative signed value is taken into consideration because of the reason mentioned previously for other obtained characteristic values. Hence, the solution of $Z_7(y)$ turns into:

$$Z_7(y) = c_7 e^{\lambda_7 y}. \qquad \text{(C.18)}$$

Consequently, remembering that $Z_8(y) = DZ_7$, the derivative of $Z_7(y)$ with respect to y gives the last solution vector:

$$Z_8(y) = c_7\lambda_7 e^{\lambda_7 y}. \qquad \text{(C.19)}$$

All these vectors form together the general solution of Eqs. (C.1). To see the expanded demonstrations of these solution vectors, one can refer to Chapter 3.

Needless to say, the formulation and the solution procedure take place for the general cases, i.e., 3D compressible boundary layers with oblique waves. For 2D boundary layer problems such as in the present study, one has to make an additional simplification as setting W_e to zero. For plane waves, β should also be set to zero as well.